



University  
of Glasgow

Bai, Xiaohong (1992) Microstructural deformation of clay. PhD thesis

<http://theses.gla.ac.uk/6940/>

Copyright and moral rights for this thesis are retained by the author

A copy can be downloaded for personal non-commercial research or study, without prior permission or charge

This thesis cannot be reproduced or quoted extensively from without first obtaining permission in writing from the Author

The content must not be changed in any way or sold commercially in any format or medium without the formal permission of the Author

When referring to this work, full bibliographic details including the author, title, awarding institution and date of the thesis must be given

**MICROSTRUCTURAL DEFORMATION OF CLAY**

by

**XIAOHONG BAI**

A thesis submitted for the degree of

Doctor of Philosophy

Department of Civil Engineering

University of Glasgow

November 1992

© XIAOHONG BAI, November 1992

*[Handwritten signature]*

*TO*  
*MY FATHER AND MOTHER*

## A B S T R A C T

This thesis reports observations of the changes to the microstructure of a saturated kaolin clay during normally consolidated undrained shear together with some complementary observations of normally consolidated and over-consolidated drained shear.

Three new methods of digital image analysis of optical microscopy have been developed to provide a novel method of analysing clay structures in failed and unfailed specimens. This method provides both a map of the microstructure and a histogram of the orientations, from both of which further analyses may be made. The results obtained agree well with measurements made using the older technique of micro-photometric analysis.

In addition, more than 800 electron micrographs from the main series of tests were analysed, this being one of the first uses of a new set of algorithms which had recently been developed to analyse microstructure with orientated textures. In addition, the density field was smoothed and itself analysed. All of these results were in general agreement with the measurements from the optical microscopy.

As far as is known, this is the first study to concentrate on the microstructural deformation of clay in undrained shear. The material was naturally dispersed; and it had been expected that during pre-peak deformation the platy clay particles would slip and turn to form large domains (*i.e.* groups of sub-parallel particles) inclined at  $45^{\circ}$  or more, although other hypotheses were also under consideration. Both optical microscopy and electron microscopy showed that the preferred orientation, which was originally horizontal, definitely remained horizontal whilst the shear strain increased, until the failure plane cut through this orientated structure.

It was expected that when strongly anisotropic clay samples are deformed, the shear strain will disrupt the structure, so that the strength of anisotropy decreases. Conversely, when isotropic clay samples are deformed, it was expected that slippage of the particles will cause the strength of anisotropy to increase. The present samples started at a moderate strength of anisotropy, and the subsequent changes were small. This observation supports the above hypothesis and

suggests that the samples were on the borderline between the two types of behaviour. There were, however, some changes of the microstructure. The strength of anisotropy at first appeared to increase and later to decrease as strain increased. The deviations of the orientations of the individual structural elements appeared to decrease at first and later to increase, this being the complementary trend. In addition, post-peak, the between-samples standard deviations increased with strain, suggesting that different samples were deforming in different ways.

The sizes of all the features mapped in both types of micrograph were measured. On average, these varied only slightly with strain. However, it appeared that in some samples the features identified in optical microscopy became larger as strain increased, whereas in others they may have become smaller. This again suggests that the effect of strain on samples which were originally similar was to make them become dissimilar.

These results suggest that in normally consolidated undrained shear there may be three mechanisms acting within these samples, *i.e.* they were bedding down at first, and later being disrupted by the shear strains; but the failure plane cut through all pre-existing structure non-conformably. Further, there may have been an element of instability in the microstructural response to strain. The results available for the other series of tests led to broadly similar conclusions.

## ACKNOWLEDGEMENTS

The author wishes to express her deeply grateful thanks to her research supervisor, Dr. Peter Smart, Lecturer in the Department of Civil Engineering at the University of Glasgow, for his constant guidance and encouragement throughout the research programme.

The author's special thanks are due to Dr. I. McConnachie, Lecturer in the Department of Civil Engineering for his useful discussion and help he made for the author during the research study, and to Prof. D. Muir. Wood, Head of the Department, for his allowing the use of the facilities in the Department.

The author's thanks are due to Mrs. X. Leng in the Department, who provided the image analysis program, to Mr. K. Shrapel of Queen Mary College, London, who made the thin sections, to Mr. A. Burnett in the Department, who prepared the specimens used for Scanning Electron Microscopy, to Mr. P. Ainsworth in the Department of Geology, who gave patient help to familiarize the author with the use of the Scanning Electron Microscope, and to Mr. D. Higgins, the manager of the Meiko computer, for his help in running it.

The author wishes to acknowledge Taiyuan University of Technology for giving her the opportunity to pursue higher degree abroad and the Education Commission of Shanxi Province for financial support, also US AFOSR 87.0346 for some further assistance.

The author also wishes to thank all those colleagues and friends, whose help and words of encouragement enable her to complete this study, with special mention of Mr. Hao Wang, Dr. Meijiu Wei and his wife Mrs. Xiaonian Xue.

Finally, the author gratefully acknowledges the help, sacrifice and support of her husband, Jungang Jia, her daughter, Fan Jia, and parents-in-law, Lingyun Jia and Fengling Zhang, without which this study could not have been concluded.

# C O N T E N T S

ABSTRACT

ACKNOWLEDGEMENTS

CHAPTER 1 INTRODUCTION AND REVIEW OF THE PRESENT  
KNOWLEDGE OF CLAY STRUCTURE

1.1	Introduction	1
1.2	Clay Particles	2
1.2.1	Physical Properties	2
1.2.2	Structure	4
1.2.3	Cation Exchange	5
1.2.4	Types of Clay Minerals	7
1.3	Clay Water System	10
1.3.1	Clay Water	10
1.3.2	Adsorbed Water	12
1.3.3	Double Layer Water	13
1.3.4	Inter-Particle Forces	15
1.4	Clay Structures	17
1.4.1	Factors Affecting the Structure	17
1.4.2	Open Structures	19
1.4.3	Dense Structures	21
1.5	Stress Effects	22
1.5.1	Consolidation	22
1.5.2	Deformation and Failure	25
1.5.3	Compaction	27
1.6	Scope	29
	Figures	30

## CHAPTER 2 MECHANICAL EXPERIMENTAL PROGRAMME

2.1	Introduction	37
2.2	Material	38
2.3	Filter Press	39
2.3.1	Slurry Preparation	39
2.3.2	Cake Preparation	40
2.4	Triaxial Test	42
2.5	Stress-Strain Characteristics	44
	Figures	46

## CHAPTER 3 PREPARATION OF SAMPLE

3.1	Introduction	50
3.2	Review of Present Methods of Sample Preparation	50
3.2.1	Drying	51
3.2.2	Impregnation	54
3.2.3	Grinding and Polishing	55
3.3	Sample Preparation	58
3.3.1	Introduction	58
3.3.2	Pore Fluid Substitution	59
3.3.3	Impregnation	60
3.3.4	Grinding and Polishing	60
3.4	Conclusion	62
	Figures	63

## CHAPTER 4 METHODS OF OPTICAL MICROSCOPY

4.1	Introduction	65
4.2	A Previous Method - Polarising Micro-Photometric Analysis (PMPA)	66
4.3	Polarising Micro-Photometric Mapping (POLMAP)	68
4.4	Advanced Polarising Micro-Photometric Mapping	

	(POLMAP4 and POLMAP3)	73
4.4.1	POLMAP4	73
4.4.2	POLMAP3	75
4.5	Discussion	76
	Figures	78
<b>CHAPTER 5 SCANNING ELECTRON MICROSCOPY</b>		
<b>AND IMAGE ANALYSIS</b>		
5.1	Introduction	87
5.2	Scanning Electron Microscopy	88
5.2.1	Scanning Electron Microscopy	88
5.2.2	Scanning Electron Microscope Operating Conditions	89
5.3	Image Analysis	93
5.3.1	Introduction	93
5.3.2	Intensity Gradient – PICDIF	95
5.3.3	Consistency Ratio Mapping – PICCON	97
5.3.4	Orientation Enhancement	100
5.3.5	Porosity Analysis – PICPOR	101
5.4	Flow Chart	103
	Figures	108
<b>CHAPTER 6 OBSERVATION AND DISCUSSION OF THIN SECTIONS</b>		
6.1	Introduction	114
6.2	Preliminary Observation on Failure Planes	115
6.2.1	Introduction	115
6.2.2	Normally Consolidated Undrained Shearing	115
6.2.3	Normally Consolidated Drained Shearing	116
6.2.4	Discussion	116
6.3	Normally Consolidated Undrained Triaxial Testing	116
6.3.1	General Observation	116

6.3.2	Pre- Consolidation and Triaxial Consolidation	117
6.3.3	Shearing	119
6.3.4	Standard Deviation	123
6.3.5	Discussions	124
6.4	Normally Consolidated Drained Triaxial Testing	125
6.5	Over- Consolidated Drained Triaxial Testing	127
6.6	Summary	129
	Figures	130

## CHAPTER 7 OBSERVATIONS OF SCANNING ELECTRON MICROSCOPY

7.1	Introduction	146
7.2	Comparisons of Methods	147
7.2.1	Comparison between Internal Methods	147
7.2.2	Comparisons between Optical Microscopy and Scanning Electron Microscopy	148
7.3	Effect of Shear Deformation	150
7.3.1	Introduction	150
7.3.2	Preferred Orientation	150
7.3.3	Anisotropy	150
7.3.4	Chord Size	151
7.4	Summary	152
	Figures	153

## CHAPTER 8 CONCLUSIONS AND RECOMMENDATIONS

8.1	Conclusions	162
8.1.1	Stress- Strain Behaviour	162
8.1.2	Sample Preparation	162
8.1.3	Optical Microscopy	163
8.1.4	Observation of Shear Deformation	164
8.1.5	Observation of Failure Planes	168

APPENDIX A	MECHANICAL TESTING PROCEDURE FOR NORMALLY AND OVER-CONSOLIDATED DRAINED SHEAR SERIES (UEA TESTS)	
A.1	Normally Consolidated Drained Series	170
A.1.1	Sample Preparation	170
A.1.2	Triaxial Test	170
A.2	Over-Consolidated Drained Shear Series	171
APPENDIX B	THE THEORY OF OPTICAL MICROSCOPY	
B.1	Without Plate	172
B.2	With a Quarter-Wave Plate	174
B.3	With a Half-Wave Plate	175
B.4	With a Whole-Wave Plate	176
B.5	Two Special Methods of Analysis	177
B.5.1	Method One: POLMAP4	177
B.5.2	Method Two: POLMAP3	178
	Figures	180
APPENDIX C	COMPARISON OF ANISOTROPY INDICES AND CONSISTENCY RATIO	
C.1	Introduction	181
C.2	Anisotropy Index A1	181
C.3	Anisotropy Index A2	184
C.4	Consistency Ratio CR	185
C.5	Conclusions	185
APPENDIX D	AN EXAMPLE OF OUTPUT FILE	187
REFERENCES		189

## Chapter One

### INTRODUCTION AND REVIEW OF THE PRESENT KNOWLEDGE OF CLAY STRUCTURE

#### 1.1 Introduction

It has been recognized from the early days of soil mechanics that the study of microstructure is of importance in the understanding of the engineering behaviour of soils (Terzaghi, 1925). The influence of soil microstructure on the response of soil to an applied stress has been the subject of investigation by a number of workers (Mitchell, 1956; Seed and Chan, 1961; Lambe, 1960; Smart, 1966b; De, 1970; McConnachie, 1971; Wong, 1975; Smart and Dickson, 1978; and others). Microstructure is to be distinguished from macrostructure which describes discontinuities, including fissure and crack patterns within the soil mass, which are visible to the naked eyes. Microstructure, which can not be discerned with the naked eyes, is a characteristic of assemblies of soil particles, which is referred to as structure and has two elements, geometrical arrangement and interparticle forces. Three types of interparticle forces have been suggested: firstly, quasi-reversible physico-chemical forces; secondly, irreversible frictional forces; and thirdly, quasi-irreversible cementation. With some exceptions, much of the work done previously has been qualitative. The establishment of the fabric changes during various types of deformation on a quantitative foundation would be more meaningful than a purely qualitative knowledge; if a quantitative function were available, further, it might be possible to develop a theoretical model for the processes at the primary particle level and to apply it to engineering practice.

This study is an enquiry into the practicability of describing a soil

quantitatively in terms of its constituent fabric elements; it employs new quantitative techniques of structural analysis to discern the mechanisms of deformation of shear and correlates the variation of the measured indices with the engineering behaviour of the soil.

Quantitative studies of the fabric changes accompanying shear have been undertaken using optical microscopy and electron microscopy. The former method is indirect, and recognizes the characteristics of aggregates of particles and of the small groups of particles. The latter methods can resolve individual particles and fabric elements and investigate the characters of particles and fabric elements.

In this research, three new methods of optical microscopy were developed and applied to three series of triaxial tests, and for the electron microscopy, Leng's image analysis techniques, which will be explained in Chapter 5, were employed to analyse the series for normally consolidated undrained shear, the other two series being analysed in the University of East Anglia.

## 1.2 Clay Particles

### 1.2.1 Physical Properties

In general, clay particles have the following characteristics: very small size; plate-like shape; large surface area per unit weight, which is the result of the above two characteristics; and physico-chemical interaction with both the water surrounding them and the ions within that water. All of these characteristics contribute to the complicated properties of the structures formed by the clay particles.

Clay particles consist of minerals which have a layered structure, and this is why the particles are usually plate-shaped although some are like needles. This combination of small size and platy habit results in a very large amount of surface area per unit weight, called the 'specific surface', for clay particles. The specific surface is a fully characteristic property for each chief group of clay minerals. (Based on this property, a method of clay mineral identification was developed by Konta in 1961).

The specific surface of a clay governs the bonding forces existing between its particles, and these forces depend on the character of the surfaces of the particles and on their environment. The inter-particle gravitational forces on the particles can be considered proportional to the volume. Both the volume and the coefficient of proportionality are small; thus, for the usual clay particles, the gravitational effects are less important than the surface bonding forces. These surface bonding forces between the clay particles result partly from their affinity for water. Clay will adsorb water from the atmosphere or from liquid water until each particle is enclosed in an envelope of water. In addition, there is an electrostatic interaction between the clay crystals and the ions within the water. These physical phenomena are the basis of a physico-chemical process which will be described in Section 1.3.1.

Therefore, the physico-chemical properties of clay particles are more important than the physical properties. Most of the physical properties of a clay mass, such as high void ratio, compressibility, etc., in fact, have a physico-chemical origin.

### 1.2.2 Structure

The basic structural units of most clay minerals consist of a silica tetrahedron and an alumina octahedron (Grim, 1953). Silicon and aluminium may be partially replaced by other elements in these units; this being known as isomorphous substitution. The basic units combine to form sheet structures which in turn combine forming particles.

The silica tetrahedron unit consists of a central silicon ion surrounded by four closely-packed and equally-spaced oxygen ions (Fig.1.1.a). The silica tetrahedral units are arranged to form an hexagonal network, which is repeated indefinitely to form a sheet (Fig.1.1.b). The tetrahedrons are arranged so that the tips of all of them point in the same direction, and the bases of all the tetrahedrons are in the same plane. The oxygen ion which forms the apex of each tetrahedron is not shared.

The alumina octahedral unit consists of a central aluminium ion surrounded by six closely-packed hydroxyl ions in two planar sheets (Fig.1.2.a). The alumina octahedral units are arranged repetitively to form a sheet in which all of the hydroxyl ions are shared (Fig.1.2.b).

The two basic structural units, alumina octahedron and silica tetrahedron, combine in two ways to form two common types of unit layer. One hydroxide sheet of the octahedron and one silicon tetrahedral sheet can form a common sheet, which is called a 1:1 type of structure, in which each apical oxygen at the silica tetrahedral sheet replaces one hydroxyl group of the hydroxide sheet of the octahedron (Fig.1.3.a). On the other hand, hydroxyl ions in the octahedral sheet replace oxygens from the apices of the silica tetrahedral sheet to form another

common sheet which is called as a 2:1 type of structure (Figs.1.3.b and c).

The intra-sheet bonds of clay particles can not be broken in engineering work (Lambe, 1953). However, the inter-sheet bonds may vary from strong to very weak, depending on the type of clay mineral. According to Lambe (1953) and Leonards (1962), in decreasing order of strength, components of such bonds may be:

- (1) hydrogen-bond;
- (2) bonds due to non-exchangeable cations;
- (3) secondary valence bonds (Van der Waal's forces);
- (4) bonds due to exchangeable cations;
- (5) bonding due to cementing agents.

### 1.2.3 Cation Exchange

A very important physico-chemical property of the clay minerals is their cation exchange capacity, *ie.* their ability to adsorb cations (Taylor, 1959), as will be explained in the following paragraphs.

The behaviour of a clay is greatly influenced by the nature of exchangeable cations held by it. The cation exchange capacity is defined as the sum total of exchangeable cations which it can adsorb. Since each cation is associated with a negative site, the permanent negative charge carried by a clay mineral can be regarded as equal to its cation exchange capacity (Taylor, 1959).

There are three causes of cation exchange capacity of the clay minerals (Grim, 1962):

1. Broken bonds around the edges of the silica-alumina units would give rise to unsatisfied charges which could be balanced by adsorbed cations. The number of broken bonds, hence the exchange capacity due to this cause, would increase as the particle size decreased. In kaolinite, broken bonds are the major cause of exchange capacity. In illite, broken bonds are an important cause of exchange capacity. In montmorillonite, broken bonds are responsible for a relatively small portion (20%) of the cation exchange capacity.

2. Substitutions within the lattice of trivalent aluminium for quadrivalent silicon in the tetrahedral sheet and of ions of lower valence, particularly magnesium, for trivalent aluminium in the octahedral sheet result in unbalanced charges in the structural units of some of the clay minerals. In montmorillonite, substitutions within the lattice cause about 80% of the total cation exchange capacity. But in illite, a small amount of the exchange capacity may result from lattice substitutions; and in kaolinite, very little isomorphous substitution is found.

3. The hydrogen of exposed hydroxyls may be replaced by a cation which would be exchangeable. Some hydroxyl groups would be exposed around the broken edges of all the clay minerals, and cation exchange due to broken bonds would, in part at least, be replacement of the hydrogens from exposed hydroxyls on the surfaces of the particles.

In the clay minerals in which cation exchange results from broken bonds, the exchangeable cations are held around the edges of the flakes and elongate units. However, in the clay minerals in which the exchange reaction is due to lattice substitutions, the cations are held mostly on the basal plane surfaces.

In masses of clay with relatively small amounts of adsorbed water, it is likely

that the adsorbed cations are held directly in contact with, or at least very close to the clay mineral surface. In clay water systems, the exchangeable cations may be at a greater distance from the clay mineral surfaces and separated from them by water molecules. In practice, all pore water in soils contains some dissolved cations and anions and should be referred to as a solution.

Because of variations in mineral structure, clay minerals do not have a fixed exchange capacity, but a range which is influenced by a number of factors of which the most important is pH. Negative edge charges develop in solutions with pH values greater than 7, due to the loss of protons from the tetrahedral layers. Increasing pH leads to increased negative charges, hence increased cation exchange capacity. But, when the pH falls to less than 7, positive charges form on the particle edges, due to proton adsorption on the octahedral layers, with a resultant decrease in the cation exchange capacity.

Under a given set of conditions, various cations are not equally replaceable and do not have the same replacing power. Therefore, the behaviour of the soil will be influenced not only by pH but also by the concentration of the ions present and by their type. However, there is not a single, universal replaceability series. The series varies depending on the conditions, and on the clay mineral.

#### 1.2.4 Types of Clay Minerals

As mentioned above, two units, silica tetrahedron and alumina octahedron, are involved in most of the clay minerals. These structural units link together to form 1:1- or 2:1-type sheets which are called unit layers. The various clay minerals are formed by stacking combinations of these basic sheet structures with different forms of bonding between the combined sheets. The principal clay

minerals formed are kaolinite, illite, and montmorillonite. A brief discussion of these will be given in the following. A detailed study of clay mineral structures was made by Grim (1953), and a comprehensive selection of electron micrographs of clay minerals was given by Beutelspacher and Van der Marel (1968).

### i. Kaolinite

Kaolinite consists of a 1:1-unit layer based on a single sheet of silica tetrahedrons combined with a single sheet of aluminium octahedrons (Fig.1.3.a). The basal spacing of these unit layers is about  $7.2 \text{ \AA}$ , and the planes between them are cleavage planes. Hundreds of such units are stacked together like leaves of a book to form one particle. Thus, the particles of kaolinite are larger than those of the other clay mineral types, and may be as much as  $10 \text{ }\mu\text{m}$  in diameter and  $2 \text{ }\mu\text{m}$  in thickness; but 10 times smaller is more typical. The basic morphology of kaolinite is of six-sided flakes, frequently with a prominent elongation in one direction; but many kaolinite particles are irregular flakes.

In kaolinite, secondary valence bonds and hydrogen bonds link adjacent layers. Due to this strong bonding, there is no possibility of entry of water between the successive sheets of the particle. This hydrogen bonding effect is also responsible for the tendency to form large particles.

There is very little isomorphous substitution in kaolinite. Consequently, its cation exchange capacity is quite low, being 3 to 15 meq. per 100 g, and its specific surface area is small, having a higher ratio of edge area to total surface area. Therefore, the effect of pH of the pore fluid on the net negative charge is more important for kaolinite than for other minerals (Van Olphen, 1963).

## ii. Illite

Illite has a 2:1-unit layer consisting of a sheet of alumina octahedrons sandwiched between and combined with two sheets of silica tetrahedrons (Fig.1.3.b). Particles are formed by the stacking of unit layers, which have a basal spacing of about  $10.3 \text{ \AA}$ . The size of the particles is intermediate between particles of kaolinite and montmorillonite, a typical diameter being  $0.3 \text{ }\mu\text{m}$  or less.

In the octahedral sheet, there is partial substitution of  $\text{Al}^{+++}$  by  $\text{Mg}^{++}$  and  $\text{Fe}^{++}$ ; and in the tetrahedral sheet, there is partial substitution of  $\text{Si}^{++++}$  by  $\text{Al}^{+++}$ . The combined sheets are linked by fairly weak bonding due to non-exchangeable potassium ions held between them. As a result, the distance between unit layers is fixed and small enough ( $0.76 \text{ \AA}$ ) to prevent water or other cations from entering between them. Therefore, the lattice is non-expanding in distinction to the montmorillonite discussed below.

About 20% of the silicon ions in the silica sheet are replaced by aluminium ions. This isomorphous substitution gives a residual negative charge to the illite structure units. However, most of this negative charges is balanced by the positive charges of the strongly held non-exchangeable potassium ions. Thus, the only exchangeable cations are found on the outside surfaces of the particles; and the cation exchange capacity is comparatively low, being 10 - 40 meq. per 100 g.

## iii. Montmorillonite

Montmorillonite has the same basic structure as illite. The unit layers are

about 9.5 Å thick. The montmorillonite particles are formed by the stacking of the unit layers. The size of particles is very small, about 1000 Å diameter. In the presence of a sufficient quantity of water, montmorillonite will break down into flexible flakes only one unit layer in thickness. In the octahedral sheet there is partial substitution of aluminium by magnesium. There is less isomorphous substitution than in illite (up to 15%), so bonding between unit layers in montmorillonite is weaker. In consequence, the space between the combined sheets is occupied by water molecules and exchangeable cations (Fig.1.3.c).

The isomorphous substitutions result in residual negative charges on the unit layers, a large percentage (about 80%) of which is satisfied by the attraction of exchangeable cations from the soil water to the surfaces of the individual unit layers. Thus, montmorillonite has a high value of cation exchange capacity, being 80 – 150 meq. per 100 g. Because the amount of water between the unit layers may vary depending on circumstance, montmorillonite possesses an 'expanding lattice structure'. The distance between the unit layers varies as the number of molecular water layers between these layers changes, depending on the abundance of the water and the nature of the exchangeable cations. This is the origin of the swelling behaviour exhibited by montmorillonite soils.

### 1.3 Clay Water System

#### 1.3.1 Clay Water

In the natural state, soil always contains some water. The smaller the size of the particles of soil, the more the effect of the water in the soil is. Especially for clay, water has a fundamental influence on its properties.

Each particle of clay develops a film of water all round it, the thickness of which depends on the mineralogy of the clay; the quantity of available water; and the conditions of the environment, *ie.* cation concentration, cation valence, pH, temperature, electrolyte concentration, dielectric constant, *etc.* This layer of water is held round the clay mineral particle partly by hydrogen bonding and partly by the effect of the electrostatic field set up by the negatively charged surface of the particle, because water molecules are dipolar. Superimposed on the effect of the water, there is an ionic effect. A 'double layer' is formed by the negative charge on the particles and the positively charged cations which are attracted to balance it. For a given particle the thickness of the double layer depends mainly on the valency and concentration of the cations: an increase in valency (due to cation exchange) or an increase in concentration will result in a decrease in layer thickness, and an increase in temperature will also result in a decrease in layer thickness. In addition, the thickness of the double layer will depend on the intergranular pressure, since particles are forced to approach more closely to each other by an increase of intergranular pressure, thus reducing the thickness of the double layer. Under some conditions, the adsorbed cations are free to move within the general neighbourhood of the surface of the particle, in which case there is a 'diffuse double layer'.

Two other phenomena are superimposed on the preceding. Firstly, the water molecules may be directly attracted to the cations, which are then said to be 'hydrated'. Secondly, some of the cations may be tightly held to cation points on the surfaces of the particles, this being called 'specific adsorption'. However, it is the first two phenomena which are usually treated as the important ones.

According to Lambe (1958), the clay water can be categorised as adsorbed

water (close to the surface), double layer water (corresponding to the diffuse double layer), and free water. The amounts of adsorbed and double layer water per unit weight of mineral increase with decreasing particle size. Most of the pore water in naturally occurring clay is within the double layer.

### 1.3.2 Adsorbed Water

Adsorbed water is the water which is held closest to the surface of the particles, and it is bonded mostly strongly to them. Lambe (1958) suggests that a pressure of 10000 atmospheres may be required to remove the innermost molecular layers.

The thickness of the adsorbed water layer is sometimes considered as being of  $8 \text{ \AA}$  to  $28 \text{ \AA}$ , representing a range of three to ten molecular layers of water. The available water covers all particles with a film of water one molecular layer thick before any particle adsorbs a second layer. The process is reversed as the water is removed. The thickness of the adsorbed water layer depends on two factors (Scott, 1969):

1. The concentration of ions in the soil water. Increasing the concentration increases the number of cations close to the surface, and therefore reduces the thickness of the adsorbed water layer needed to neutralise the negative ions in the particle.

2. The type of cation in the adsorbed layer. The rate of diffusion of the ions out of the adsorbed layer depends on their size, so that this will also affect the thickness of the layer.

The adsorbed water is different from the liquid water, *ie.* normal water. However, there is considerable uncertainty as to the nature of the differences between the adsorbed water and normal water, and the form which adsorbed water takes is not yet understood. For example, one view is that the adsorbed water is not able to transfer static water pressure and to move in the direction normal to the surface of the particles. It can shear more easily than the liquid water, but it is more resistant to the normal stress. The water is sometimes thought to be less dense, more viscous, and possess a less random configuration of molecules than liquid water (Low, 1959).

### 1.3.3 Double Layer Water

Strictly, the double layer water is all the water which experiences attraction towards the soil particles, but it is more convenient to follow Lambe's scheme and to exclude the adsorbed water, which is the innermost part of the double layer proper.

Because clay particles are very small, having equivalent spherical diameters of less than 1  $\mu\text{m}$ , and because very small particles are (usually) colloidal, most clay mineral particles can be considered as collidal particles. Colloidal theory deals with very dilute suspensions of colloids, which are very different from the clay masses which the soil engineer encounters. However, the theory developed for colloids is relevant to the understanding of the behaviour of clay masses.

A clay colloid dispersed in water will carry some negative electrical charge on its surface, as was discussed in Section 1.2.3. Since the net electrical charge of the entire clay water system obviously remains zero, the charge on each clay colloid must be neutralised by opposite charges of a sufficient number of cations,

often called 'counter ions' or 'exchangeable ions', drawn towards the particle as explained above. In addition to the force of electrical attraction due to the charged clay particle surface, these ions experience forces due to their inherent thermal motion and due to the attraction exerted on them by other ions and colloids. As a consequence, each ion occupies a position which represents a compromise between the various forces mentioned above to which it is subjected. There is of course some motion superimposed, and there may be some exchange of ions with the free water. Thus, each dispersed colloidal particle is surrounded by a swarm of ions in close proximity to its surface, so that the negative charge of the particle is balanced by the net positive charge of these ions. This swarm of ions is mostly composed of cations, but it may also contain a small number of anions, as shown in Fig.1.4.a, which shows a diffuse double layer for a particle suspended in water. If a proportion of the exchangeable cations are held closely against the surface of the clay particle, in effect the charge on the clay particle is reduced, and Fig.1.4.a may still be used to represent the diffuse part of the double layer. Another situation arises if all the exchangeable cations are held closely; but the following discussion will concentrate on the diffuse double layer. In the diffuse (part of the) double layer, the concentration of the counter ions near the particle surface is high, and it decreases with increasing distance from the surface. The exact distributions of the cations and anions, as a function of the distance from the clay colloid surface, can be obtained from the electrostatic and diffusion theory (Van Olphen, 1963). The electric potential at any point within the double layer can also be computed from the same theory. Fig.1.4.b and c show typical distributions of the ionic concentrations and electric potential.

The thickness of the double layer for natural clays was suggested by Meade (1964) to be in a range of 50 Å to 300 Å. However, the thickness of the double layer varies with certain factors. Lambe (1958) lists a number of these.

Electrolyte concentration, valence of ions, and temperature, all cause a reduction of the thickness of the double layer as they increase. Dielectric constant, size of hydrated ion, pH, and anion adsorption, all cause an increase in the thickness of the double layer as they increase.

In a natural soil, the size of many particles are outside the colloid range, so that direct interference among adjacent particles cannot be dismissed; and the particles might be touching; and clay masses are subjected to external forces; all of which are outside the range of the colloid theory. Thus, certain limitations on the direct application of the double layer theory to the clay masses must be noted. However, the double layer theory raises important points which cannot be neglected in the consideration of clay soils. In a limited number of cases the theory has been found to be quantitatively applicable to certain purified clays.

#### 1.3.4 Inter-Particle Forces

In general, three types of inter-particle forces exist in a clay soil, these being the double layer force, Van der Waals force, and ordinary friction.

The double layer force is a repulsion which is determined by the colloidal theory. As mentioned above, certain limitations must be born in mind when clay masses are being considered.

At a certain distance apart, the double layers of two clay particles begin to interfere: they repel each other, because the outer parts of the double layers associated with them have the same charge. If their interference is small, the electrical potential contribution from the double layer of one particle will be not significant at the surface of the second particle and *vice versa*. Conversely, if

the two particles are very close together, strong interference between them will take place. Expressions for the corresponding repulsion potential and forces have been developed as functions of the inter-particle distance and electrolyte concentration (Fig.1.5.a). The range of the repulsive force between particles depends on the thickness of the double layers, which in turn depends on the environment.

The Van der Waals forces are weak attractive forces acting between all molecules. The theory postulates that each atom attracts all other atoms, and is attracted by them. This force decreases with a high power of the interatomic distance (Fig.1.5.a). However, the attractive force between two particles which each contains large numbers of atoms is significant when the particles are of the order of  $10 \text{ \AA}$  to  $20 \text{ \AA}$  apart. The Van der Waals attractive forces do not vary significantly when the electrolyte concentration of the solution changes.

Fig.1.5.b shows the combined effect of double layer repulsion and Van der Waals attraction between colloidal particles, following Meade (1964). At the high electrolyte concentration, the inter-particle forces are always attractive. In this case, the clay flakes will pack together in parallel. However, at low or intermediate electrolyte concentrations, the forces between particles are repulsive when the particles are far apart, and the forces between the particles are attractive when they are very close; thus, there is an equilibrium distance between particles, at which, the force between the particles is zero.

Olson and Mitronovas (1960) studied  $\text{Ca}^{++}$  and  $\text{Mg}^{++}$  illites consolidated in  $\text{CaCl}_2$ - and  $\text{MgCl}_2$ -solutions between  $0.0002 \text{ M}$  and  $1 \text{ M}$ , approximately, using soil-mechanics style consolidometers. They found that  $\text{Ca}^{++}$  and  $\text{Mg}^{++}$  illites are slightly more resistant to consolidation at intermediate salt concentration,

0.01 N to 0.1 N; but the effect of the concentration is small, and the observed curves are only in partial agreement with the curves calculated using Gouy–Chapman theory.

Lambe (1958) outlines the importance of these colloidal effects in soil mechanics. However, the general application of the double layer theory to clay water systems is apparently limited.

## 1.4 Clay Structures

### 1.4.1 Factors Affecting the Structure

The structure of clay soil is mainly studied using the techniques of electron and optical microscopy. The first results of electron microstructure of soil appeared in 1960 (Bates and Comer, 1954; Rosenqvist, 1960). Much progress has been made since then (Collins and McGown, 1974; Smart and Tovey, 1982; Bennett, *et al* 1990). The early study of clay structure was based on a consideration of the nature of clay particles, inter-particle forces and environment by indirect experiment. These early studies included some optical microscopy, which, although it cannot resolve individual particles, does reveal some aspects of the structure. As the technique of electron microscopy developed, the structural models were improved by the use of them, because the individual particles could be seen. Computer aided analysis of electron microscopy of soil dates back to Unitt's (1975) introduction of the intensity gradient method; but the work presented here together with parallel work in the University of East Anglia represents the first major use of computer aided image analysis of clay soils.

Before the structure of clay is reviewed, the factors affecting the structure, excluding the stress, are first considered. Meade (1964) presented a review about the effect of physical and chemical factors on the structure of clay. Lambe (1958) discussed briefly the influence of most of the factors. All of his explanations are based on the effect of the double layers of the clay particles.

Chemical factors include electrolyte concentration, cations and anions present, acidity, and dielectric constant. Rosenqvist (1955) and Hsi and Clifton (1960) studied the effects of the first two variables and showed that an increase of electrolyte concentration causes an increase of sediment volume, which indicates an increase of degree of flocculation. Later, Meade (1964) stated that the relation is valid for kaolinite and illite, but not for montmorillonite. Hsi and Clifton (1960) measured the settling volumes of clays in solutions of chlorides of  $\text{Na}^+$ ,  $\text{Ca}^{++}$ ,  $\text{Fe}^{++}$ ,  $\text{Al}^{+++}$ , and  $\text{Sn}^{++}$  to evaluate the effect of cations. They found that an increase of cation valence results in an increase of sediment volume, (except for iron).

The effect of pH was observed by Schofield and Samson (1954). They reported that increasing the pH value of the solution produces a decrease of sediment volume, and they concluded that flocculation is due to edge to face attraction of particles, which is strongest under acid conditions and diminishes with increasing pH. Lambe (1958) suggested that a decrease in the value of the dielectric constant produces an increase in sediment volume, *i.e.* an increase of degree of flocculation.

The 'physical' factors include temperature, drying, organic matter content and concentration of clay in the depositing medium, which may be important in the determination of particle arrangements in sediment. Some work on these factors

has been done by Lambe (1958), Emerson (1959), Ingram (1953) and Meade (1964). Increasing temperature causes a decrease in the double layer thickness, with a resultant tendency towards flocculation (Lambe, 1958). Drying of clays tends to irreversible domain formation (Emerson, 1959). The preferred orientation of clay particles in clayey rocks might relate to the presence of organic matter (Ingram, 1953). Meade (1964) found that the concentration of clay suspension influences the preferred orientation.

#### 1.4.2 Open Structures

As mentioned in Section 1.2.1, clay particles are essentially plate-like in shape. Their contacts may be edge to edge, edge to face or face to face. From an alternative point of view, the soil structure can be divided into two large classes: open structure and dense structure. Dense structures will be discussed in Section 1.4.3; open structures are discussed below.

An open structure model was proposed by Terzaghi (1925). He suggested that, during deposition, a small particle remains in its position of first contact as it arrives at a sediment surface, because the strength of the bond so produced is greater than the weight of the particle. In this way, an open, spongy network is built up. The most important open structures are cardhouse, bookhouse, and honeycomb structures, in all of which the particles arrange generally edge to edge or edge to face, so the void ratio is high.

In single-plate cardhouse structure, the plates are arranged singly with angular or perpendicular edge to face contacts presumably governed by some definite phenomena (Fig.1.6.a). These structures are subdivided principally into flocculated, cemented, and authigenic versions.

In bookhouse structure, small packets are arranged with angular or perpendicular edge to face contacts (Fig.1.6.b).

In honeycomb structure, the particles are grouped in sheets or chains, which are themselves grouped into a loose inter-connecting framework with relatively large voids between the sheets (Fig.1.6.c).

At one time, hypotheses involving single-plate cardhouse structure were common; but this type of structure appears to be rare (Collins and McGown, 1974; Smart, 1975). One of the most 'convincing' micrographs is of chlorite formed in situ (Hayes, 1970). Pusch (1970) observed the behaviour of clay particles in a drop of water whilst the water was evaporated inside a high-voltage electron microscope; and O'Brien (1972) conducted a series of experiments on fresh sediments prepared in the laboratory. Smart (1975) shows single-plate cardhouse structure that was tentatively attributed to microbiological activity. Smart went on to suggest that crumbs are formed as follows: (1) relatively large pores are formed by cultivation *etc.*; (2) Bacteria rearrange the particles near the surfaces of these pores one by one to form open structures stabilised by soft organic matter; (3) this organic matter condenses, drawing the particles together and forming stronger bonds.

Bookhouse structure has been frequently seen (Rosenqvist, 1959; Smart, 1966b and 1966c). Flocculent structure is fairly common. In some cases, random clusters of particles have been mixed among the chains or the clusters have occurred alone.

Closely packed random structures have been observed. These are denser than cardhouse and bookhouse structures. If cardhouse structures resulted from

stable edge to face contacts, the angles of contact would be distributed about a certain value, and the structures would be systematic, not random. Close packed random structure, cardhouse structure, probably bookhouse structure will extinguish between crossed polars.

Generally, the open structures occur either in an uncemented form, in which case they are unconsolidated muds, and the structure would change on reclamation, or the structures are cemented, in which case one obtains a quick clay (Smart, 1975).

#### 1.4.3 Dense Structures

Almost all dense structures are domain structures. Here the term domain means a group of plates orientated in approximately the same direction, and acting as a unit (Fig.1.7.a).

The domains occur under both natural conditions and in laboratory studies. They may be subdivided into overlap domains, in which the plates are separate particles (Fig.1.7.b), and intergrown domains, in which the crystal lattices are continuous from plate to plate, perhaps imperfectly (Fig.1.7.c). Overlap domains have been seen in failure planes. Presumably, intergrown domains may require more conditions to be formed than overlap domains.

Domain structures may also be divided into turbostratic structure and discrete domain structure. The former consists of large domains, some of which are curved; and it has few large voids and diffuse inter-domain boundaries. The latter consists of smaller domains, has well-defined structural boundaries and definite inter-domain voids.

Domains can be seen where thin sections of clay are examined between the crossed polars in an optical microscope. A domain is a group of platy particles orientated in the same direction. If the plates lie in the plane of the thin section, they are dark between crossed polars. Otherwise, they are bright if the direction of preferred orientation lies between the polars and dark if the direction of preferred orientation is parallel to the direction of either of the polars. Fuller details will be given when the new algorithms are introduced in Chapter 4.

Much of the evidence for domain structure has come from the application of electron microscopy (Smart, 1969). Bowles (1968) showed domains in a natural soil, and considered that they were not original features of the sediment fabric, but the results of in situ shear stressing. Pusch (1970) reported the formation of domains in zones adjacent to the failure plane of a sheared sample. Smart (1966b, 1966c) and McConnachie (1971) confirmed that consolidation may also result in a domain structure.

## 1.5 Stress Effects

It is well known that pressure greatly affects the microstructure of soil. Based on the engineering purpose, there are three effects to be discussed, these being consolidation, deformation and failure, and compaction.

### 1.5.1 Consolidation

In geotechnical engineering, the term consolidation means decrease in volume of saturated soil as water is expelled by pressure. In laboratories, the sample is often confined laterally, and the pressure is doubled daily. There are three models to describe the behaviour:

1. Mechanical: the particles slip, bend, or break, either coming into contact directly or being separated by very thin layers of adsorbed water.
2. Physico-chemical: double layer effects dominate as described above.
3. Mineralogical: strain is accommodated by migratory recrystallization.

Buessem and Nagy (1953) suggest that the characteristic feature of deformation is the sliding of one particle along another for the unconfined compression, which led them to expect an increase in the degree of preferred orientation. If so, this and also the following hypotheses would be general phenomena applying to all of consolidation, deformation and compaction. In 1959, Tan reported that bending of clay particles is possible and that under heavy local stresses montmorillonite particles may be broken. In the same year, using X-ray diffraction and sound propagation, Kaarsberg reported that increasing compaction of illite produced greater particle parallelism. These terms particle parallelism and preferred orientation appear to be used as synonyms; but for a complete understanding, it will be necessary to distinguish between local preferred orientation and overall preferred orientation, although not all of the authors mentioned below have made this distinction clearly.

Olson and Mitronovas (1960) and Olson (1962) studied consolidated illite at pressure of 47 kPa (7 lb/in<sup>2</sup>) by X-ray diffraction. They found increasing parallelism with increasing pressure, caused by slippage of particles at points of contact, and again suggested that bending of particles is possible.

Smart (1966c) examined consolidated kaolin at 370 kPa (4 kg/cm<sup>2</sup>), and found that the particles were grouped in domains with preferred horizontal

orientation.

The results of McConnachie (1971) showed a relationship between the intradomain void ratio and pressure for kaolinite up to 95,000 kPa (1000 kg/cm<sup>2</sup>) (see Smart, 1975). This suggests that at high pressure, the domains were themselves compressed as the mechanical inter-particle forces caused by the high pressure overwhelmed the physico-chemical interparticle forces.

Van Olphen (1963) found that the last layer of adsorbed water was removed from vermiculite (at 25°C) at a pressure of about 5200 atmospheres. Chilingar and Knight (1960), compressing samples between 266 and 1,330,000 kPa (*i.e.* 2.8 and 14000 kg/cm<sup>2</sup>), concluded that in this pressure range, only adsorbed water is removed.

During consolidation, the expulsion of water is usually accompanied by temporary increase of water pressure; however, in some soils, the volume continues to decrease after the excess pore pressure has disappeared. This continued consolidation is called secondary consolidation. There are three explanations to be offered (Smart, 1975):

1. When the particles slip into fresh positions, they are at first held apart by their adsorbed water layers, which are slowly squashed out.
2. Secondary consolidation is caused by pressure recrystallisation of the particles themselves.
3. The structure consists of groups of particles with large voids between. During primary consolidation the groups slip, setting up pore water pressure, but

during secondary consolidation, there is only yielding within the groups, any intragroup pore water pressure rises being inaccessible to measuring instruments.

### 1.5.2 Deformation and Failure

According to Lambe's study (1960), the electrical forces acting between clay particles should be completely different when they are parallel to each other and when they are in random orientation. On this basis, the shear strength will vary with the relative positions of the clay particles. This immediately leads to a need to study the microstructure of clays and the changes in the microstructure which occur when soil is deformed by the application of shear stresses. In addition, clays are often anisotropic; for example, some early studies (Ward, Marsland and Samuels, 1965; Aas, 1967) found that the strength along horizontal planes was greater than that along vertical planes. There are at least four phenomena which may cause anisotropy, these being: fissures of various types; layering of various types; anisotropy of inter-particle contacts; and preferred orientation of platy particles. The present study is concerned with the last of these.

Deformation means a change of shape less drastic than failure. It is known that during deformation, dense sands dilate and loose sands contract. The same phenomena may happen in clay; it might dilate or contract according to circumstances. In most situations, shear tests are done to apply one stress to deform the soil whilst using other stresses to confine it. When the confining stresses are too low to break the initial structure of the soil, saturated clays dilate when deformed under drained conditions, whereas they contract under much higher confining stresses. In unsaturated soils, the moisture tension will tend to act as a confining stress, and water scarcity may result in the adsorbed layers

becoming more ordered and thus increase the rigidity and tendency to dilate; but shrinkage cracks would weaken the soil. Presumably, dispersing conditions, whether due to changes in pH or ionic composition or to dispersing agents, will tend to permit clay particles to slip individually, thereby facilitating contraction; whereas flocculating conditions and cementation would tend to cause the particles to move in groups and cause dilation. There may also be an intermediate state in which the groups retain their identity but fail to bond to each other, so that the soil behaves as if dispersed.

Smart (1966b) showed that domains in a dispersed kaolin increased in size during shearing. Smart and Dickson (1978) studied a flocculated kaolin, and reported that both the length and breadth of domains increased by 50% during pre-peak deformation and decreased with further shear. They suggested that some of the domains may have been pressed together under stress.

Smart (1966c), Morgenstern and Tchalenko (1967), Barden (1972), De (1970), *etc.* also studied failure planes. They found that a complete preferred orientation of clay particles occurs within slickensided failure zones. These failure zones occur either singly, or with complementary zones at approximately  $45^\circ \pm \phi/2$ , or possibly as omisepic fabric. At-peak deformation involves breakdown of domains in the failure plane (Smart, 1966c; Smart and Dickson, 1978); in the zone of failure, the particles rearrange with complete preferred orientation. Within the failure planes, the particles seem to have been separated from each other, and some may have broken or recrystallised (Smart and Tovey, 1981).

To date, several hypotheses about the development of fabric in soils during shearing have been suggested for pre-peak deformation. They may be briefly summarized as follows (Smart and Tovey, 1989):

1. Domains grow in size and turn into a preferred direction parallel to the failure plane.
2. Domains act as rigid bodies and slip into closer packing without significant change in size or internal structure.
3. Domains retain their identity, orientation and relative positions, whilst strain is accommodated by small changes in their size, resulting from small internal changes in particle packing as the latter slip over one another.
4. Domains break into smaller domains; and then some of the fragments rotate into new orientations.

The aim of the present work is to see which if any of the above hypotheses apply (to a particular type of sample); but it is possible that more than one of these mechanisms may occur simultaneously during deformation. In addition, whilst text books usually quote the slope of a failure plane as  $\pi/4 + \phi/2$  to the direction of the minor principal stress, Vermeer (1990) showed that for granular soils, the direction can lie between  $\pi/4 + \phi/2$  and  $\pi/4$ . This suggests that in some circumstances the response of the soil structure to stress may be unstable.

### 1.5.3 Compaction

Here, the term compaction means compaction of unsaturated soils by various combinations of compressive and shearing stresses applied for brief periods, e.g. by wheels or in laboratory tests, and resulting in increased dry density, and usually increased strength and decreased permeability to water, air, and root penetration.

According to Soil Mechanics for Undergraduates (1985), the principal mechanisms controlling compaction of clay soils are as follows.

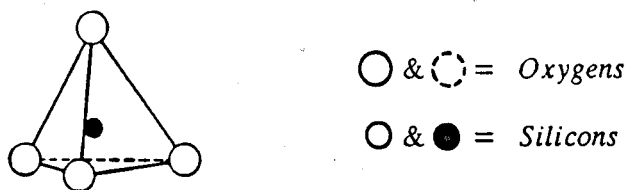
At a low water content, called stage A, there is not enough water for the full development of the double layers of the clay particles. The deficiency of water brings about high electrolyte concentrations, thus compressing the double layers, in turn, decreasing the electrical repulsion between the particles; so it favours flocculation of the particles, a low degree of preferred orientation of the particles, and low dry density as the result of random packing. As the moulding water content increases from low to intermediate, called stage B, the double layers get a chance of expanding, although at this stage also the water content is not enough for their full expansion. This increase of water content reduces the electrolyte concentration, resulting in increased repulsion between the particles, permitting a more orderly arrangement of particles, thus, bringing about an increase in the density at this stage. Further increase of water content, stage C, allows the electrolyte concentration to reduce further and the double layers to expand further. Thus, the electrical interparticle repulsion forces increase, but the attraction force are reduced due to the greater interparticle space at stage C. Therefore, the particles are arranged in a dispersed structure, a more orderly fashion at stage C than stage B. However, the dry density at this stage is lower than that at stage B, because the added water increases the interparticle spacings.

In general, it can be concluded that compaction of clays dry of optimum tends to produce a flocculated structure, and compaction wet of optimum tends to produce a dispersed structure. However, the flocculation and dispersion in the stages dry of optimum to wet of optimum may be very distinct for some soil types, whilst for others, it may be inappreciable.

## 1.6 Scope

Clay particles are extremely small and planar, and so possess large surface areas per unit weight. Consequently, the electrical charges associated with the particle surfaces, especially in the presence of water, significantly influence their behaviour. Van der Waals attraction, double layer repulsion, and possibly edge-face electrostatic attraction between particles determine the configuration of the clay structure, which is also sensitive to the environment. Hypotheses concerning shear deformation have been advanced for shear tests under different conditions of consolidation and drainage. However, insufficient observational evidence had been obtained concerning the phenomena which had been suggested. Therefore, this study represents an attempt to describe clay fabric, examined in an optical microscope and electron microscope, by using new image analysis technology and improved optical methods, and to apply these quantitative procedures to the measurement of soil structural changes over a whole series of normally consolidated undrained shearing deformation.

(a)



(b)

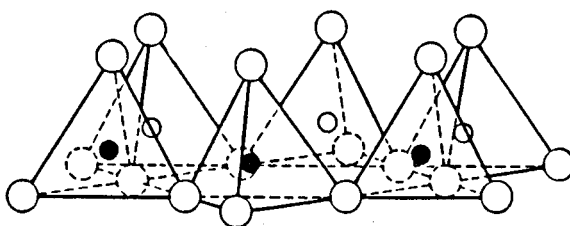
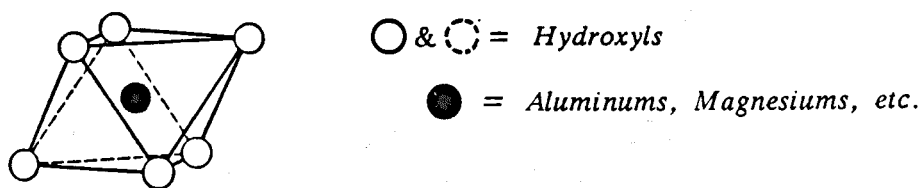


*Fig.1.1* Diagrammatic Sketch Showing (a) Single Silica Tetrahedron and (b) Sheet Structure of Silica Tetrahedrons Arranged in a Hexagonal Network (reproduced from Grim, 1953).

(a)



(b)

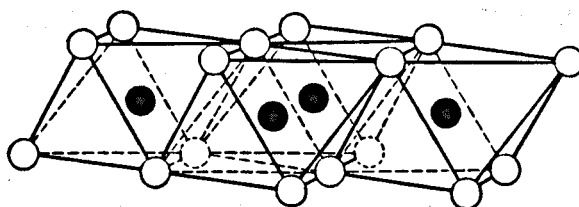


*Fig.1.2* Diagrammatic Sketch Showing (a) Single Octahedral Unit and (b) the Sheet Structure of the Octahedral Units (reproduced from Grim, 1953).

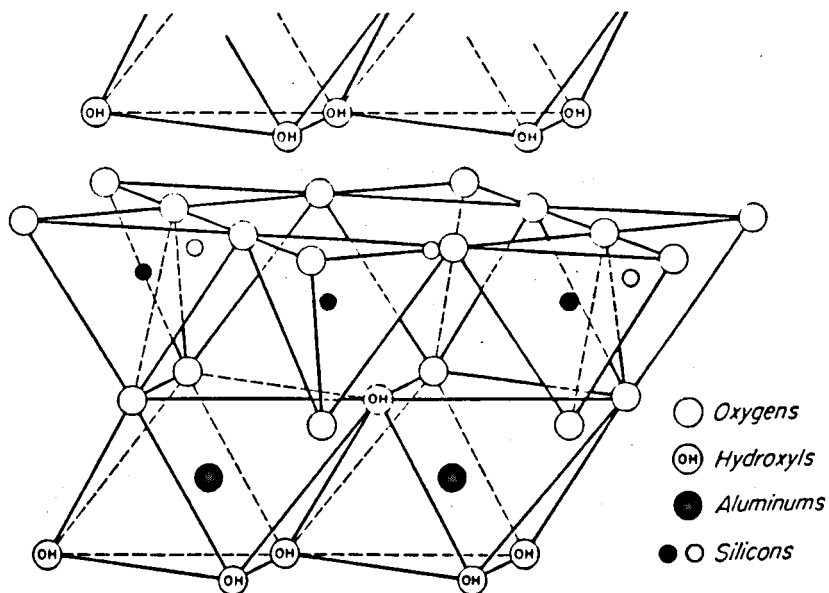


*Fig.1.3.a* Diagrammatic Sketch of the Structure of Kaolinite Layer  
 (reproduced from Grim, 1953).

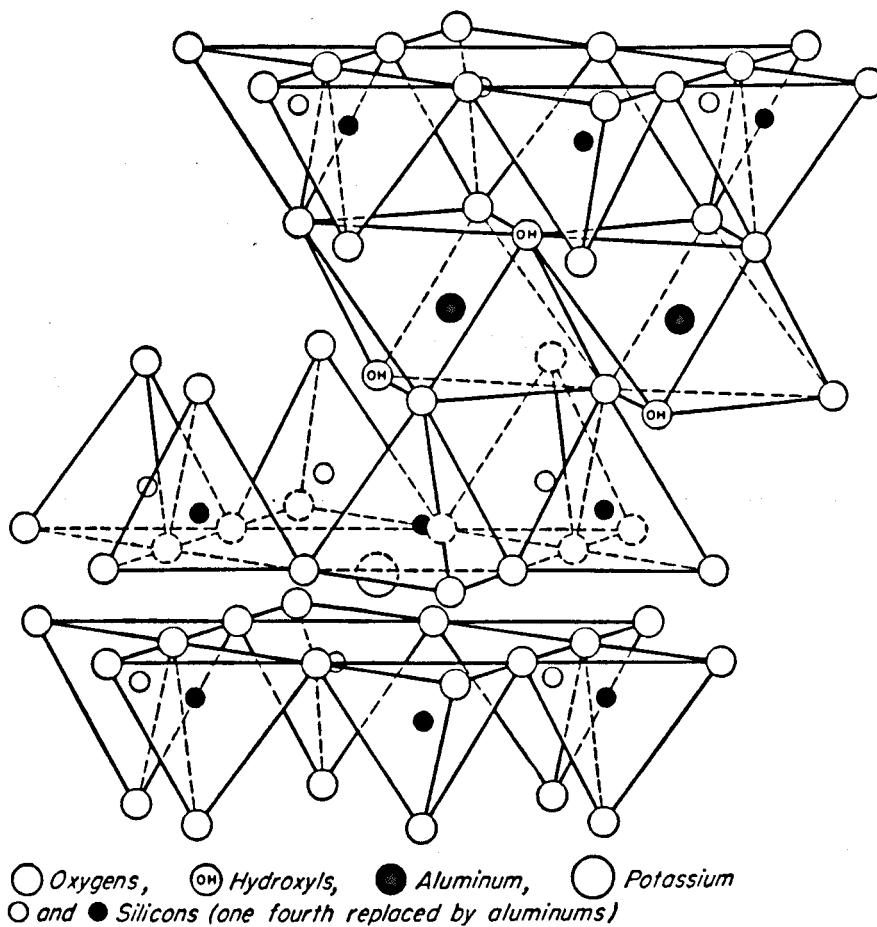


*Fig.1.3.b* Diagrammatic Sketch of the Structure of Illite  
 (reproduced from Grim, 1953).

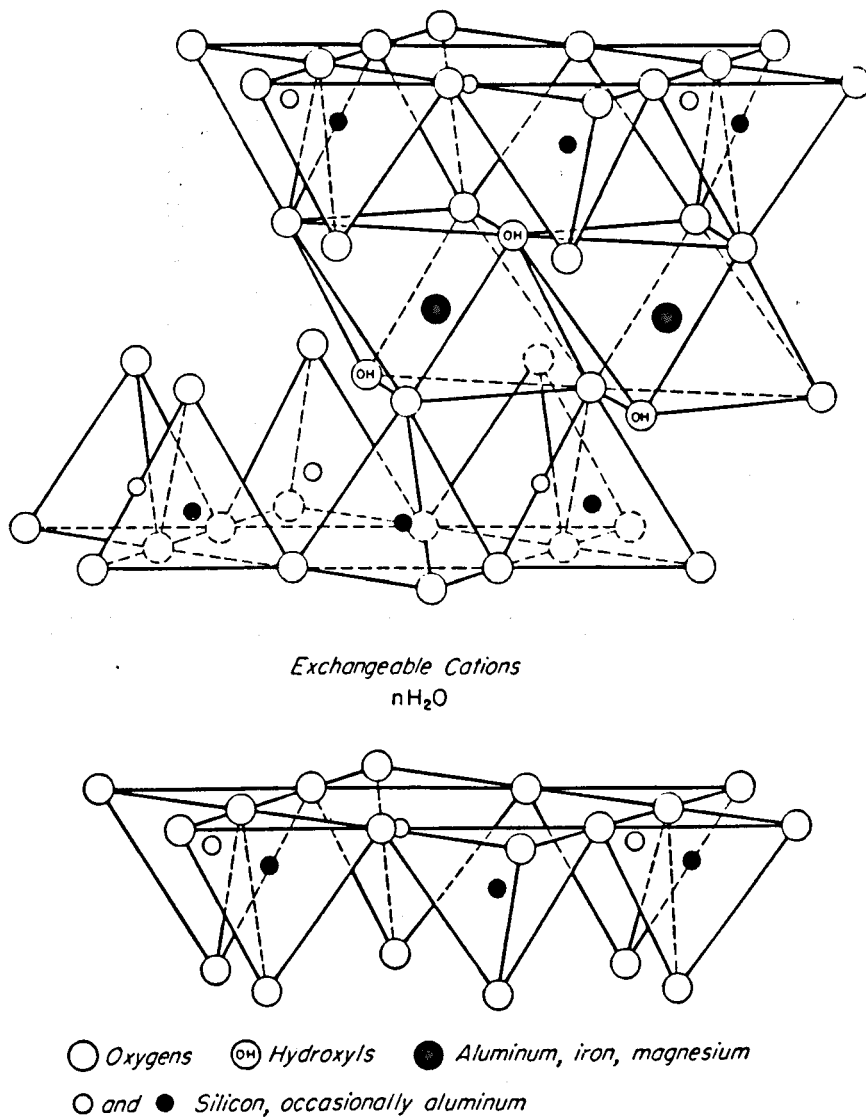


Fig.1.3.c Diagrammatic Sketch of Structure of Montmorillonite  
(reproduced from Grim,1953).

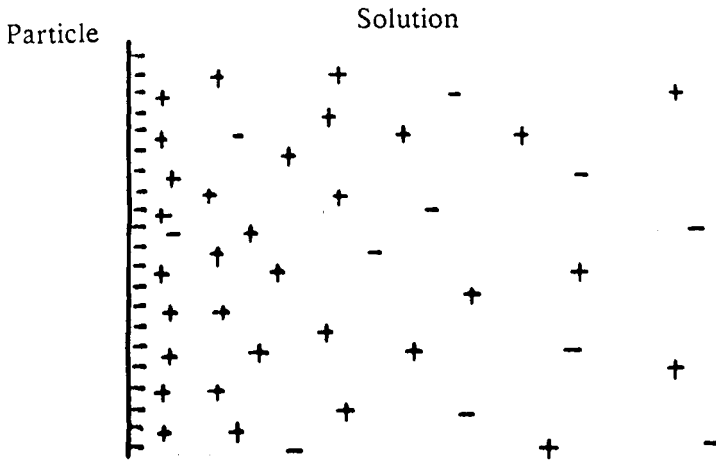


Fig.1.4.a Configuration of the Diffuse Electric Double Layer.

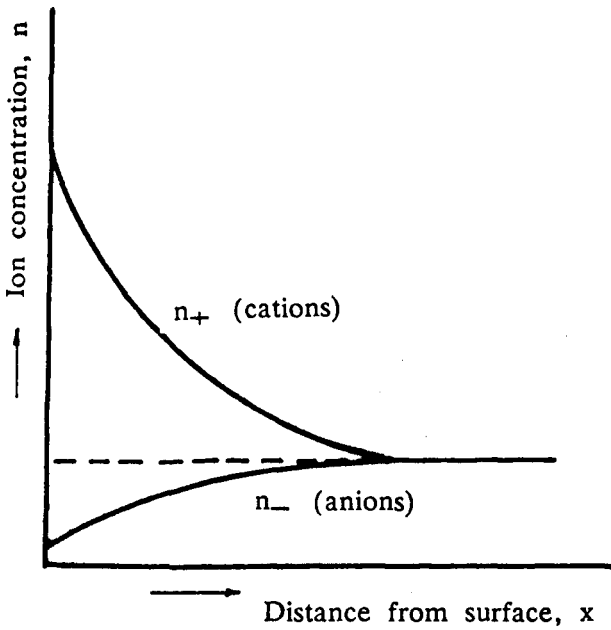


Fig.1.4.b Charge distribution in the Diffuse Electric Double Layer.

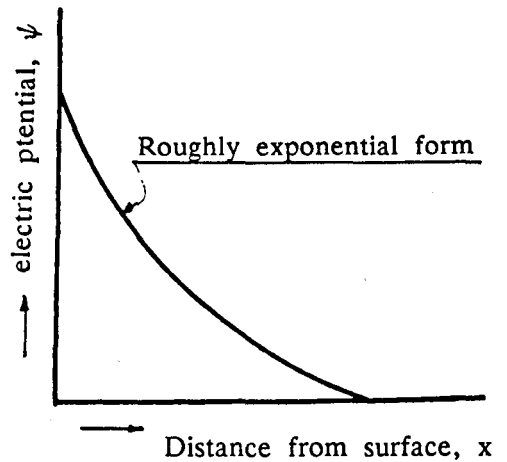


Fig.1.4.c Electric Potential Distribution in the Diffuse Electric Double Layer.

(reproduced fro Van Olphen, 1963).

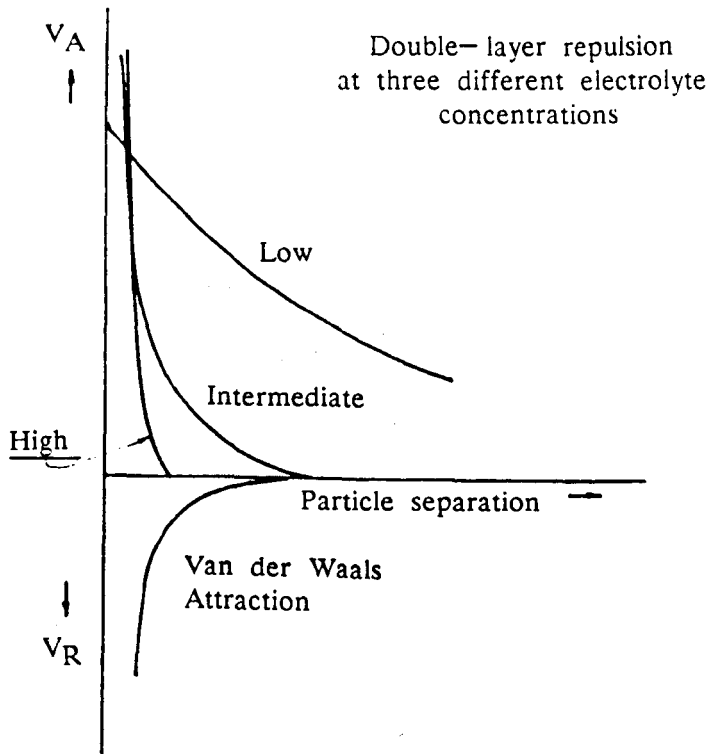


Fig.1.5.a Repulsion and Attraction as Functions of Particle Separation (reproduced from Van Olphen, 1963).

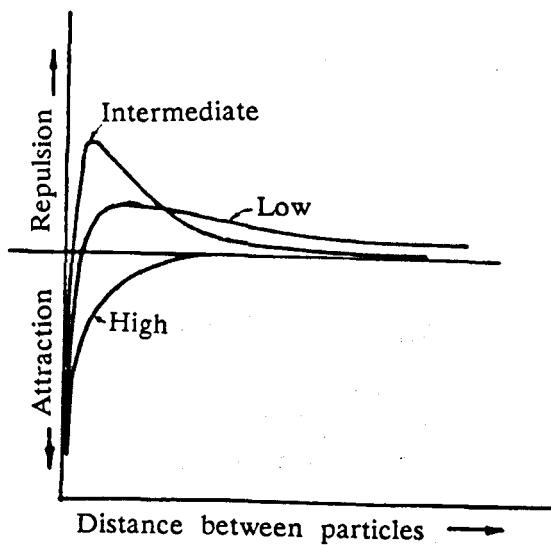
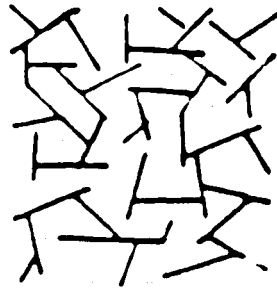
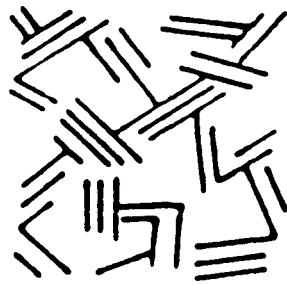


Fig.1.5.b Resultant of Repulsion and Attraction between Particles at three Different Electrolyte Concentrations. (reproduced from Meade, 1964).



(a) Single Plate Cardhouse Structure.



(b) Bookhouse Structure.



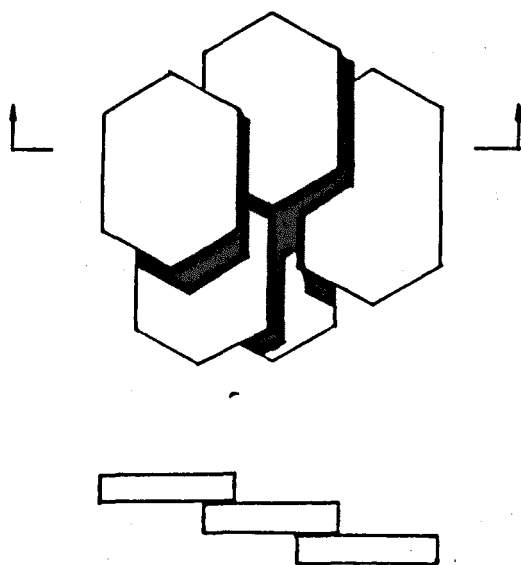
(c) Honeycomb Structure.

*Fig.1.6* Types of Open Structures

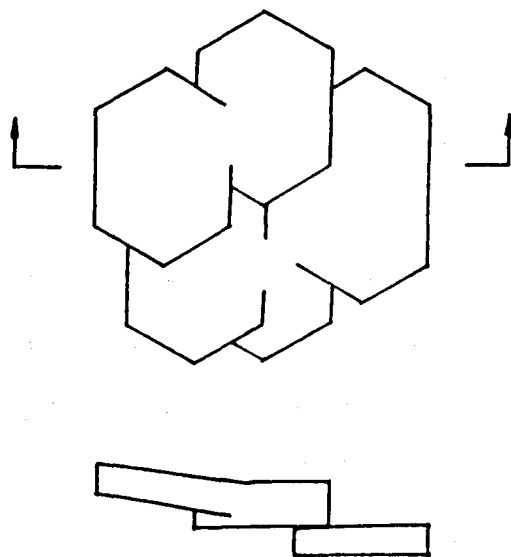
(reproduced from Smart, 1969)



(a) Domain



(b) Overlap Domain



(c) Intergrowth Domain

Fig.1.7 Domains (reproduced from Smart, 1992).

## Chapter Two

### MECHANICAL EXPERIMENTAL PROGRAMME

#### 2.1 Introduction

In modern soil mechanics, there are three standard types of triaxial test to be used in the soil laboratory; these are consolidated drained shear, consolidated undrained shear, and unconsolidated undrained shear. They reflect the behaviour of soil in most situations which arise in practice. The great advantage of triaxial tests is that, within limits, failure of the sample can be along the weakest plane in the sample; whereas the failure plane is fixed a priori in the direct shear box test. In the true triaxial apparatus, the pressures applied in the three main directions can be different, but few such apparatus are available. Therefore, the standard triaxial test was used in this study.

The behaviour of soil microstructure has been of wide interest for the last few decades; and studies of the properties of soils during shearing and consolidation have been made. However, observations for shearing have been taken only for a few cases (see Chapter 1) and using less advanced methods than were available here. Just before this research started, a joint study between the Universities of Glasgow and East Anglia had begun to study two cases of triaxial shear: normally-consolidated drained, and over-consolidated drained. Therefore, the normally-consolidated undrained case was chosen to be studied here. The full flow chart of the experimental programme is shown in Fig. 2.1, which includes the mechanical experimental programme, sample preparation, and analysis of micrographs. This chapter gives the details of the mechanical experimental programme, and the other parts will be discussed in the following chapters. The

results of the mechanical experiments compared with those of normally consolidated drained triaxial shearing tests from the University of East Anglia are also summarised in this chapter. The details of the University of East Anglia's mechanical experimental programme is given in brief in Appendix A.

## 2.2 Material

The type of clay used in the present study was selected to satisfy certain requirements, to be convenient and to be cheap.

A simple artificial clay was preferable for several reasons. The first reason is that it facilitates control of the conditions of the experiment and eliminates natural variability. At the same time, isolating a single clay mineral for study reduces the number of unknown factors and avoids the problem of interaction between different mineral types. Studying the behaviour of one type of clay at a time will allow comparisons between different types to be made. Another reason is that a low quartz content was desirable to avoid problems during the cutting of ultra-thin sections for viewing in the optical microscopy and electron microscopy.

Speswhite Kaolin satisfied the above requirements and was already in use in the University of East Anglia for the drained normally-consolidated shearing. Therefore, this clay was chosen so that comparisons between the drained and undrained tests may be made.

Table 2.1 contains details of the chemical, physical, and engineering properties of Speswhite Kaolin. Chemical analysis and pH and particle size values were obtained from the suppliers, English Clays Lovering Pochin and Co. Ltd.

Table 2.1 Chemical, Physical and Engineering Properties

CHEMICAL ANALYSIS % by weight	SiO <sub>2</sub>	46.2
	Al <sub>2</sub> O <sub>3</sub>	38.7
	Fe <sub>2</sub> O <sub>3</sub>	0.56
	TiO <sub>2</sub>	0.09
	CaO	0.20
	MgO	0.20
	K <sub>2</sub> O	1.01
	Na <sub>2</sub> O	0.07
	Loss on ignition	13.14
PHYSICAL PROPERTIES	% by weight finer than 2 microns	77-83
	% by weight finer than 10 microns	99.5
	Refractive Index	1.56
	Specific Gravity	2.62
pH		5.0
ATTERBERG LIMITS	Liquid Limit	67.5
	Plastic Limit	37.0
	Plasticity Index	32.5

### 2.3 Filter Press

#### 2.3.1 Slurry Preparation

According to Martin and Ladd (1975), kaolin should be mixed at the highest possible moisture content, because the orientation of particles in samples mixed at moisture contents less than about 1.5 times the liquid limit are more sensitive to small pressure changes than when using slurry with higher moisture contents. Preliminary trials at 100%, 110%, 120%, 140%, 160% and 200% moisture

contents for Speswhite Kaolin showed that samples mixed at moisture contents higher than 120% were too soft and too sticky to handle with safety. For optimum conditions in the low pressure filter presses used here, a moisture content of 120%, 1.8 times the liquid limit, for Speswhite Kaolin was chosen.

The clay was mixed in a Z-bladed mixer. This mixer has a capacity of about 10 litres, and each filter press has a capacity of about 3.5 litres. Therefore, when three filter presses were used simultaneously, the slurry was mixed in two batches. First, 4 litres of slurry was mixed for one filter press, and secondly, 8 litres of slurry was mixed for the other filter presses. The recipe for 4 litres of slurry is as follows:

Speswhite Kaolin powder, 2.5 kg  
de-aired water, 3.0 kg.

It is important to evacuate the air from the slurry during mixing. If there is air in the slurry, the cake cannot attain one hundred per cent saturation, and large pores form in the cake. In order to make the cake as completely saturated as possible, vacuum was applied during the mixing. The vacuum was about 20 in Hg (500 mm Hg).

Each batch of slurry was mixed for two hours.

After having been completely mixed, the slurry was put in the filter press. Care was needed to avoid trapping air within the slurry.

### 2.3.2 Cake Preparation

Three virtually identical low-pressure filter presses were used. Fig. 2.2

shows their general arrangement. The low-pressure filter presses had been designed to produce cakes of soils which were to be:

- 100 mm high
- 125 mm diameter
- uniform in internal structure
- similar from cake to cake.

These cakes were required to cut a series of identical samples 76 mm high x 38 mm diameter for triaxial testing. Each cake provided one sample. The samples used here were cut vertically, even though they also could be cut horizontally or inclined at any angle.

The filter press apparatus consists of four main parts: reservoir; pressure cylinder, sump; and loading system. The loading system is made up of an air-water cylinder, an air pressure regulator, and an air pressure gauge. The air-water cylinder is connected to the pressure cylinder; and the sump is connected to the reservoir.

The clay slurry is consolidated in the pressure cylinder between two porous stones. The pressure is applied to the slurry by driving the lower stone upwards by a piston under the action of pressurized water. This water is supplied from the air-water cylinder which has sufficient size to drive the piston from the extreme bottom to the extreme top of the pressure cylinder. Whilst the clay is being consolidated, the upper stone is held down by a top cap, which forms a part of the reservoir assembly. The water exhausted from the slurry passes upwards into the reservoir and downwards through the piston rod into the sump.

There are three valves in the cylinder. All of them are non-return valves;

and they should be such that their operation neither increases nor decreases the volume/pressure of the water in the cylinder.

Before starting the tests, the pressures required to move the piston against friction in the empty presses were measured. These values were added to the nominal pressures to give an empirical correction for friction, which was considered to be sufficiently accurate for the present purposes.

The pressure was increased by increments over 10 days, Table 2.2, and progress was monitored by the movement of the piston.

Table 2.2 Pressures Applied To The Press *kPa*

Nominal Pressure	Filter Press Number			Duration hours
	1	2	3	
12.5	24.5	24.5	22.5	24
25.0	37.0	37.0	35.0	24
50.0	62.0	62.0	60.0	24
100.0	112.0	112.0	110.0	168

The cakes produced were just firm enough to handle. This is because the pressure was limited for two reasons: to keep the degree of anisotropy of the cakes as low as possible; and to remain below the strength of the plastic of which the filter presses had been constructed.

#### 2.4 Triaxial Test

The normal height:diameter ratio of the triaxial test sample is about two, the benefit of which is that radial strains are much more uniform throughout the

central portion of the sample.

The triaxial test equipment employed here is shown in Fig 2.3. The samples used were cut to the size of 76 mm high x 38 mm diameter from the filter cakes using a cheese wire. The type of test chosen here was undrained normally-consolidated shearing, so triaxial pre-consolidation was applied using drainage from the bottom of the sample before shearing. The pre-consolidation of the sample is often carried out with a positive pressure applied to the drainage lines, so that when consolidation is complete, the pore water pressure is positive. Application of this back pressure has two advantages. First, it helps keep any dissolved air in the pore water in solution, thus preventing the formation of air bubbles. Second, in materials which dilate when sheared in undrained loading, the pore pressure will decrease, and the positive back pressure ensures that the absolute value of the pore pressure always stays above zero to avoid possible cavitation problems. Here, a back pressure of 50 kPa was applied.

The highest cell pressure was limited to 700 kPa by both the pressure system of the laboratory and the capacity of the triaxial cells. The cell pressures were applied in four stages. The timetable is given in Table 2.3.

Cell Pressure	kPa	100	200	400	700
Duration	Day	1	1	1	2

After consolidation, the deviator stress was applied to the undrained sample with pore pressure measurement at the bottom of the sample. The rate of loading in the undrained stage of the test will affect the measured pore pressures

due to three causes: time lag in the pore pressure measurement system; progressive equalization of non-uniform pore pressures; and rate dependent effects on the soil structure (Lee *et al*, 1983). Bjerrum (1972) reported that the rate of loading has an effect on undrained strength, typically increasing it in the order of 5% to 10% for each order of magnitude increase in strain rate. For the above reason, a strain rate of 0.15 mm/min was chosen.

In order to observe the microstructural changes of the clay during shearing, shearing was stopped at different strains. According to several pre-experiments, it was known that failure was achieved at about 14% strain. Thus, shearing was stopped at the following values of strain: 0%, 1%, 2%, 4%, 6%, 8%, 10%, 12%, around 14% (referred to 'failure'), and over 14% (referred to 'after failure').

When shearing was finished, the load was released. Then the cell pressure was gradually reduced to zero, one stage released each day in order to prevent any sudden change of pore pressure, Table 2.4. Then the sample was taken out immediately and cut into the sub-samples required for the preparation procedures described in the next chapter.

Cell Pressure	<i>kPa</i>	700	400	200	100	0
Duration	<i>Day</i>	2	1	1	1	1

## 2.5 Stress – Strain Characteristics

Fig.2.4 shows some typical stress–strain curves from normally consolidated

undrained triaxial tests. These curves give the stress-strain characteristics of Speswhite Clay under normally consolidated undrained shearing. When the strain is less than 2%, the stress increases linearly with the strain; then as the strain increases, the stress grows slowly; and the maximum stress is achieved at about 10% strain; for strains larger than that, there were three phenomena, these being stresses remaining unchanged, a little decreasing, and suddenly falling down with a failure plane building. A statistical analysis for the deviation of the stress-strain curves between samples was made, which showed that the deviation is within 5% possibility. The upper limit curve and lower limit curve are presented in Fig.2.4.

For comparison, some results of the University of East Anglia series are given in Fig.2.5, which are normally consolidated drained triaxial shearings; and Speswhite Kaolin was employed too. These curves show similar characteristics to those above: there is a very steep rise at the start, followed by a gradual curve, which either flattens out, or which may show a drop of stress at the highest strain reached (about 14%–18%) corresponding to the formation of a failure plane. Fig.2.6 shows the variation of volumetric strain with strain. Each point represents a separate test. The volume of the sample falls rapidly at first up to about 8 % axial strain. Therefore there is only a small further change in volumetric strain.

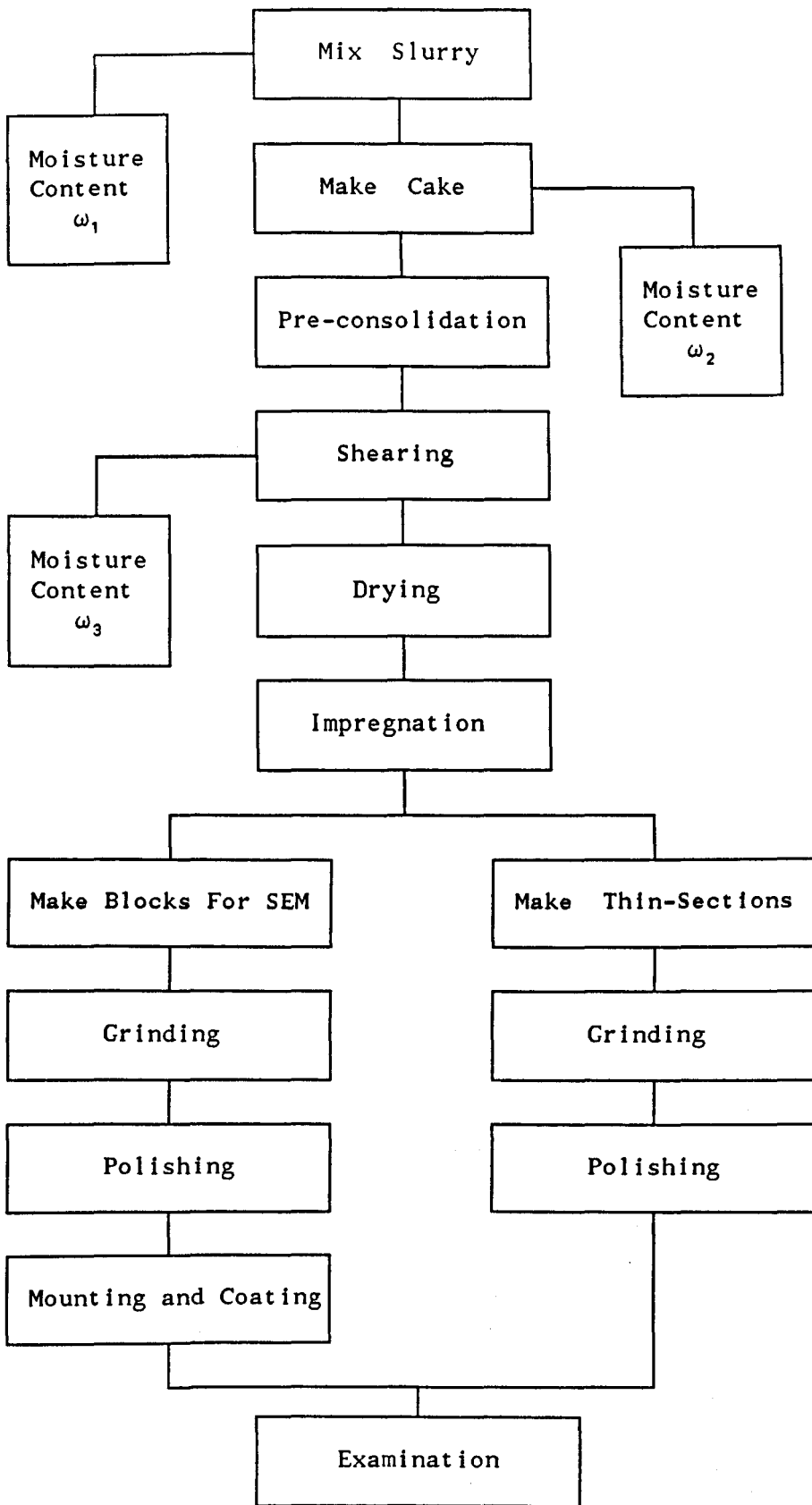


Fig. 2.1 Flow Chart of Experimental Programme

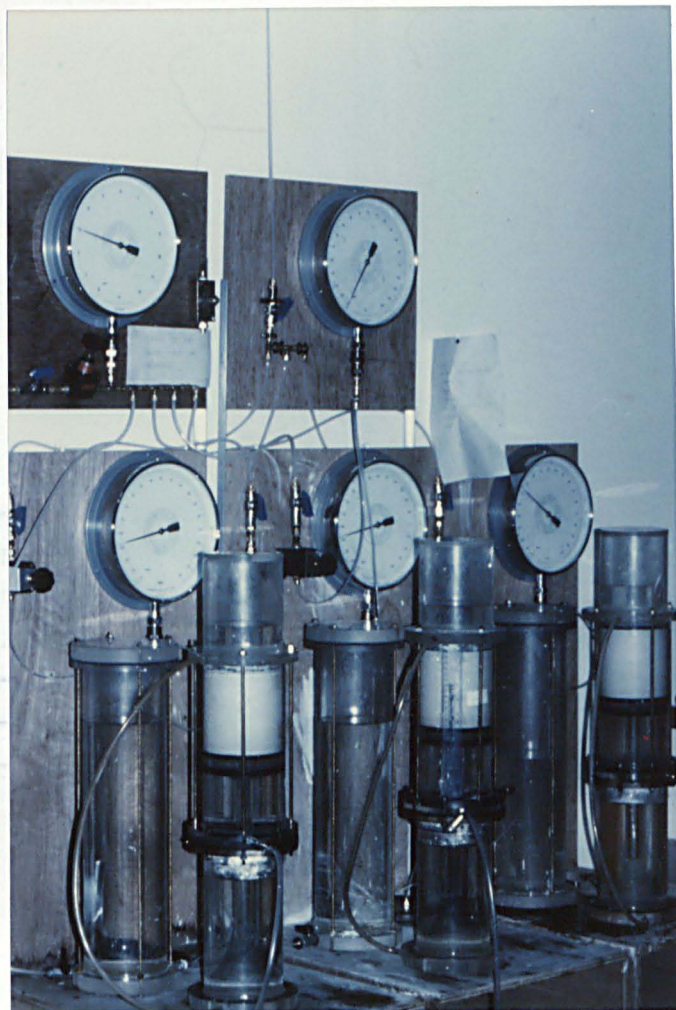


Fig. 2.2 The low-pressure filter press arrangement

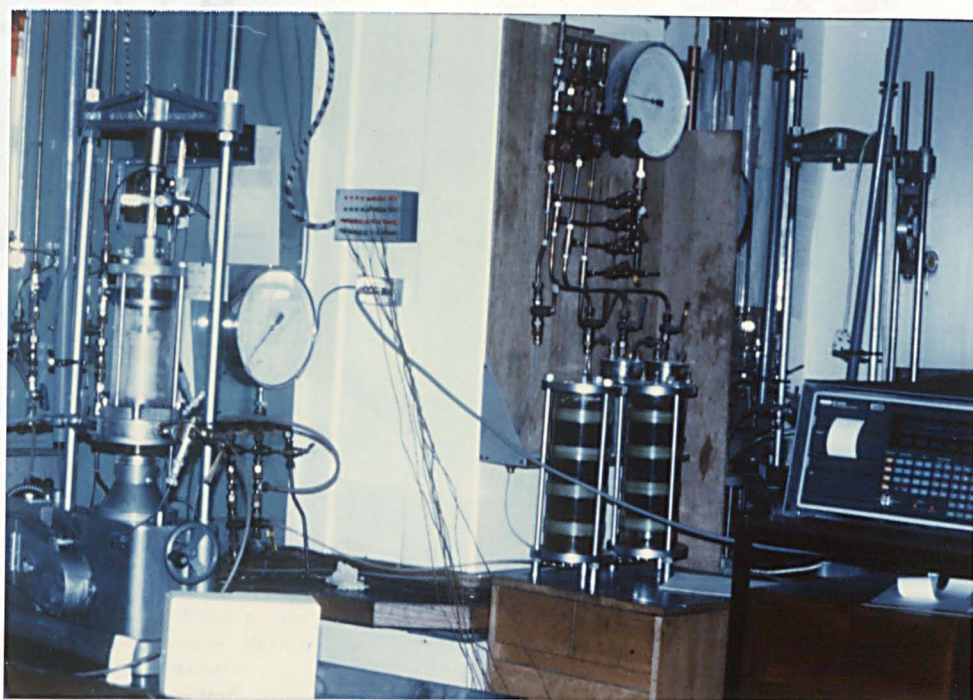


Fig. 2.3 The triaxial apparatus

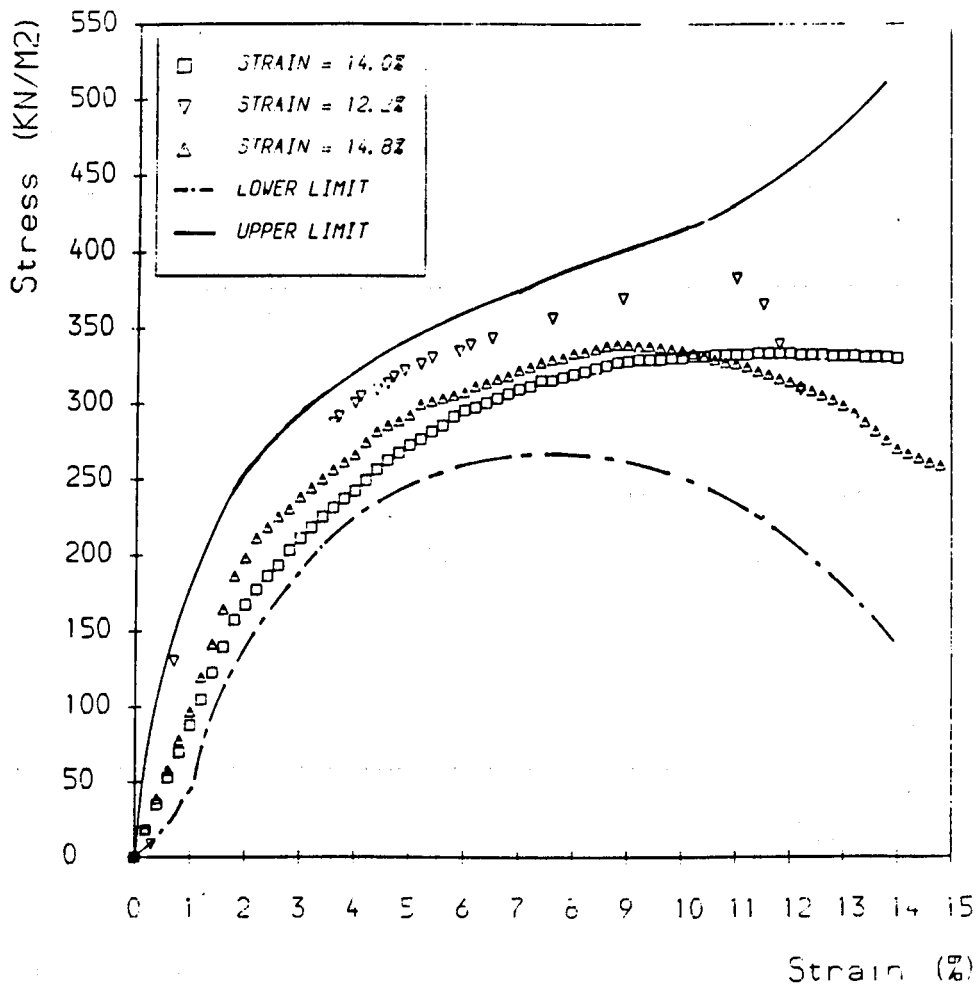


Fig.2.4 Stress-Strain Curves of Normally Consolidated Undrained Shear

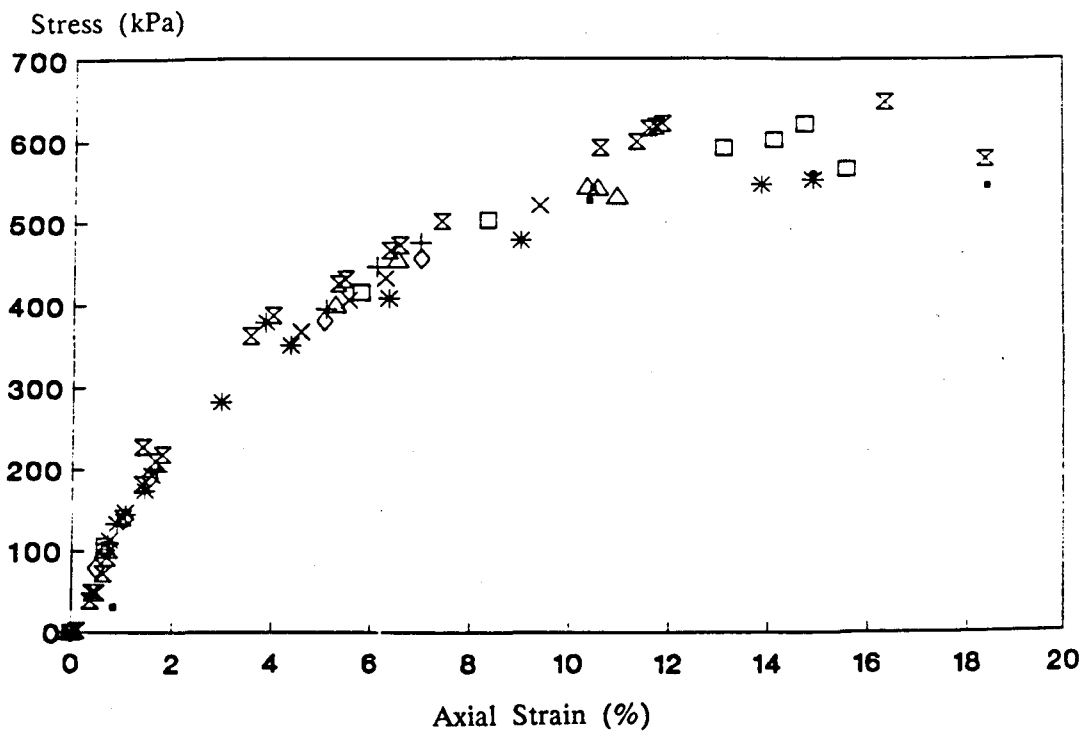


Fig.2.5 Stress-Strain Curve For Normally Consolidated Drained Shear  
(Reproduced from Smart and Tovey, 1989).

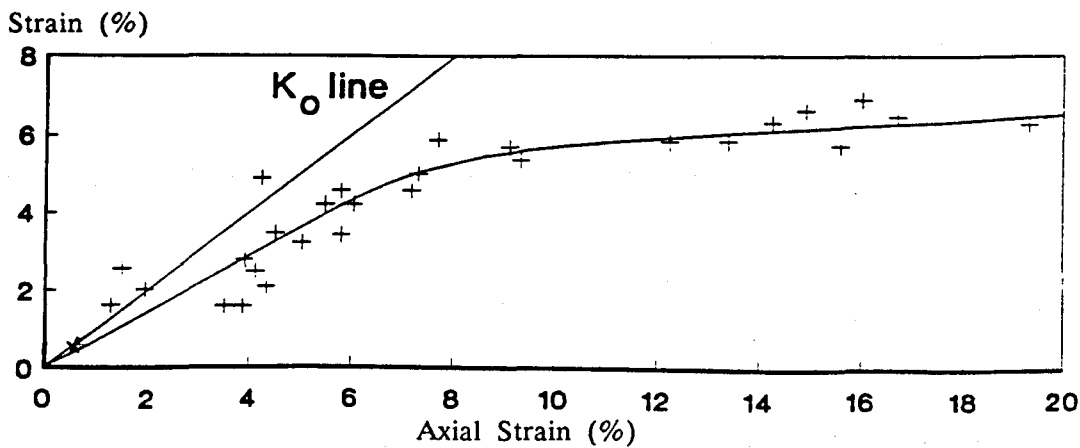


Fig.2.6 Volumetric Strain vs. Axial Strain for Normally Consolidated Drained Shear (Reproduced from Smart and Tovey, 1989).

## Chapter 3

### PREPARATION OF SAMPLE

#### 3.1 Introduction

The fabric of fine grained soils including kaolin clay cannot be studied directly, because of the difficulty of obtaining satisfactory, undisturbed samples. Preliminary sample preparation is necessary, so that the samples may be broken, cut open, sawn, or ground down to reveal true and undisturbed surfaces which are, expectedly, typical of the whole soil fabric.

The sample preparation procedures cover: removing water from the sample, which process is referred to as drying; impregnating the sample; grinding and polishing the impregnated sample. The impregnated sample is usually called a specimen.

Section 3.2 gives a brief review of various methods of preparing samples, and the procedures which were used in this research are described in Section 3.3.

#### 3.2 Review of Present Methods of Sample Preparation

Up to today, people have developed various methods of preparing samples in order to observe the most satisfactory surface. However, it seems impossible to avoid disturbing the soil structures at all during the processes of cutting or sawing samples etc., because these processes disrupt the soil.

Techniques of preparation have been reviewed by Smart and Tovey (1982),

FitzPatrick (1984) and Murphy (1986). General points relating to these techniques are discussed below, and the techniques actually used here are discussed in Section 3.3.

### 3.2.1 Drying

Four main methods of drying have been used up to the present. They are air-, freeze-, supercritical-, and substitution-drying. Removing water in wet soil results in some rearrangement of the particles, which may be caused by surface tension effects (Smart and Tovey, 1982). Pusch (1966) reports that thin slices of stiff clays can be examined at their natural moisture content by enclosing specimens in cells and using high voltage electron microscopy. This approach is not generally available, and one of the methods described below should be employed as a first step in the study of clay structures.

#### i. *Air-drying*

Air-drying methods including oven-drying are the easiest and cheapest methods. Drying at room temperatures may require a longer time to remove all the water from clayey materials, but the faster oven-drying may cause gross damage, and the high temperatures may cause not only considerable shrinkage but also mineralogical alteration to particles. From the viewpoint of studying structures of soils, a slow method seems to be preferred.

Because of its simplicity, air-drying has been most widely used in soil science (Borst and Keller 1969, Tovey 1971, Barden and Sides 1970, O'Brien 1972, Wong 1975, etc.).

*ii. Freeze-drying*

Freeze-drying was developed to avoid the damage caused by surface tension. The basic idea is that a very low temperature is employed to make all the water in the sample freeze rapidly, so that the water solidifies 'instantaneously' without disruptive crystal growth (Keinonen 1957; Williams 1964). However, freeze-drying is not as effective as expected. Rosenqvist (1959), Smart (1966c), Gillott (1969, 1970), and Tovey (1970), for example, have all studied and used freeze-drying techniques. Smart (1966c) reviews the subject and notes that in kaolin samples, freeze-drying induced cracking and the development of an artificial structure and of a "fluffy" appearance, although the drying apparatus has been improved since then. It still has the major disadvantage that only small volumes or thin samples can be dried without disruption of the structure. The principal difficulty occurs during freezing. The disruption is caused by ice crystal formation within the centre of the supposedly quickly frozen sample. Besides, this method needs expensive equipment.

*iii. Supercritical-drying*

Supercritical drying has been used in biological research to avoid disruptions of structure (surface tension and freezing effects) through the samples (Kistler 1932), and it has proved useful for soil (Gillott 1969, 1970).

The critical point of a liquid is defined as the temperature and pressure above which the physical properties of the liquid and its vapour are the same. For water, the values of temperature and pressure are 374°C and 21770 kPa (3266 lb/in<sup>2</sup>) respectively. It is obvious that above the critical point, surface tension can be eliminated, and so the original soil fabric may be better preserved

during the removal of the pore water. However, as mentioned above, the critical temperature and pressure of water are so high, even were alcohol to be substituted for the pore water, that the stability of the clay minerals would be in doubt (Smart and Tovey 1982). Bhasin (1975) has used supercritical-drying without replacing water, but apparatus would have to be specially built and very expensive. After comparing the air-, freeze-, and supercritical-drying, Gillott (1970) reported that volume change could not be eliminated, but that by avoiding air-drying it could be greatly reduced. Otherwise, the size of the sample for supercritical-drying would be quite small, usually only 5mm by 5mm by 20mm.

#### iv. Substitution-drying

Substitution-drying involves the replacement of pore water in soil by a liquid possessing a low surface tension, followed by air-drying. The substitution of a liquid with low surface tension before air-drying would reduce surface tension damage, but, the substitution itself might cause rearrangement of the particles. However, substitution-drying is sometimes considered the most suitable method for removing water from most samples of soil before impregnation (Murphy 1986).

The liquids used in substitution-drying might be acetone, alcohol (Singh 1969), dioxan and methanol (Greene-Kelly *et al*, 1970); but acetone, which has been used in the liquid phase (Miedema *et al*, 1974) or in the vapour phase (FitzPatrick 1984), is the most commonly used solvent for its rapid evaporation and lower price. Another reason for preferring acetone to other liquids, is that acetone has a very good resin solvency.

During the process of replacement of soil water, major damage can be

caused if a pure acetone is used at the beginning of the removal of soil water, because the water in the sample takes up acetone less quickly than water diffuses from the sample. Murphy (1986) suggested that a much faster 'drying' schedule is possible by more frequent acetone changes and or by causing gentle movement of the acetone during exchange, using a magnetic stirrer.

### 3.2.2 Impregnation

In this thesis, impregnation means that the sample is solidified by filling its pores with a substance which, in the first instance, has a low viscosity and which can be hardened. Therefore, impregnation reinforces the structure of the soil which is to be examined in transmission electron microscopy, scanning electron microscopy, or optical microscopy. Usually, the impregnating agents are insoluble in water, so they should be substituted for the pore water in wet soil samples via one or more intermediate organic solvents. The principle involved is that the first solvent is miscible with water, which it gradually replaces in the pores, while the impregnating material is miscible with the final solvent, usually acetone or methanol, which evaporates leaving the sample impregnated.

In general, the material used for impregnating samples should have the following properties and advantages:

1. low viscosity;
2. miscible with acetone to lower its viscosity;
3. harden in normal conditions;
4. not change the physical structure of the sample;
5. isotropic and colourless in thin sections, with a refractive index of about 1.54.

According to the above conditions, no material can be completely suitable. Up to today, the materials to be used for impregnating samples, usually, have been Vestopal W, Carbowax 6000, epoxy resins, and monomeric resins. All of them have both advantages and disadvantages. Vestopal W is the first choice for wet and large samples (Smart 1966a). Epoxy resins are normally suitable for dry soil. Carbowax 6000 is miscible with water, so that it is much better than other resins in this respect, but the sample is soft after impregnation by it, and it is easy to damage the structure of soil during later treatment. As for monomeric resins, it has been suggested that they should not be used, because of a health hazard, even though they have excellent fluidity to allow them to impregnate into the pores of soils.

Dynamic impregnation was described by De (1970). He found that this process increased the rate of impregnation, but that samples suffered erosion at the edges. During the operation, samples were inclined at 2–3°.

### 3.2.3 Grinding and Polishing

After impregnation, samples of soil should be cut or sawn into specimens of certain sizes which will be used during examination for optical microscopes or scanning electron microscopes or transmission electron microscopes. When cutting or sawing samples, the structures of the surfaces of soil samples will be disturbed ineluctably. In order to get a true and smooth surface to examine, the specimen still needs to be ground and polished finally. A thin section is needed for optical microscopy in transmitted light.

### i. *Grinding and Polishing the Impregnated Specimen*

Specimens are ground flat by hand or by machine, using either loose powders, grinding papers or grain-impregnated lapping plates or cups. There are advantages and disadvantages to all those methods. Firstly, the obvious marks on the surfaces of the specimen chosen are removed using coarse abrasive. Progressively finer grit sizes are used to eliminate coarse scratches. Some pressure must be applied to the specimens during grinding to smooth flat faces.

The main problem during grinding is the introduction of grinding material into the impregnated specimen, particularly into the resin-filled pores, especially when loose powders are used. For this reason, the pressure should be as low as possible and also enough lubricant should be applied. After grinding, the specimens should be cleaned carefully. When using progressively finer grain sizes, the different grain grades must be kept separate to avoid unwanted scratches.

After grinding, the specimen is easily polished to a glass-like finish. Usually, progressively finer high quality diamond pastes (6  $\mu\text{m}$ , 3  $\mu\text{m}$ ) or Jewellers' putty powder (tin oxide) lubricated by cutting oil or kerosene, are used for polishing. The polish media also must be kept free of coarser grains to avoid scratches.

### ii. *Making Thin Section*

After the above steps, a flat clean surface of the impregnated sample has been obtained, as is required for bonding to glass before a thin section can be made. However, the degree of polishing for this purpose is not high, because a well polished face does not bond strongly with glass.

The procedure of making a thin section from a specimen which already has a flat clean surface includes two steps: bonding the flat specimen to a glass slide; and finishing the thin section.

Before bonding, the flat faces of specimens to be bonded and the glass slides should themselves be cleaned and dried. Any grit or dust locked between the specimen and glass will remain visible in the finished section. For the same reason, the bonding procedure should be carried out in a dust-free environment. The bonding resin should be fast-setting and have the same refractive index as the impregnant. The sizes of glasses are up to 12.5 x 10 cm for convenience. Recommended thicknesses for different slide areas are 1.5 mm for slides 12.5 x 10 cm, 1.2 mm for slides 10 x 8 cm, 1.0 mm for slides 7.5 x 5 cm and 0.8 mm for slides 5 x 3 cm. Care must be taken. The bonding technique is a delicate but simple operation, which requires a little practice to perfect.

Murphy (1986) suggests that the two most practical ways of removing most of the surplus impregnated material from the glass slide are by sawing or by lapping on a surface grinding machine. For removing the bulk of the mounted slice and finishing to a uniform 25  $\mu\text{m}$  thickness, the techniques can be fully automatic, semiautomatic or manual. Manual work is tiring and time-consuming, but, the final stage of lapping, from about 40–100  $\mu\text{m}$  to 25  $\mu\text{m}$  thickness, is best done by hand.

Since most thin sections are examined optically it is necessary to protect them. Most sections are therefore either sprayed with lacquer or covered with sheets of very thin glass (cover slips).

### 3.3 Sample Preparation

#### 3.3.1 Introduction

In the present case, specific advice was available, because the University of East Anglia was also using Speswhite Kaolin, and McConnachie (1971) and Smart and Dickson (1978) had used SPS Kaolin, which is similar. Even so, some preliminary experimentation was required before the following techniques were adopted.

Several substitution-drying methods were tested. In the beginning, a mixture of ethanol and water was employed, but large cracks were caused in the sub-samples (Fig.3.1). Then, the mixture of methanol and water was tried, but the cracks still could not be ignored. Although the University of East Anglia was reusing used acetone as the initial substitution liquid, and then going to fresh acetone, with which they have obtained satisfactory results, the large cracks still appeared in experiments here. After these failures, the procedure as follows was adopted finally. Even though some cracks were still found, they were smaller and could be neglected (Fig.3.2).

In the investigation of impregnation, following the procedure of the University of East Anglia, Araldite was tried first. It was found that large samples could not be impregnated fully when Araldite was used, although it was quite hard. Samples impregnated with Vestopal W were softer than those impregnated with Araldite, but were completely impregnated. The difference in hardness was considered to be immaterial here and so Vestopal W was used.

### 3.3.2 Pore Fluid Substitution

Before impregnation, acetone was substituted for the pore water, because water stops the resin from hardening. The apparatus used here is shown in Fig. 3.3. Sub-samples were obtained from triaxial test samples. After the triaxial test, the samples were cut into halves longitudinally using a cheese wire. If a failure plane or other symmetrical deformation was present, the halves were cut to bisect this deformation symmetrically. From each half sample, two sub-samples can be cut from the faces located within a few millimeters of the centre of the sample. The face is parallel to the plane of bisection (Fig.3.4).

The sub-sample was put into a small dish (Fig.3.3). Clean sand was placed around the sub-sample to restrain it. The small dish was placed in a crystallizing dish, which was fitted with a drain, consisting of a glass spout, rubber tube and screw clamp. The crystallizing dish was filled gently from a burette, which was held by a clamp. Care was taken to avoid adding the fluid directly to the small dish.

The crystallizing dish was filled first with a mixture of 25% acetone and 75% distilled water; then the liquid was changed to 50% solution of acetone daily; then to 75%, and 100%; finally, the pure acetone was changed three times or more every two days. It is very important that pure acetone must be changed enough times (at least three times) to guarantee that the water in the sub-sample is completely replaced by acetone. If any water still exists in a sub-sample, the sub-sample can not be impregnated by Vestopal. To preserve the sample from disruption by surface tension, the crystallizing dish was drained by unscrewing the clamp, so that the small dish was not emptied. The crystallizing dish must be completely covered with a watch glass except whilst

refilling, otherwise the acetone evaporates rapidly.

### 3.3.3 Impregnation

The mixture of Vestopal and acetone must be gently added directly to the small dish from which most of the acetone has first been removed. A typical recipe is Vestopal W, 100, initiator, 1.0, activator, 0.5 by weight, acetone, 200–300 part by volume (Vestopal is obtained from TAAB Laboratories Equipment Limited). The acetone was then allowed to evaporate. As it evaporated, the dishes were topped up daily, taking care to keep the sub-sample submerged, this step took over two weeks. The Vestopal impregnated sample then hardened at room temperature. Finally, the Vestopal was cured at 60° C for 48 hr.

### 3.3.4 Grinding and Polishing

After curing, the impregnated samples were sawn into specimens. Two specimens were cut from each impregnated sample and were used to provide a block for examination by scanning electron microscopy and a thin section for optical microscopy respectively. The sizes of specimens were 15 mm x 15 mm x 5 mm and 20 mm x 20 mm x 5 mm respectively. Both specimens were marked to show the top, *i.e.* the surface on which the stress  $\sigma_1$  was applied. Specimens for thin sections were ground and polished on one surface, then sent to a specialist laboratory for making into thin sections. Blocks for scanning electron microscopy were ground and polished on one surface only as described below.

*i. Grinding*

The specimen was held in the fingers and rubbed against a sheet of fine emery cloth (No. 240, from Engis Ltd.) laid horizontally on a glass as the first step. The pressure was kept very light and the speed low. At the second step, silicon carbide (No. 600, from Engis Ltd.) was used on a plate glass surface. With impregnated samples, water was used as a lubricant to keep down the temperature, in an attempt to minimize melting of the surface. The main problem during flattening was the introduction of grinding material into the impregnated soil. It is suggested that the pressure should be low, the grinding time should not be too long, and enough lubricant should be added. Specimens were carefully ground until all the criss-cross markings were removed, which usually took a few minutes. Before beginning the next step, the specimens were thoroughly cleaned to avoid unwanted scratches caused by carrying over large grits.

*ii. Polishing*

Progressively finer high quality diamond pastes (6  $\mu\text{m}$ , 3  $\mu\text{m}$ ) lubricated by Hyprez fluid were used for polishing (these materials are supplied by Engis Ltd.). Firstly, 6  $\mu\text{m}$  diamond paste was used. The polishing time was 10 minutes. Then 1  $\mu\text{m}$  diamond paste was used for 7 minutes. The applied pressure was kept low to avoid damaging the surface. The polishing media must be kept free of coarser grains to avoid scratches, so the specimens were thoroughly cleaned of polishing media after each step to avoid contamination.

The polished blocks for scanning electron microscopy were mounted on specimen stabs using quick drying silver paint (supplied by AGAR Scientific LTD.)

and then coated with carbon ready for microscopy.

The observations from the thin section by optical microscopy and from the polished blocks by scanning electron microscopy are described in Chapters 6 and 7 respectively.

### 3.4 Conclusion

For different types of soils the technique of preparation of samples for optical microscope and scanning electron microscopy may be different, but for the kaolin used in this research, the techniques mentioned above provide high quality samples. The flow chart of the procedures is given in Fig.2.1.

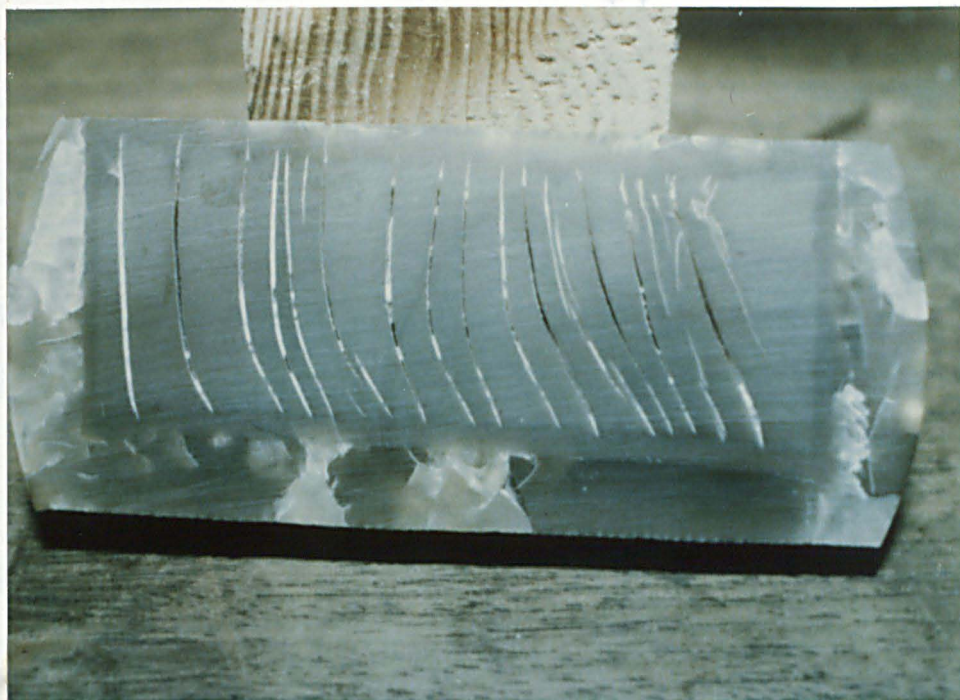


Fig.3.1 Failed Substituted Sample.



Fig.3.2 Successful Substituted Sample.

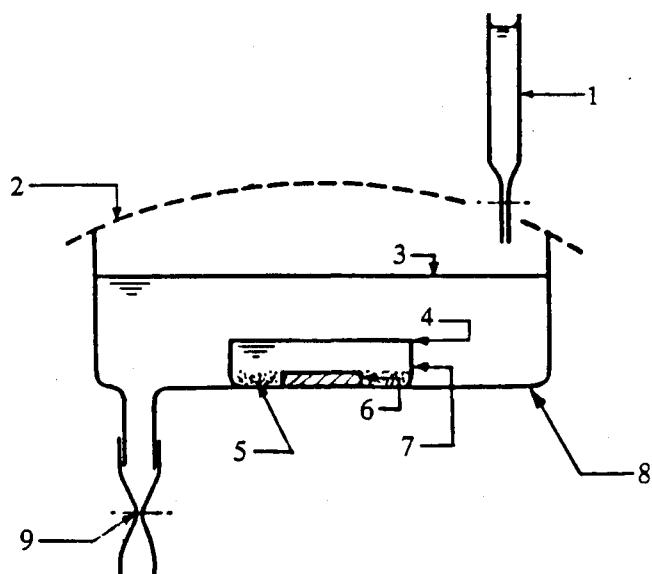


Fig.3.3 Apparatus for Impregnation, (reproduced from Smart, 1967).

Note: 1—burette, 2—watch glass, 3—usual level of fluid, 4—level before refilling, 5—clean sand, 6—sample, 7—small dish, 8—crystallizing dish, 9—screw clamp.

Not to scale.

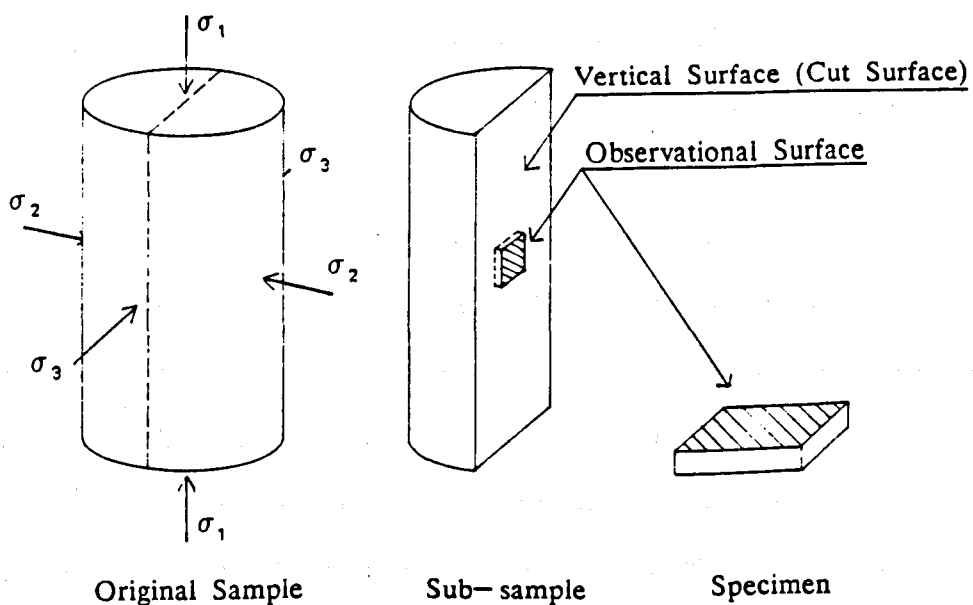


Fig.3.4 Illustration of Observed Surfaces of Sample.

## Chapter Four

### METHODS OF OPTICAL MICROSCOPY

#### 4.1 Introduction

Mitchell was the first to apply the technique of optical microscopy to the investigation of soil structure in geotechnical engineering in 1956 (Mitchell, 1956). Much use has been made of optical microscopy since then (Wu, 1958, Smart, 1966a; Tchalenko, 1967; others). The usual technique and the one which was used here employs thin sections. The technique for making thin sections has been improved since 1956, and a brief review of developments was given in Chapter 3.

The technique for observation of micro-structural features in thin sections of clay is based on the optical properties of clay particles. It is well known that a platy kaolin particle is optically anisotropic and possesses three approximately mutually perpendicular optical axes: two almost in the plane of the particle, which are called section axes in this thesis, and one almost at right angles to this plane. The refractive indices in the directions of the section axes are approximately equal and significantly different from that in the third axial direction. When a single particle is viewed between crossed polars, it may or may not exhibit extinction and illumination; but when a thin section is examined, it transmits a variable intensity of light depending on: the orientation of the optical axes of the particles in the thin section, the refractive indices of the mineral, the thickness of the thin section, the wave length and the intensity of the light. This transmitted intensity varies as the thin section is rotated with respect to the direction of polarisation.

For a certain thin section, assuming that its thickness is uniform, under a certain light, the intensity of light transmitted through the thin section depends only on the orientation of the optical axes of the particles in the thin section and the related positions of the optical axes of the particles and of the direction of the light. Thus, if kaolinite particles are arranged in a random style within a sample, a thin section in any direction through the sample does not exhibit extinction or illumination, since the optical axes of the particles are also distributed randomly. When such a thin section is rotated between crossed polars, the intensity of transmitted light remains constant throughout the  $360^\circ$ . If the particles are oriented with their planar surfaces parallel, extinction and illumination will occur in thin sections cut from the sample in particular directions. When a thin section is cut parallel to the orientation planes and viewed between crossed polars, no change shows in illumination with rotation, since the refractive indices in the directions of the section axes of the particles are approximately equal; but, when a thin section is cut normally to the plane of preferred orientation, four stages of extinction and illumination occur between crossed polars, since the optical axes of the particles lie in preferred directions (Fig. 4.1).

Hence, measurement of the transmitted light intensities may be used as an indirect measurement of the particle orientation. This Chapter gives a review of a previous method and introduces three new and improved methods.

#### 4.2 A Previous Method — Polarising Micro-Photometric Analysis (PMPA)

For a microscope with crossed polars and a thin section between them, for the intensity of light, the transfer function is (e.g. Smart, 1966a):

$$I = 0.5 \sin^2 2\theta \sin^2 \delta/2 \quad (\text{B.2}),$$



practice, because of slight asymmetry of the measurements, an average of four maxima and an average of four minima are used.

By means of the microphotometer, the average orientation direction of the particles can be determined too. A full-wave compensator could be used to locate the direction of preferred orientation by comparing the colours seen with the colours of failure planes. However, there is a small risk of an error of  $90^\circ$  in any single observation.

In observations described here, the objective was x10 and the field of view was 1.5 mm diameter.

#### 4.3 Polarising Micro-Photometric Mapping (POLMAP)

When viewed between crossed polars, the matrix of clay soil often shows diffuse light and dark patches which represent information which has been difficult to extract by conventional microscopy. By using a special type of optical microscopy and computer analysis system, the following new method has been developed.

From Equation B.2 (Appendix B), it is known that extinction occurs only when the section axes are parallel to or perpendicular to the axes of polars when a thin section is viewed between a crossed polars. And, when a quarter-wave plate is used in such a position that the angle between the axes of the quarter-wave plate and the axis of the polarizer is  $45^\circ$ , the transfer function becomes:

$$I = 0.5 (1 - \sin 2\theta \sin \delta) \quad (\text{B.3}).$$

In this case, full extinction occurs when the angle between the section axes and

the axis of the polarizer becomes  $45^\circ$  and  $\delta$  is  $\sin^{-1} 1$  or  $135^\circ$  and  $\delta$  is  $\sin^{-1} -1$  (see Appendix B).

In Fig.4.2, a Leitz Dialux-pol microscope is shown, in which the polariser, the analyser, and a slot for a compensator, are all linked together by an arm and can be rotated synchronously. The Leitz microscope used here has another slot which is fixed in the body of the microscope, and which must not be used here. Most of the measurements discussed here were made using this microscope; some were made using a Prior-Swift MPB124 Polar Microscope in which similar synchronous rotation was achieved by internal gearing.

A failure plane is shown here because its inclusion may help to explain the method. Figs. 4.3.a and 4.3.b both show the same area of a thin section of sheared kaolin examined between crossed polars. In Fig.4.3.a, the synchroniser was set at  $45^\circ$ , and the polars were crossed on the diagonals, so the bright areas are areas in which the clay particles are aligned either horizontally or vertically (with respect to the field of view). In Fig.4.3.b, the synchroniser was set at  $90^\circ$ , and the polars were crossed parallel to the sides of the micrograph, so the bright areas are areas in which the clay particles are aligned diagonally. In the first stage of analysis, these two microphotographs were digitised. What is called digitising is dividing each micrograph into  $512 \times 512$  pixels, *i.e.* 'points', and also dividing the intensity of illumination into 256 levels, which are called grey levels; then the grey level is measured at every pixel by using a Micro-Semper image analysis system. The digitised area used here was  $47.0 \mu\text{m}$  square, giving a spacing between pixel centres of  $0.0917 \mu\text{m}$ . These two digitised micrographs are denoted x1 and x2 respectively. Comparison of them, then, distinguishes between areas oriented 'on the square' and 'on the diagonal'. Each pixel was coded as follows:

- 1 if brighter in  $x_1$  than  $x_2$ , on the square;
- 2 if brighter in  $x_2$  than  $x_1$ , on the diagonal;
- 0 otherwise, i.e. undecided.

After this preliminary coding, four more digitised micrographs were used to distinguish horizontal from vertical and down-left from down-right. All these micrographs were taken with a quarter-wave plate inserted in the compensator slot and rotating synchronously with the polars.

In the second stage of analysis, only pixels coded 1 were considered, and two micrographs taken with the synchroniser set at  $135^\circ$  and  $45^\circ$  were used. These two micrographs are denoted  $q_1$  and  $q_3$  respectively. In one of these micrographs, the brighter areas are horizontal, and in the other they are vertical; a pragmatic method of deciding which is which is to experiment with failure planes in which the particle alignment may be assumed safely. Thus, the pixels which had originally been coded 1 were recoded as follows:

- 1 if brighter in  $q_1$  than  $q_3$ , i.e. horizontal;
- 3 if brighter in  $q_3$  than  $q_1$ , i.e. vertical;
- 0 otherwise, undecided.

In the final stage of analysis, each pixel coded 2 is recoded using two micrographs with the synchroniser set at  $90^\circ$  and  $0^\circ$  and labelled such that the new coding is:

- 2 if brighter in  $q_2$  than  $q_4$ , i.e. down-left;
- 4 if brighter in  $q_4$  than  $q_2$ , i.e. down-right;
- 0 otherwise, i.e. undecided.

Figs. 4.3.c - 4.3.f show horizontal, down-left, vertical, and down-right

areas respectively. During analysis, a convenient method of presenting the results is to colour the pixels as follows:

1	horizontal,	red;
2	down-left,	yellow;
3	vertical,	green;
4	down-right,	blue;
0	undecided,	black.

Fig. 4.4 shows the result of the analysis. The colours were chosen because thin sections such as the one used here frequently show yellow and blue for the pixels coded 2 and 4 respectively when viewed in white light with the synchroniser set at  $90^\circ$  and using a full-wave compensator. Under those conditions, the other areas tend to be pink, leading to green vertical and red horizontal, (for practical reasons, Fig.4.4 was taken from one microscope and Fig.4.5 from the other). In theory, for the analytical method used here, monochromatic light with a wave-length matched to that of the quarter wave plate should be used; but in practice, white light was found to be more convenient and to give similar results.

The overall anisotropy of the field of view may be assessed by considering the number of pixels mapped into each direction: undecided, horizontal, down-left, vertical, down-right. For the field discussed here, the result was:

undecided	horizontal	down-left	vertical	down-right
525	237309	2193	348	21769

Following the PMPA method above, an Anisotropy Index,  $A_2$ , obtained by this method, polarising micro-photometric mapping (PMPM), may be defined as follows:

$$A2 = \frac{|(H + V) - (L + R)|}{H + V + L + R} \quad (4.2)$$

where H, V, L and R are respectively the number of pixels mapped into the directions: horizontal, vertical, down-left and down-right. In the above example approximate estimates are:

$$L + R = 23962,$$

$$H + V = 237657,$$

leading to

$$A2 = 0.81.$$

The Anisotropy Index, A2, obtained from POLMAP can be compared with that given by polarising micro-photometric analysis (PMPA), A1. For example, for the same area, A1 = 0.7 which is a little lower than A2. These two values of A are not strictly comparable, because the PMPA measurement has been taken over a wider field of view than the POLMAP measurement. Further, the directions used for POLMAP were chosen arbitrarily beforehand, whereas PMPA showed the direction of maximum preferred orientation to be  $10^\circ$  to the horizontal within a few degrees.

POLMAP also gives extra information on sizes of patches which may be very useful in the analysis of images, and which is called CHORD SIZE in this thesis. As mentioned above, a result of analysis was obtained, in which each pixel was coded as 1, 2, 3, 4 or 0. Then, the number of pixels for every patch can be counted at every line, so, an average of the numbers of pixels in the horizontal direction can be calculated, and this is defined as horizontal chord size. In the same way, vertical chord size can be obtained too. In both cases, the average was first calculated neglecting the incomplete chords at the ends of the lines;

then, if these were greater than the average, the average was recalculated using the end chords. For the example above, the chord sizes are 62 for the horizontal and 56 for the vertical.

Two other new methods are indicated in the next Section.

#### 4.4 Advanced Polarising Micro-photometric Mappings (POLMAP4 and POLMAP3)

##### 4.4.1 POLMAP4

When a parallel beam of monochromatic light passes through a polarizer, a thin section, a quarter-wave plate, and an analyser which is crossed with the polarizer, as mentioned above,  $I$ , the transfer function of the intensity of the light is as follows:

$$I = 0.5 (1 - \sin 2\theta \sin \delta) \quad (\text{B.3}),$$

where  $\theta$  now refers to the inclination of one of the section axes of a pixel, see Appendix B. Then, suppose that the synchroniser is set in turn at  $0^\circ$ ,  $45^\circ$ ,  $90^\circ$ , and  $135^\circ$ , then, the intensity of the light at each setting may be calculated from the following functions.

$$I_0 = 0.5 (1 - \sin 2\theta \sin \delta) = q_2 \quad (\text{B.3a}),$$

$$I_{45} = 0.5 (1 - \cos 2\theta \sin \delta) = q_3 \quad (\text{B.3b}),$$

$$I_{90} = 0.5 (1 + \sin 2\theta \sin \delta) = q_4 \quad (\text{B.3c}),$$

$$I_{135} = 0.5 (1 + \cos 2\theta \sin \delta) = q_1 \quad (\text{B.3d}).$$

Therefore,

$$\tan 2\theta = \frac{I_{90} - I_0}{I_{135} - I_{45}} \quad (\text{B.3e}),$$

$$\sin \delta = [(I_{90} - I_0)^2 + (I_{135} - I_{45})^2]^{1/2} \quad (\text{B.3f}).$$

After all of the four micrographs, q1, q2, q3, q4, have been digitised, by using Eqs.B.3e and B.3f, the direction of preferred orientation at each pixel can be obtained. For example, Fig.4.6 shows the polar histogram of angles from the same area as was used when discussing POLMAP. This new method, called POLMAP4, gave the direction of maximum preferred orientation to be  $9^\circ$  to the horizontal.

For mapping, the degrees were divided into groups, which are horizontal (from  $0^\circ$  to  $22.5^\circ$  and from  $157.5^\circ$  to  $180^\circ$ ), vertical (from  $67.5^\circ$  to  $112.5^\circ$ ), down-left (from  $22.5^\circ$  to  $67.5^\circ$ ), and down-right (from  $112.5^\circ$  to  $157.5^\circ$ ) respectively, each group being coloured in the same colours as for POLMAP (Fig. 4.7). Comparison of Fig.4.4 and Fig.4.7 gives very satisfactory results. If desired, the degrees could be divided into a larger number of groups, say 8 or 12, for a finer mapping.

Taking the analysis further, a new index 'Consistency Ratio' (see Curray, 1956) is defined as:

$$CR = (S_x^2 + S_y^2)^{1/2} / S \quad (4.3a),$$

$$\bar{\theta} = 0.5 \operatorname{tg}^{-1} (S_y/S_x) \quad (4.3b)*,$$

where: the assumed intensity at each pixel is a unit vector,  $S_x$  is the sum of the components on the horizontal axis at every decided pixel after doubling the angle, *i.e.*,  $S_x = \cos 2\theta_1 + \cos 2\theta_2 + \dots$ ;  $S_y$  is the sum of the components on the vertical axis at every decided pixel after doubling the angle, *i.e.*,  $S_y = \sin 2\theta_1 + \sin 2\theta_2 + \dots$ ; and,  $S$  is the sum of the unit vectors for all decided pixels. The Consistency Ratio reflects the degree of preferred orientation of particles in the viewed area. In this example, CR is 0.9, a little higher than A2, and  $\theta$  is  $7^\circ$ .

\* Labelled undecided if  $S_x, S_y$  both small.

## 4.4.2 POLMAP3

POLMAP3 comes from the same theory as POLMAP4 and produces the same results from only three micrographs. According to Eq.B.3, when the synchroniser is set in turn at  $0^\circ$ ,  $120^\circ$ ,  $240^\circ$ , the intensities of the light through the thin section are determined by the following functions respectively:

$$I_0 = 0.5 (1 - \sin 2\theta \sin \delta) \quad (\text{B.3a}'),$$

$$I_{120} = 0.25(2 + (\sin 2\theta + \sqrt{3} \cos 2\theta) \sin \delta) \quad (\text{B.3b}'),$$

$$I_{240} = 0.25(2 + (\sin 2\theta - \sqrt{3} \cos 2\theta) \sin \delta) \quad (\text{B.3c}').$$

Therefore,

$$\text{tg } 2\theta = \frac{I_{120} + I_{240} - 2I_0}{\sqrt{3} (I_{120} - I_{240})} \quad (\text{B.3d}'),$$

$$\sin \delta = \frac{2}{3} [(I_{120} + I_{240} - 2I_0)^2 + [\sqrt{3} (I_{120} - I_{240})]^2]^{1/2} \quad (\text{B.3e}').$$

Fig.4.6 shows the polar histogram of angles from POLMAP3 for the same area as above, which has very good agreement with the result from POLMAP4.

By the same method, the Consistency Ratio may also be calculated from POLMAP3. POLMAP3 requires three micrographs,  $q_0$ ,  $q_{120}$ , and  $q_{240}$  for Prior-Swift MPB124 Polar Microscope. For the Leitz Microscope, three micrographs  $q_0$ ,  $q_{120}$ , and  $q_{60}$ , may be used, because  $q_{240}$  is unavailable and  $I_{60} = I_{240}$ .

Although POLMAP3 requires fewer micrographs than either POLMAP or POLMAP4, the data required for POLMAP4 had already been measured for POLMAP. Thus, it was convenient and saved time to use POLMAP4 in this

thesis.

#### 4.5 Discussion

The comparison of the two Anisotropy Indices and the comparisons of the Consistency Ratio with the Anisotropy Index,  $A_1$ , are shown in Figs.4.8 and 4.9, which demonstrates the relations between these parameters. The Consistency Ratio was always larger than either of the Anisotropy Indices  $A_1$  and  $A_2$  (Fig.4.8). Referring to the calculation in Appendix C, which considers two approximate distributions of the number of pixels inclined at angle  $\theta$  from the experimental distributions, the Consistency Ratio CR is more sensitive to the degree of anisotropy than are the Anisotropy Indices. These analyses show that the Anisotropy Indices depend not only on the 'strength' of anisotropy but also on the 'type' of anisotropy. Therefore, although it must be remembered that the true distributions may be much more complex than those used in Appendix C, it seems that the Consistency Ratio is a more reasonable parameter for measuring the degree of anisotropy, even though the Anisotropy Index is more convenient in some cases.

The Anisotropy Index,  $A_2$ , measured from POLMAP, was higher than the Anisotropy Index,  $A_1$ , measured by the photometer (Fig.4.9). This is believed to result from the difference in the areas examined by these methods, the larger area used by the photometer having an averaging effect.

Comparison of the preferred orientations measured by PMPA and POLMAP4 is shown in Fig.4.10, in which each point shows the modulus of the average of the inclinations from the horizontal for the five fields measured for each thin section by PMPA (photometer) plotted against the corresponding values for the

---

four fields measured by POLMAP4. The scatter is attributed to the natural variability of the material and to the small number of fields which could be measured for each thin section. Thus, in some of the subsequent analysis, the modulus of the average of all nine fields will be taken as the best available measurement of preferred orientation obtained by optical microscopy.

The new computerised methods provided a readily perceived image and more information than did the older methods. All of the thin sections for the normally consolidated undrained series were measured using PMPA, POLMAP, and POLMAP4; and all of the thin sections from the University of East Anglia were measured using PMPA and POLMAP. The results will be discussed in Chapter Six.

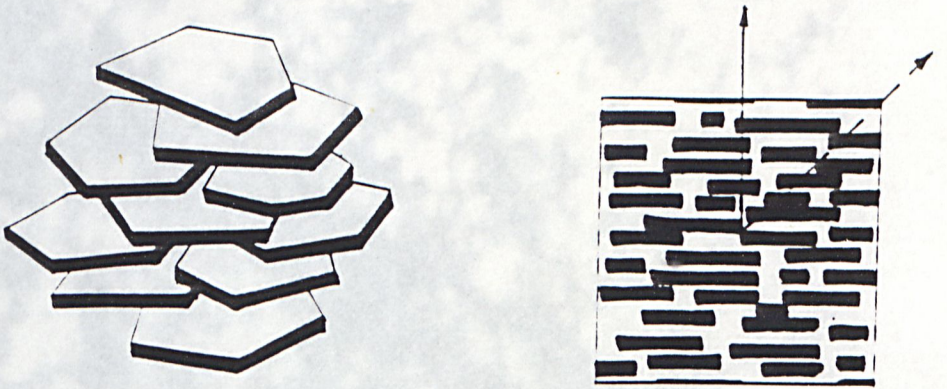


Fig.4.1 Illumination of Optical Axes of the Particles.



Fig.4.2 Leitz Dialux-pol Microscope

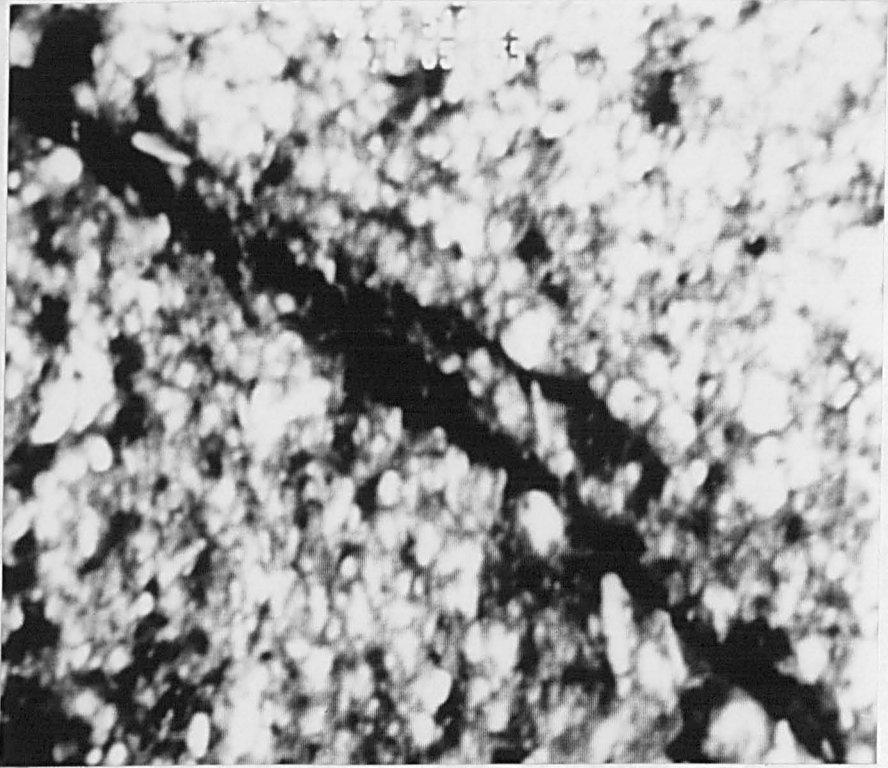


Fig.4.3.a Optical Micrograph of Polars Crossed on the Diagonal, x1.

with Quarter Wave Plate. 42

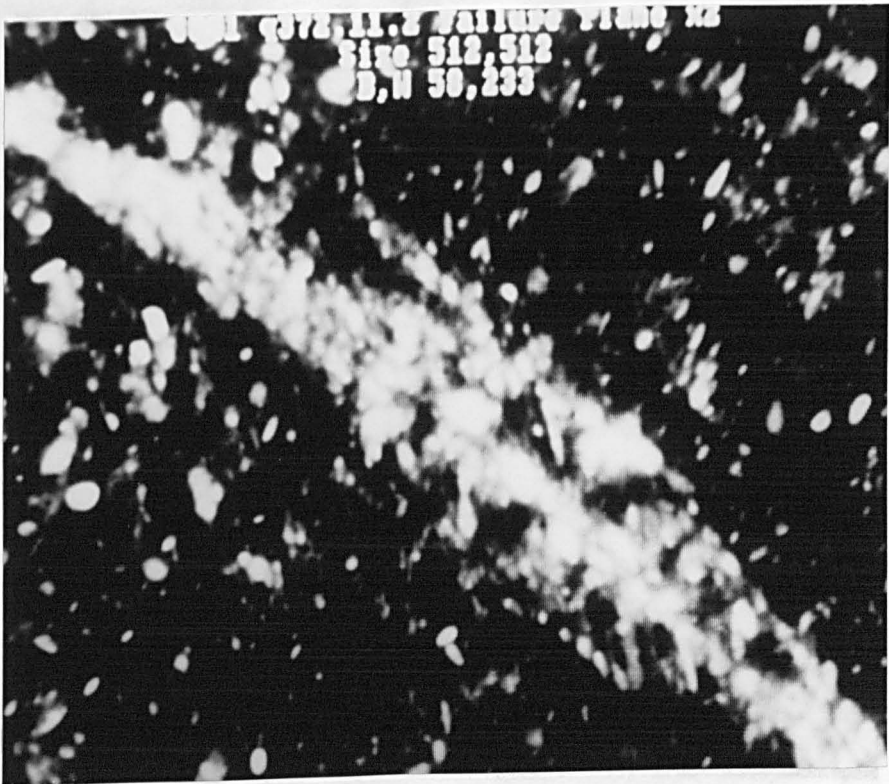
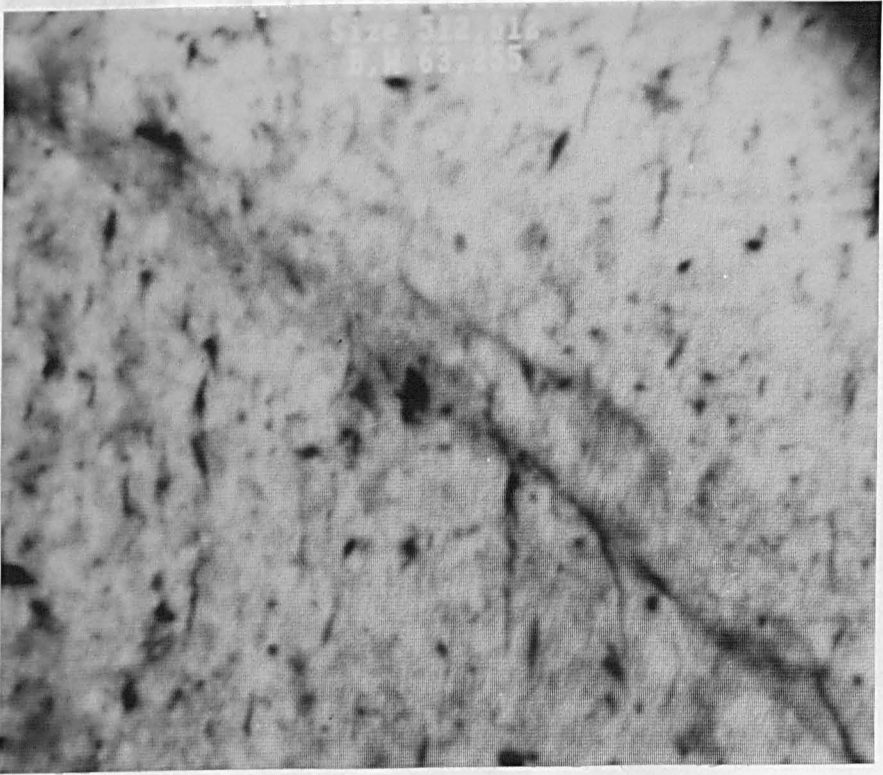
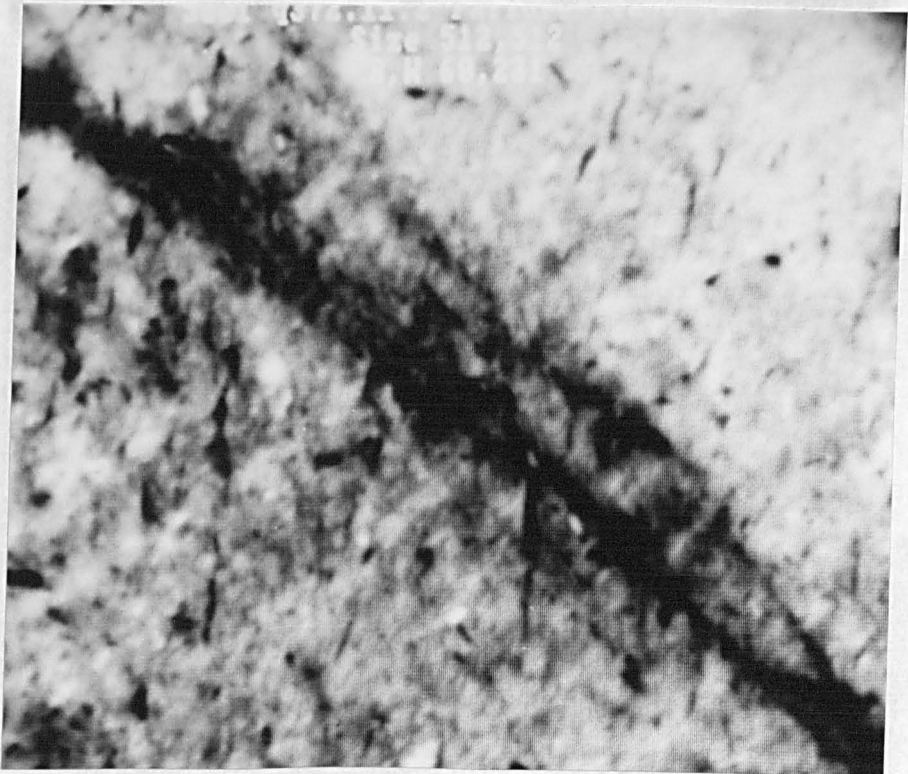


Fig.4.3.b Optical Micrograph of Polars Crossed on the Square, x2.



*Fig.4.3.c* Optical Micrograph of Polars Crossed on the Diagonal with Quarter Wave Plate, q1.



*Fig.4.3.d* As (c) but on the Square, q2.

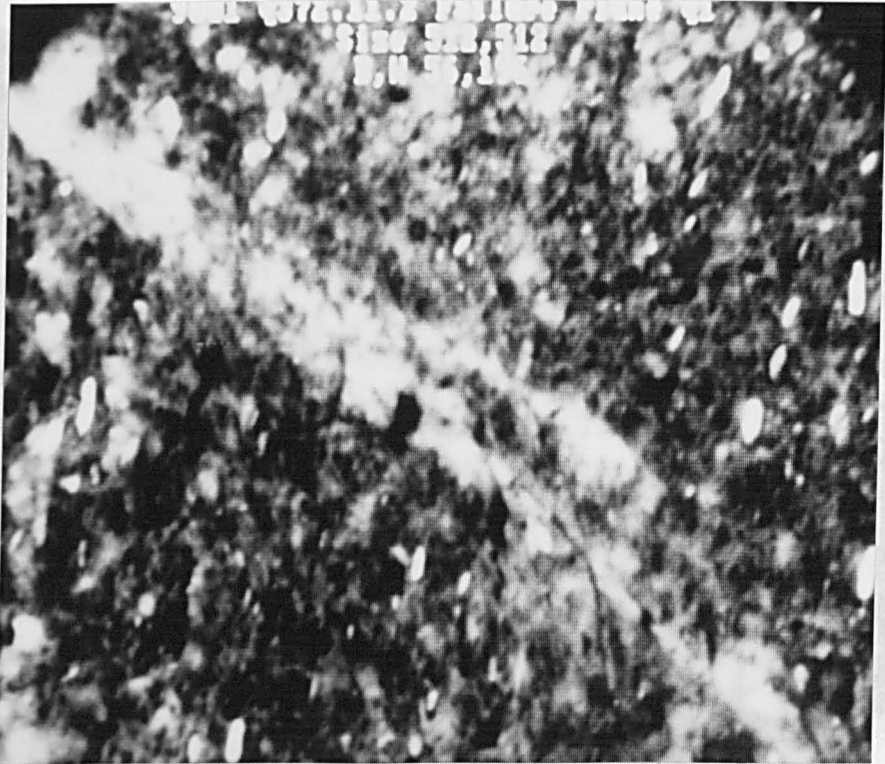


Fig.4.3.e As (c) but Synchroniser Turned  $90^{\circ}$ , q3.

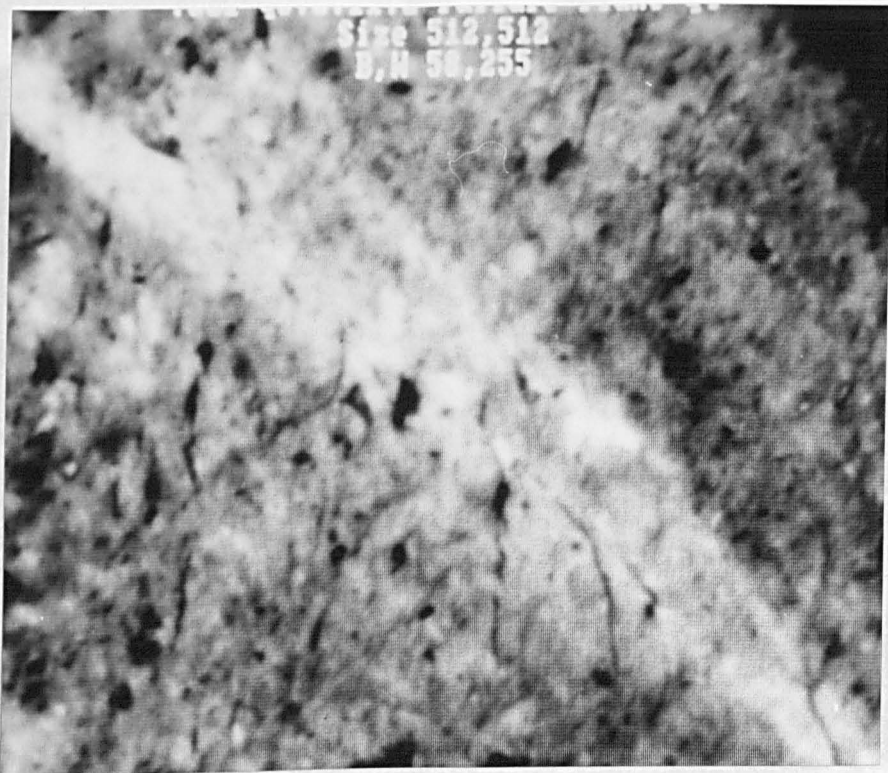
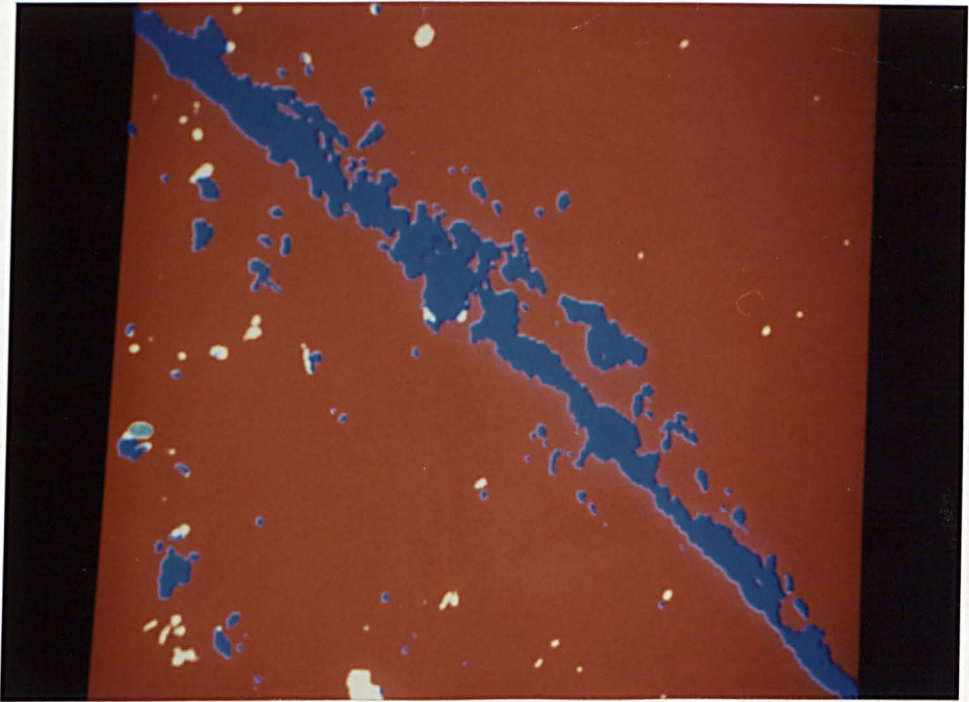
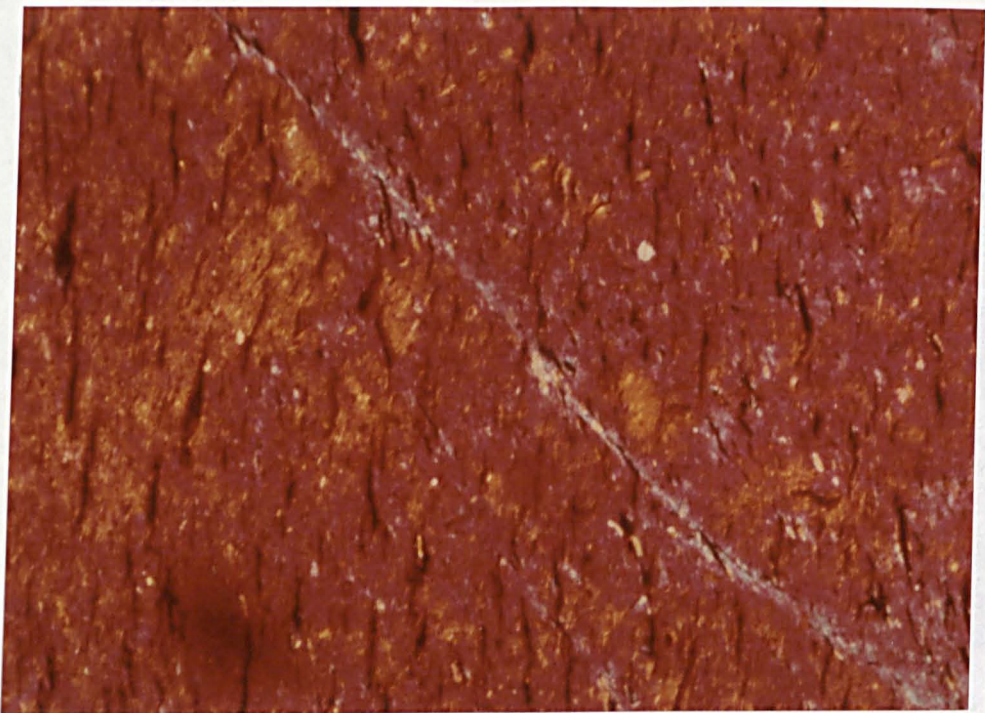


Fig.4.3.f As (d) but Synchroniser Turned  $90^{\circ}$ , q4.



*Fig.4.4* Field of Fig.4.3 Mapped Using POLMAP.



*Fig.4.5* Field of Fig.4.3 with Full-Wave Plate.

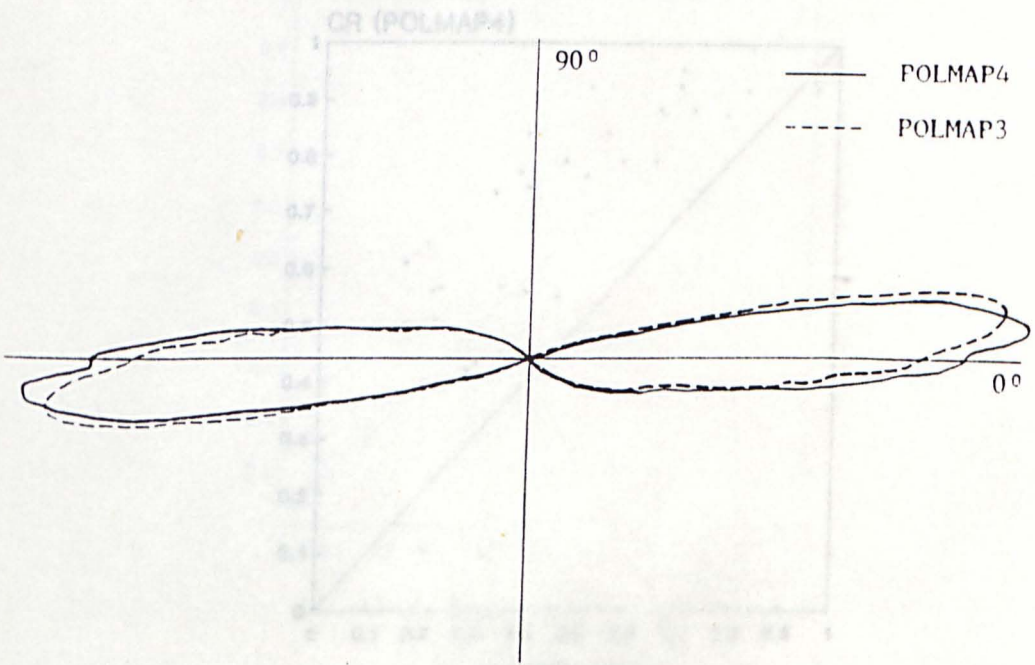


Fig.4.6 Polar Histograms for Fig.4.3.

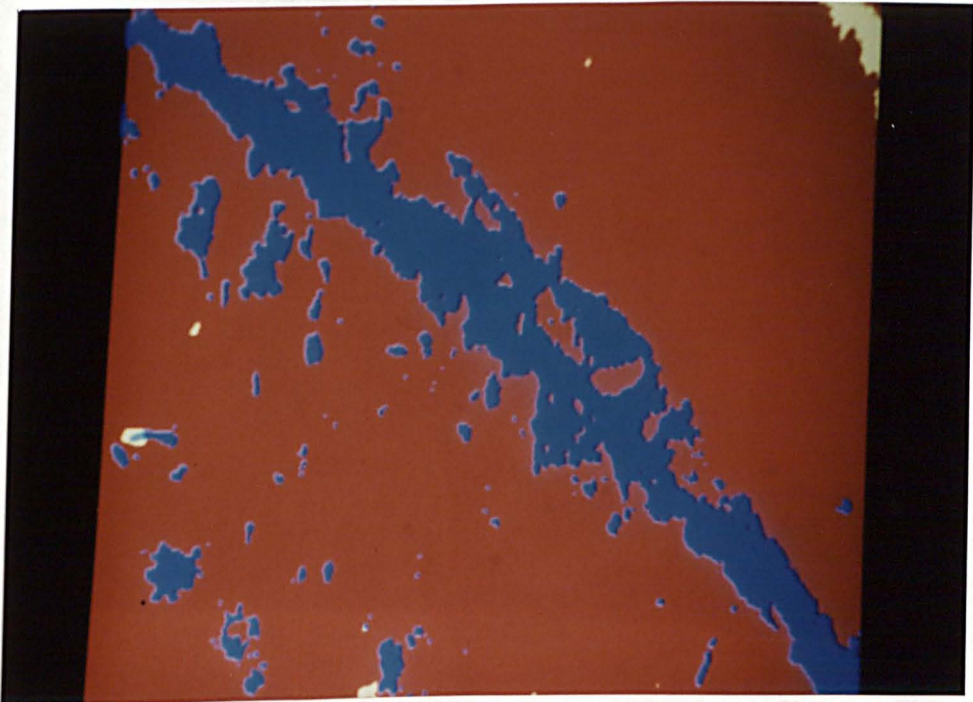


Fig.4.7 Field of Fig.4.3 Mapped by POLMAP4.

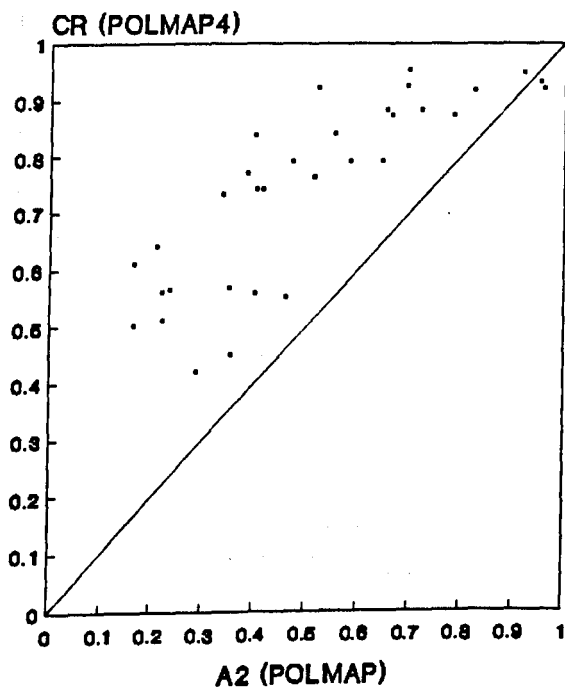


Fig.4.8.a Consistency Ratio, CR, vs. Anisotropy Index, A2  
for Normally Consolidated Undrained Shear.

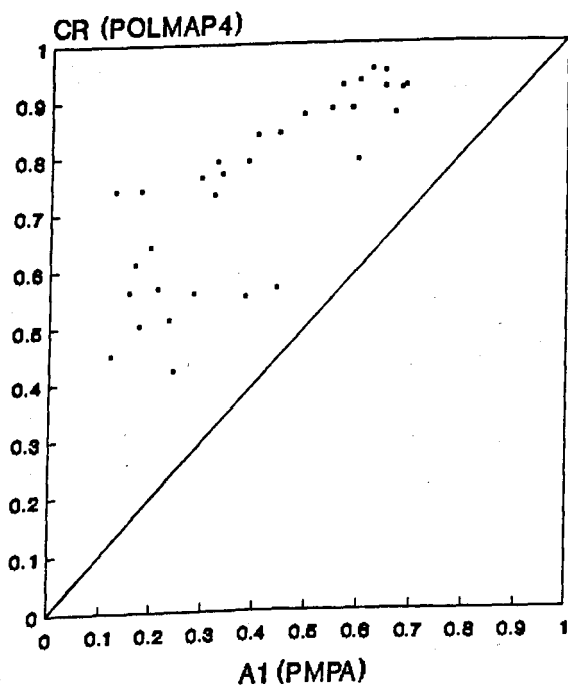


Fig.4.8.b Consistency Ratio, CR, vs. Anisotropy Index, A1  
for Normally Consolidated Undrained Shear

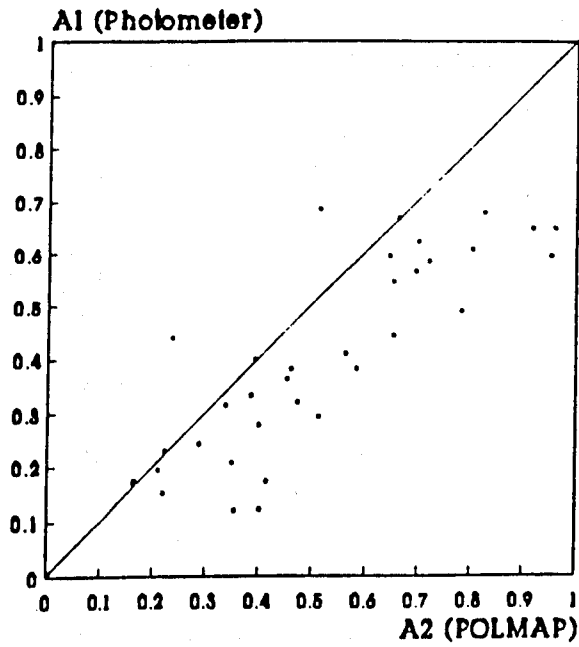


Fig.4.9.a Anisotropy Indices: A1 from Micro-Photometer vs. A2 From POLMAP, for Normally Consolidated Undrained Shear.

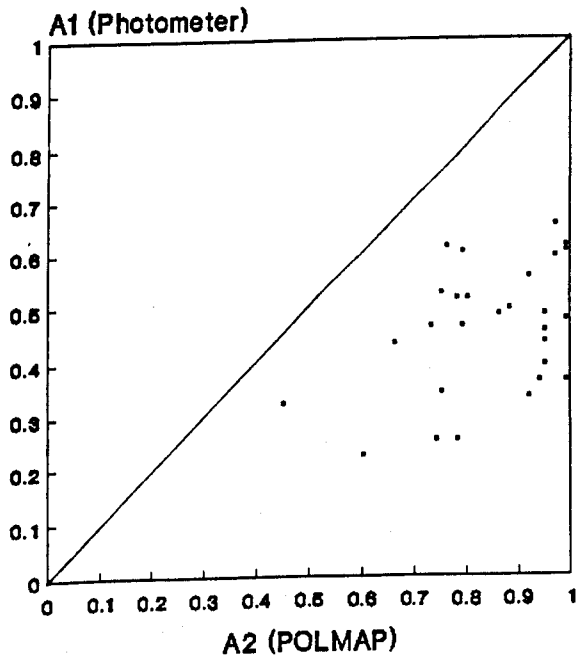


Fig.4.9.b As (a) but for Normally Consolidated Drained Shear.

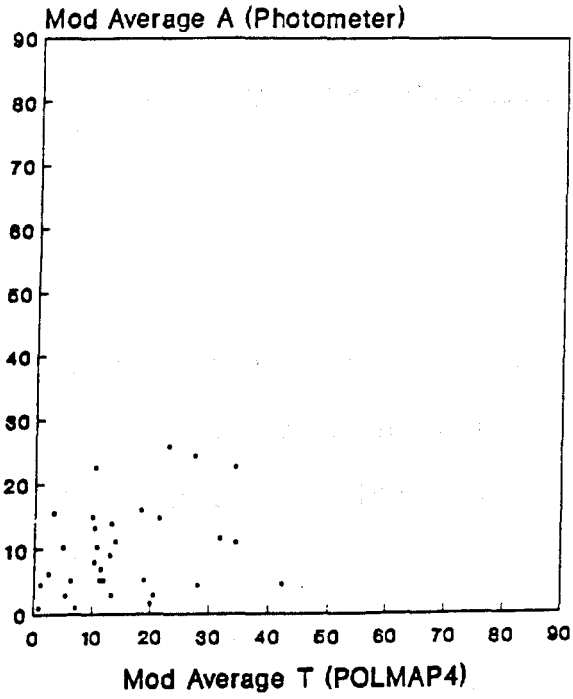


Fig.4.10 Mod average A vs. Mod average T  
Normally Consolidated Undrained Shear.

## Chapter 5

## SCANNING ELECTRON MICROSCOPY AND IMAGE ANALYSIS

5.1 Introduction

For many years, scanning electron microscopy has been used in the study of soil microstructure; and several workers have used such studies to complement optical microscopic and X-ray texture goniometric methods. This is because electron microscopy is the only technique which possesses sufficiently high resolution to permit the identification of particles as small as those of clay. Electron microscopes are of two sorts according to whether the electron beam is transmitted through the specimen or reflected by it. In this research, reflection scanning electron microscopy was used (Hayes, 1972).

For over 20 years, it had been necessary to use hand mapping to analyse the structure of clayey soils as seen by the electron microscope. Although much valuable information had been obtained by hand mapping, it was too slow and expensive for modern conditions, and almost all of the intra-feature information was inaccessible to it. In recent years, the development of image processors, analysers, and image processing software for use on PC and other computers is providing a most useful tool in the quantitative studies of soil microstructure.

This Chapter reports the methods of electron microscopy and of image analysis which were used to study the structure of the samples deformed in the triaxial tests in this research.

## 5.2 Scanning Electron Microscopy

### 5.2.1 Scanning Electron Microscope

The scanning electron microscope employs a reflection geometry for the formation of the image; its basic components are an electron gun and two or more electro-magnetic lenses.

The beam of electrons leaving the gun is reduced in diameter by the lenses to produce an image of the electron source on the surface of the specimen. At the point of impact of the beam of electrons on the specimen, some electrons are reflected as back-scattered electrons, while others liberate secondary electrons of low energy. In addition, collisions between some of the electrons and atoms in the specimen cause the emission of various wavelengths of electromagnetic radiation.

The electrons which are issued from the specimen by these means are collected, amplified, and used to control the brightness of a spot on the screen of a cathode ray tube. Before the electron beam passes through the final lens, a scanning raster is set up, which deflects the beam and causes it to scan over the surface of the specimen. The spot on the surface of the cathode ray tube is also caused to scan in synchronism. In this way, a picture is built up which has a direct correspondence with the surface of the specimen within the scanned area. The contrast of the picture depends on the variation in the reflectivity of the surface of the specimen; when the surface is not smooth, this reflectivity depends mainly on the topography of the surface of the specimen; but when the surface is flat, no topographic effect exists, and the contrast depends on variation of the chemical composition of the surface. The brightness of the spot depends on the

material, the angle of incidence of the beam, and the operating conditions of the instrument.

The magnification can be expressed as the ratio of the distance scanned on the cathode ray tube to that scanned by the electron beam on the surface of a specimen inclined normally to that beam. The magnification can be varied continuously over a wide range. The maximum useful magnification depends on the instrument's resolving power, which in turn depends on the diameter of the electron probe and the scattering of electrons within the specimen. Resolution is limited to approximately  $0.01 \mu\text{m}$ .

### 5.2.2 Scanning Electron Microscope Operating Conditions

As mentioned above, the effect of the factors which control the quality of the image from the Scanning Electron Microscope are various and complicated. In order to obtain a perfect image for analysis, some decisions must be made at an early stage. Tovey (1980), however, investigated the problem of the relative orientation of the object to the collector; he found no significant difference and showed that the intensity gradient technique could be used to assess orientation of a specimen to within 1 degree. Moreover, Tovey and Sokolov (1981) also have studied the effects of several of the instrumental parameters on the results; they showed that beam current variations in the Scanning Electron Microscope did not affect the results. However, there still remain some questions which are described as follows.

#### i. *Choice of Operating Mode*

There are two sorts of operating modes which may be chosen; these are the

back-scattered mode and the secondary mode. Some trials were made in the beginning. Sometimes secondary emission was better than back-scattered emission; the difference seems to vary from microscope to microscope. In this research, the back-scattered mode was chosen. The reason is that the back-scattered mode produced micrographs of higher contrast than did the secondary mode in the microscope used. This effect can often be used to great advantage to identify small particles, which are usually not readily apparent in the secondary mode. The back-scattered mode also seemed to reduce the noise in the images. In addition, the back-scattered mode was employed in the University of East Anglia. They have accumulated much relevant experience and provided much useful advice for the preparation of the specimen and the method of observation. The operating voltage was 20 kv.

## ii. *Choice of Magnification*

It is well known that the higher the magnification used, the smaller the area covered by each micrograph. Examination of the overall aspect at low magnification may provide some answers, but detailed examination at high magnification will be necessary to see many of the microtextural features which are characteristic of some environments.

Smart and Tovey (1982) have given a brief summary of some of the magnifications that have been found useful. They suggest that at magnifications between 2500x and 10000x, individual particles can be seen, and the inter-particle structure in a kaolin can be revealed as well.

According to the above suggestions and several trial examinations, a magnification of 4000x was used as a standard magnification in this research; this

brings as many features as possible into the field of view and reveals the small particles as well as possible. Most observations were made at this magnification.

When images were recorded photographically, the Scanning Electron Microscope in the Department of Geology at the University of Glasgow added a scale mark to the negatives, so that the magnification could be worked out whatever the enlargement was and when making prints.

When images were recorded electronically, in preparation for making quantitative measurements of size or orientation, separate calibrations of the instrument at the relevant magnifications were made, using the Scanning Electron Microscope calibration specimens supplied by Agar Scientific Ltd. The relevant data are listed in Table 5.1. Here, it is the size of the imaged areas which is important. These areas refer to the full-sized digital images discussed below. It is useful to refer to these images by their 'magnification', but this is a nominal figure which refers only to what was seen on the screen of the monitor. There is a difference of 6% in the scales in the two directions. If necessary, the measurements obtained from the images could be corrected for this effect.

Table 5.1

Magnification	Size of Imaged Area hz x vert
x4000	25.0 x 23.5 $\mu\text{m}$
x2000	49.1 x 46.1 $\mu\text{m}$
x800	124.0 x 115.7 $\mu\text{m}$
x400	250.0 x 235.0 $\mu\text{m}$

### iii. *Material of Coating*

Materials that do not naturally conduct electricity and heat cause problems in the scanning electron microscope unless they can be made conductive by some method. The main problem is known as 'charging'. If some parts of the image charge up, by retaining electrons, these parts appear extra bright in the image. The primary purpose of the coating material is to conduct charge and heat from the specimen to the stub. Therefore, certain characteristics are required for these thin films to perform effectively. The most common method is by vacuum deposition of a conducting coating.

Firstly, the conductive film must be continuous and uniform over the entire specimen surface. The film must also be continuous with the stub which usually is made of metal such as copper or aluminium. To minimise the conducting path, the specimen is stuck to the stub using a conducting glue, Quick Dry Silver Paint supplied by Agar Scientific Ltd. The ability of a conductive material to form a smooth and continuous film is of importance. Thus, it provides a good path to conduct heat away and electricity to earth. Secondly, the coating material will not readily react with the specimen surface or oxidize over a long period of time. Further, it must be able to withstand subjection to the electron beam without deterioration and subsequent loss of continuity. In addition, for microscopy proper, the efficiency of reflection of electrons,  $\eta$ , should be high.

Gold coating was used first in this research, but it did not provide a perfect image; then, following the procedure at the University of East Anglia, carbon coating was substituted for gold, and better images were obtained. Therefore, all of specimens used in this thesis were coated with carbon.

#### iv. Observation

All of the scanning electron microscopy was done using a Cambridge Instrument Company Scanning Electron Microscope, Model 5526, running in the Department of Geology. This instrument was very easy to use, because it was controlled by a computer. Digitized images were recorded by another computer which is an integral part of the Cambridge Scanning Electron Microscope. The micrographs show cross-sections of the resin-impregnated specimens (the specimen preparation was described in Section 3.3); the particles are light grey, the resin in the voids is dark grey.

All the digitized micrographs from the electron microscope have 512 rows of 512 pixels each and are digitized to 256 grey levels, the same as those from the optical microscope. Usually, 26 images were taken from a bulk specimen of about 20 x 20 mm, including 25 images at 4000x magnification and one at 800x magnification. The images at high magnification are arranged in an array of five rows of five images each (Fig.5.1). The distance between adjacent images was about 2.5 mm. The images at both sides of the bulk begin at about 5 mm from the specimen edges to avoid the edge disturbances. The low magnification image was taken concentrically with the central high magnification images.

### 5.3 Image Analysis

#### 5.3.1 Introduction

Image processing and image analysis techniques have only recently become an important tool in the quantification of soil microstructure (Tovey 1980, Tovey and Sokolov 1981, Smart and Tovey 1982, Tovey and Smart 1986, Chiou *et al.* 1990,

Bhatia and Soliman 1990, Smart and Leng, 1992), even though they have been used for some time in many areas of science such as biology and geology.

There are four steps to any quantitative analysis using image processing and analysis, which are listed as follows:

1. Image digitization and coding: the image to be studied must be digitized into a discrete array of pixels before it is analysed. At each pixel, the intensity is coded on a grey level scale (frequently 0 - 255, but sometimes 0 - 65535). A typical image will be stored as a 512 x 512 array of pixel values, but any suitable size may be used, depending on the hardware which is available. The modern trend is towards larger arrays; but these were not available here.

2. Image enhancement and restoration: the digitized image may be enhanced, which involves image de-blurring, contrast stretching, or equalization, binary or multiple thresholding, or image rotation.

3. Image analysis: this is the image analysis itself, in which the features discovered in the image are quantified by some algorithm measuring the properties of the image, which may be classified or described in terms of its parts and properties.

4. Interpretation of results.

At present, for the study of soil microstructure, the main interest is concentrated on the orientation analysis of electron micrographs of soil, because the orientation of the soil particles reflects the geological and geochemical conditions of the soil, the qualitative classifications of the soil, the relationship of

the changes of soil microstructure to external physical effects such as mechanical deformation, and the mode of flow of water through the soil. For the study of the orientation of electron micrographs, the intensity gradient method was first introduced by Unitt (1975), who analysed the anisotropy of microstructure on a point by point basis. Later, much useful improvement was made (Unitt and Smith 1976, Tovey 1980, Smart and Tovey 1988). Based on these methods, Smart and Leng first automated the hand mapping methods (Smart and Leng 1992). Leng then made further improvements which will be explained below. Her programs were employed in the main analysis of electron micrographs of this thesis.

A brief review are given in the following Sections.

### 5.3.2 Intensity Gradient - PICDIF

Unitt (1975) introduced the intensity gradient method to the orientation analysis of electron micrographs. This method is fundamental in that the edges of any feature in a digitized micrograph are differentiated from the surrounding region by changes in two directions along and across the scan lines. These changes can be used to determine the orientation of a feature, as its alignment will be orthogonal to the direction in which the rate of change of intensity is greatest. Unitt calculated a vector indicating the greatest rate of change of intensity gradient at each pixel in the image. For example, the vector  $U$  at point 0 was calculated from the four closest neighbour pixels (Fig.5.2):

$$X = 0.5 (I_1 - I_3) \quad (5.1);$$

$$Y = 0.5 (I_2 - I_4) \quad (5.2);$$

$$U = (X^2 + Y^2)^{1/2} \quad (5.3);$$

$$\alpha = \text{arc tan } (Y/X) \quad (5.4);$$

where

$U$  = the magnitude of the intensity gradient vector  $U$ ;

$\alpha$  = the direction of the intensity gradient vector  $U$ ;

$X$  = the intensity gradient at point 0 in the x-direction;

$Y$  = the intensity gradient at point 0 in the y-direction;

$I_i$  = the intensity of the pixel at point  $i$ .

Unitt and Smith (1976) realized that the method was affected by the limited range of values that the intensity at any one point may take. When variations in intensity are small, the difference functions in both the numerator and denominator are also small, and thus only a few values of  $\alpha$  are possible. In order to overcome this, Unitt extended the analysis to include points 1 - 4 and 9 - 12 (Fig.5.2) in what later became known as the 9c-point analysis. Tovey (1980) showed that problems still arose with regions where the intensity varied little, and suggested that vectors with a magnitude less than  $2/h$  should be omitted in the aggregation of results to form a rosette diagram. In an attempt to improve the accuracy, Tovey and Smart (1986) considered two other groupings of points namely points 1 - 8 (Fig.5.2) inclusive (known as the 9s-point method), and an arrangement with points 1 - 12 and 21 - 24 (Fig.5.2) inclusive (known as the 17-point method). They found that the increased number of points used in the analysis improved the general shape of the rosette diagram. The 9c-point and 17-point methods were to be preferred. Later Smart and Tovey (1988) worked out all of the formulae for calculating the coefficients for different sizes of masks within the 24 points shown in Fig.5.2 based on the two dimensional Taylor expansion. It is found that the '20' mask (Fig.5.2 at 1,2,.....,20) is the most nearly circular, and the '20,14-formula' is the most accurate. This formula was derived by a least squares solution for the first 14 differential coefficients in the Taylor series based on a square grid. The coefficient matrices for the

x-direction,  $dx$ , and the y-direction,  $dy$ , for this formula, are given as follows respectively:

$$\begin{bmatrix} 0 & 0.013 & 0 & -0.013 & 0 \\ 0.077 & -0.207 & 0 & 0.207 & -0.077 \\ -0.070 & -0.280 & 0 & 0.280 & 0.070 \\ 0.077 & -0.207 & 0 & 0.207 & -0.077 \\ 0 & 0.013 & 0 & -0.013 & 0 \end{bmatrix}$$

$$\begin{bmatrix} 0 & 0.077 & -0.070 & 0.077 & 0 \\ 0.013 & -0.207 & -0.280 & -0.207 & 0.013 \\ 0 & 0 & 0 & 0 & 0 \\ -0.013 & 0.207 & 0.280 & 0.207 & -0.013 \\ 0 & -0.077 & 0.070 & -0.077 & 0 \end{bmatrix}$$

For the method to be used in this research, the '20,14-formula' was employed. The magnitude and the angle of the intensity gradient vector can be worked out from following equations:

$$U = (dx^2 + dy^2)^{1/2} \quad (5.5),$$

$$\alpha = \text{arc tan } (dy / dx) \quad (5.6).$$

As mentioned above,  $\alpha$  is determined from Eqn.5.6; if  $U$  is zero,  $\alpha$  is undetermined; so pixels must be labelled 'undecided' when  $U$  is smaller than an arbitrary limit, which was taken as 3 pixels in the present work, where for convenience, the term 'pixel' is used as a measure of length. This is slightly more severe than Tovey's recommendation of  $2/h$  mentioned above.

### 5.3.3 Consistency Ratio Mapping - PICCON

The clay structure consisted mainly of groups of particles showing strong local preferred orientation which are called domains here. There were also some random clusters of plates. Consistency Ratio Mapping was developed to map

these features (Smart and Leng 1991).

Filtering techniques are widely employed in image restoration. As the intensity gradient image is a vector image, the operation has to be based on directional statistics theory. The mean direction of the observed intensity gradient vectors, therefore, were introduced here. The filter used here is a large circular filter. The radius of the filter is necessarily large enough to contain the large particles. The higher the magnification of micrograph to be analysed, the larger the size of the domain in the micrograph is, the larger the radius of the filter should be. The radius of the filter was determined based on the statistical method and an analysis of the graph of the semi-variance (Smart *et al.* 1992). A radius of 20 pixels was used.

The Consistency Ratio method maps domains and random clusters by first smoothing the vector field,  $U$ , then testing for randomness and segmenting the oriented areas into a limited number of equally spaced directions. The formulae are:

$$X = \sum U \cos 2A \quad (5.7),$$

$$Y = \sum U \sin 2A \quad (5.8),$$

$$S = \sum U \quad (5.9),$$

$$R = (X^2 + Y^2)^{1/2} \quad (5.10),$$

$$C = R/S \quad (5.11),$$

$$\tau = 0.5 \text{ arc tan } (Y/X) \quad (5.12).$$

where

$$A = \arg \text{ grad } I;$$

$$U = \text{mod grad } I.$$

For the clay structure analysis, the angles of vectors are doubled before computation, and then halved afterwards, because the intensity gradient vectors surrounding each particle all point outwards, and they are in opposite directions for two parallel edges; so the opposite vectors would cancel each other out.

Mapping is achieved by segmenting T. The process is:

1. Calculate the intensity gradient at each pixel in the image;
2. Sum the vectors within the large circular filter;
3. Encode the angles of summed vectors to get the local preferred orientation;
4. Map the pixels with the same preferred orientation into domains.

Two special cases should be considered. First, if S is small, T must be labelled 'undecided' and mapped accordingly. Second, if

$$C < \{1/N \ln (1/P)\}^{1/2} \quad (5.13),$$

where N is the number of (decided) pixels in the filter, and P is the probability of obtaining a greater consistency ratio by chance, the pixel is mapped as random (Smart and Leng 1990).

T is coded into a limited number of directions, say 4, 8, or 12. In this thesis, four directions were chosen for comparing with the results of optical microscopy, which gives:

Code	Direction	
0	Undecided;	
1	Horizontal	$0 - \pi/8, 7\pi/8 - \pi;$
2	Down-left	$\pi/8 - 3\pi/8;$
3	Vertical	$3\pi/8 - 5\pi/8;$
4	Down-right	$5\pi/8 - 7\pi/8;$
5	Random.	

### 5.3.4 Orientation Enhancement

Intensity gradient analysis had originally been developed in soil microstructural analysis to measure the anisotropy of samples as seen in scanning electron microscopes by obtaining the polar histogram of angle  $A$ . Fig.5.3 shows an original image. As shown in Figs.5.4.a and b, the histogram of  $A$  has an 'elliptical' shape whether weighted by  $U$  or not. The consistency ratio mapping was therefore modified to give an enhanced orientation analysis by providing histograms instead of maps (Leng in preparation).

For the same reason as mentioned in Section 5.3.2, the mean direction vectors were calculated by the following equations:

$$\bar{X} = n^{-1} \sum U_i \cos (2\alpha_i) \quad (5.14),$$

$$\bar{Y} = n^{-1} \sum U_i \sin (2\alpha_i) \quad (5.15),$$

$$\bar{R} = (\bar{X}^2 + \bar{Y}^2)^{1/2} \quad (5.16),$$

$$\bar{\theta} = 0.5 \text{ arc tan } \bar{Y}/\bar{X} \quad (5.17),$$

where

$\bar{X}$ : components of mean direction vectors of the filter in x-direction;

$\bar{Y}$ : components of mean direction vectors of the filter in y-direction;

$\alpha_i, U_i$ : angle and strength of intensity gradient at each pixel within the filter;

$\bar{\theta}, \bar{R}$ : angle and strength of the mean direction vectors of the filter.

The resultant mean direction vectors formed a third image: mean direction

vector image. As shown in Figs.5.4.c and d, the histograms of the smoothed angle,  $\bar{\theta}$ , show stronger and more obvious distribution than did Figs.5.4.a and b, the details depending on whether weighted by  $\bar{R}$  or not.

### 5.3.5 Porosity Analysis — PICPOR

#### i. Introduction

The back-scattered images from the scanning electron microscope appear to be ideally suited to extracting the porosity information by simple thresholding. Thresholding is one of the most important approaches to image segmentation. The fundamental idea is that, if the given image  $f$  has grey level range  $[Z_1, Z_k]$ , and  $T_h$  is any number between  $Z_1$  and  $Z_k$ , the result of thresholding  $f$  at  $T_h$  is the two-valued image  $f_t$  defined by

$$f_t(x,y) = \begin{cases} 1 & \text{if } f(x,y) \geq T_h \\ 0 & \text{if } f(x,y) < T_h \end{cases} \quad (5.18).$$

This gives a black-and-white image (binary image).

In an ideal situation, the image would consist of only two components: the kaolin particles and the impregnated voids. In the simple case, the grey level histogram would show two peaks, one corresponding to the mean intensity of the particles, the other to the mean intensity of the voids. For such a case, it would be very simple to select the mid point between the peaks to represent the correct threshold. In the situation here, however, such an idealized image is not realized, and the grey level histograms from all of the images are unimodal, so there is no clear separation of the grey levels into two groups as described above.

The degradation of images is a common feature in all types of microscope, and this results in an ideal image becoming blurred through averaging around each pixel. It is difficult to choose a simple global threshold which will segment the particles from the voids correctly. To deal with this problem, two methods were developed, which are described in turn below.

## ii. *Black-and-White Method*

In the situation which arose here, it is difficult to fix the threshold to produce an accurate black-and-white image. In present work, Hounslow and Tovey (1992) developed a method to choose this automatically by comparing each pair of adjacent pixels whilst scanning the image from top to bottom and thus generating a relative contrast histogram  $c(t)$ . During the scan, each pair of adjacent pixels was considered. If the grey levels of such pair of pixels are  $I_a$  and  $I_b$  (where  $I_b > I_a$ ), and the search threshold level is  $T$ , where  $I_a \leq T_h < I_b$ , a contribution given by

$$dc(T_h) = \min (T_h - I_a, I_b - T_h)$$

was added to the relative contrast histogram. The peak of the relative contrast histogram based on all adjacent pairs in the whole image was accepted as the threshold; pixels brighter than the threshold were mapped as particles; other pixels were mapped as voids. As a preliminary, they had used Wiener filtering to sharpen the contrast of the image. However, this method had not been implemented in Glasgow, so a simpler approach had to be used.

A simple method to provide a black-and-white image was based on simple thresholding. As mentioned above, all pixels with grey levels below a threshold value are labelled as voids; and the others as solids. The threshold was chosen automatically to give the correct porosity for the sample using the histogram of

grey levels for the whole series. The reasonableness of the choice of threshold was checked by superimposing alternate tiles of the black-and-white images on the original grey images, see Fig.5.5.

### iii. Grey Level Method

The grey level method of measuring the local porosity is based on the original grey images. It assumes that the porosity of a single pixel is proportional to its grey level. By analogy with X-ray micro-analysis, the local porosity,  $p$ , of an individual pixel is given approximately by:

$$p = (I_s - I)/(I_s - I_v) \quad (5.19),$$

where  $I_s$ : grey level corresponding to pure solids,

$I_v$ : grey level corresponding to pure voids.

It has been intended to standardise  $I_v$  and  $I_s$  by adjusting the microscope on a block of pure resin and on a large solid particle, respectively, following the procedure established in the University of East Anglia. However, due to difference between the microscopes used, this was not possible here. Therefore, values of  $I_s$  and  $I_v$  had to be chosen using the histogram of intensities of grey levels for all 25 images from one specimen. The pairs of values were chosen to keep the porosities calculated from image analysis for each sample equal to those obtained by gravimetric analysis (within a few parts per thousand).

## 5.4 Flow chart

According to the above discussion, the following procedure for image analysis of the scanning electron micrograph was used in this research:

*i. Image Archive*

As mentioned in Section 5.2.2, electron micrographs were digitised as they were recorded by the Cambridge 360 SEM; then they were stored temporarily on a hard disk. At the end of a session, the micrographs were copied to a half-inch magnetic tape which forms a primary archive. About 5% of the images for each session were also copied on to floppy disks for the Nimbus analyser. The images stored on the tape were then copied to the Meiko main tape via Sun workstations.

About 5% of the images on the Meiko either had missing scan lines or were incomplete. These were located in a preliminary inspection, and the poor quality images were moved to the ends of the batches containing them and excluded from further analysis. By the end of this stage, all the good images for each sample were in one contiguous block of files ready for analysis.

*ii. Preliminary Analysis of Grey Levels*

A preliminary analysis of all the good images for each specimen was made as follows, see Fig.5.6.

*1. Histogram of Greys*

The histogram of the grey levels at each pixel was calculated for the whole set of images.

## 2. Choose Threshold $T_h$

Based on the histogram as mentioned above and the porosity calculated from gravimetric analysis, a threshold for the specimen was chosen automatically (Section 5.3.).

## 3. Choose $I_s$ and $I_v$

Based on the same histogram, the values of  $I_s$  and  $I_v$  were chosen interactively to make the porosity calculated from the images equal to the true porosity as closely as possible (Section 5.3).

## 4. Calculate Results

The porosities were calculated using both methods, *i.e.* grey level and black-and-white, for all the good images for one specimen. This involved recording the images from file. Whilst the analysis was proceeding, the thresholded images were shown on the monitor as shown in Fig.5.5 as a check on the analysis.

## 5. Summarise Results

The results for each image were written to file together with their average and standard deviations.

### iii. Main Analysis

Fig.5.7 is a simplified flow chart showing the main analysis of the electron

micrograph. The work was actually split in parallel between 6 transputers, see Smart and Leng (1990). As in the preliminary analysis, all the good images for each specimen were analysed in one run. An example output file is in Appendix D.

### 1. Intensity Gradient

The intensity gradient was calculated at each pixel by means of the 20,14- formula for each good image proceeding one-by-one. The results were stored in a histogram, and the consistency ratio (magnitude and direction) was calculated for each image.

### 2. Consistency Ratio Smoothing

At each pixel, the intensity gradient vector was replaced by a consistency ratio vector calculated within a large circular filter centered on the pixel in order to smooth the field. The vectors  $U$  were summed in the filter; the mean vector and consistency ratio of the filter were calculated; then, the angles were encoded into four "directions" to map domains and random areas; chord sizes were measured from this map. The results were stored in histograms, and a new consistency ratio (magnitude and direction) was calculated for each image.

### 3. Porosity Analysis

The porosity at each pixel by means of the grey level method was calculated and smoothed using the same filter as above. The intensity gradient analysis (step i) was repeated for the smoothed porosity. In addition, this field was segmented into two classes at the true porosity of the specimen, and the chord

sizes analysis (step ii) was repeated. These results were stored in histograms.

#### 4. Summarise Results

The magnitudes and directions of the consistency ratios calculated from the intensity gradient, the consistency ratio smoothing and the porosity analysis were tabulated for all the images for one specimen. The chord sizes for all the images for both the consistency ratio map and the porosity map were also tabulated. Vector means, arithmetic means, and arithmetic standard deviations were calculated as appropriate. These results and selected histograms were then written to file, whilst the analysis was proceeding. The following images for each specimen in turn were shown on the monitor: original, intensity gradient, consistency ratio map, porosity map, original with consistency ratio boundaries superimposed.

Chapter seven contains the relevant discussion and analysis of the results obtained.

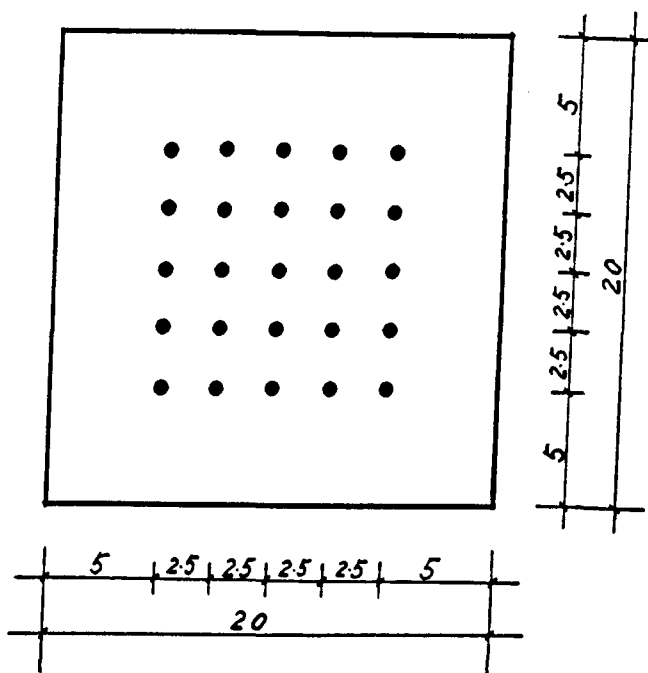


Fig.5.1 Indication of Images Taken.

			⋮			
	22	15	10	14	21	
	16	6	2	5	13	
...	11	3	0	1	9	...
	17	7	4	8	20	
	23	18	12	19	24	
			⋮			

Fig.5.2 Numbering of Pixels within the Mask.

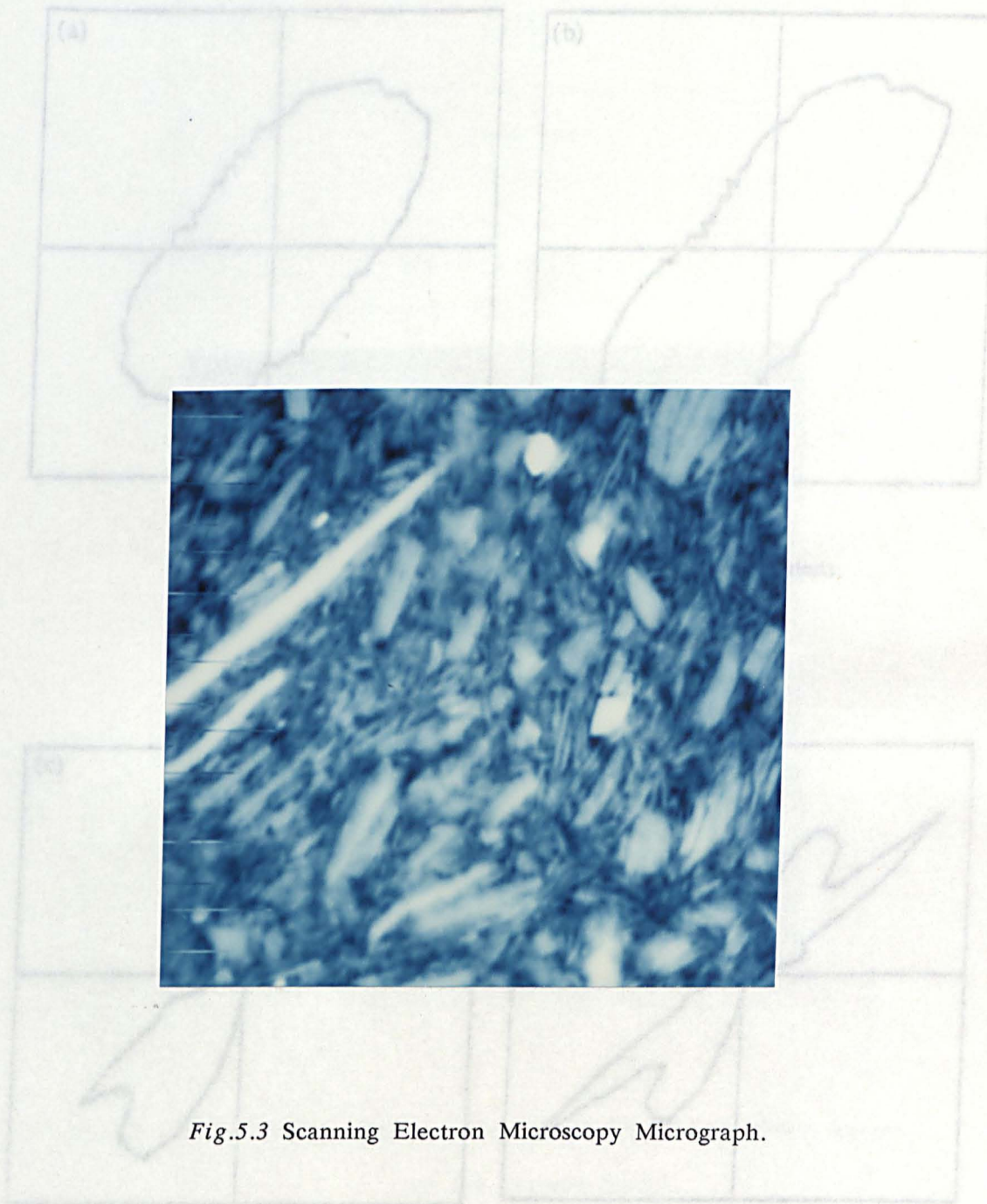
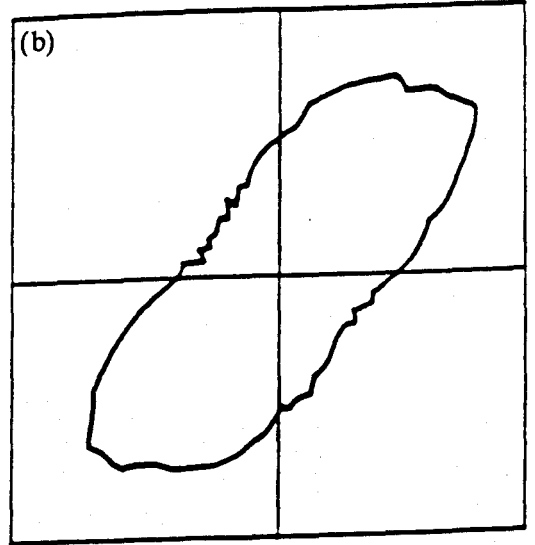
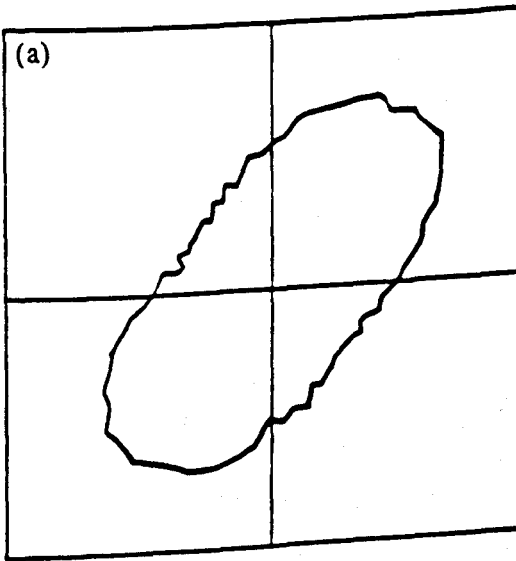


Fig.5.3 Scanning Electron Microscopy Micrograph.

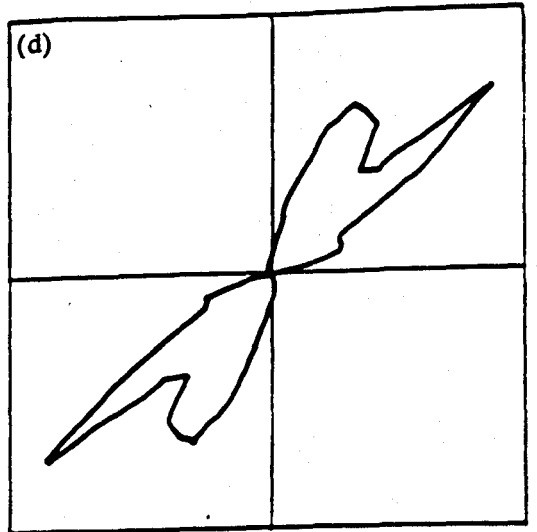
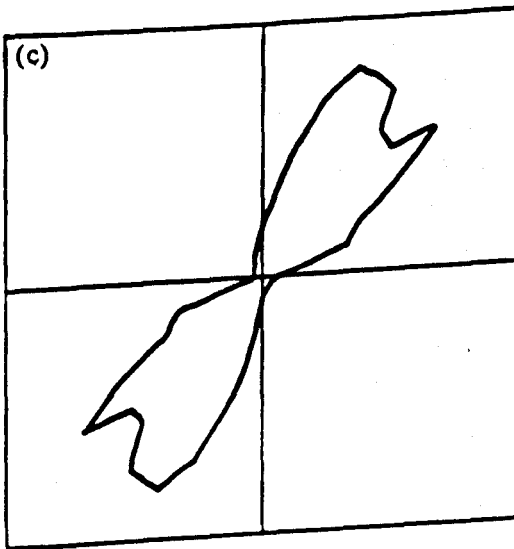
(c) Unweighted Histogram of Mean Distance;

(d) Weighted Version of (c).

Fig.5.4 Polar Histograms (calculation by Long, 1992).



(a) Unweighted Histogram of Angle of Intensity Gradient;  
(b) Weighted Version of (a).



(c) Unweighted Histogram of Mean Direction;  
(d) Weighted Version of (c).

Fig.5.4 Polar Histograms (calculation by Leng, 1992).

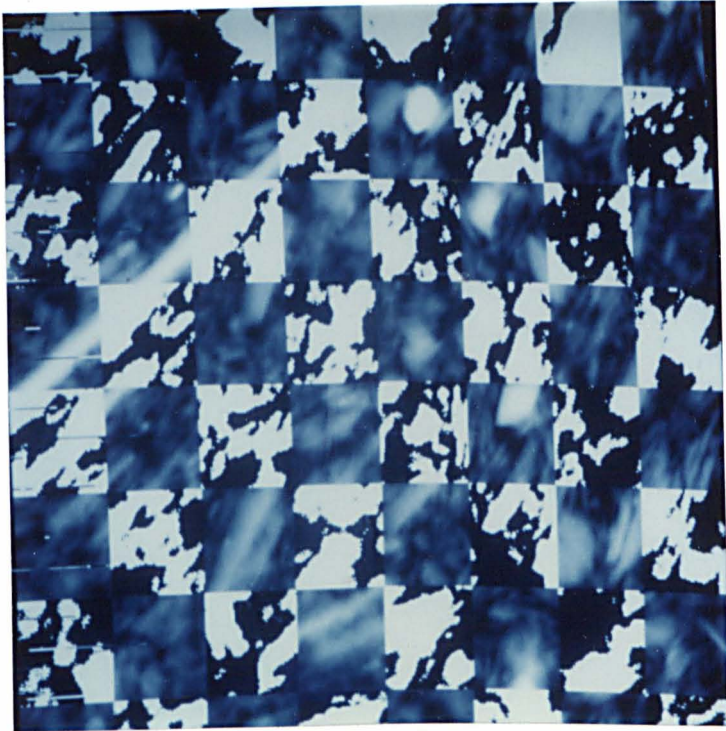


*Fig.5.5* Superimposing Alternate Tiles of the Black- and- White Images on the Original Images.

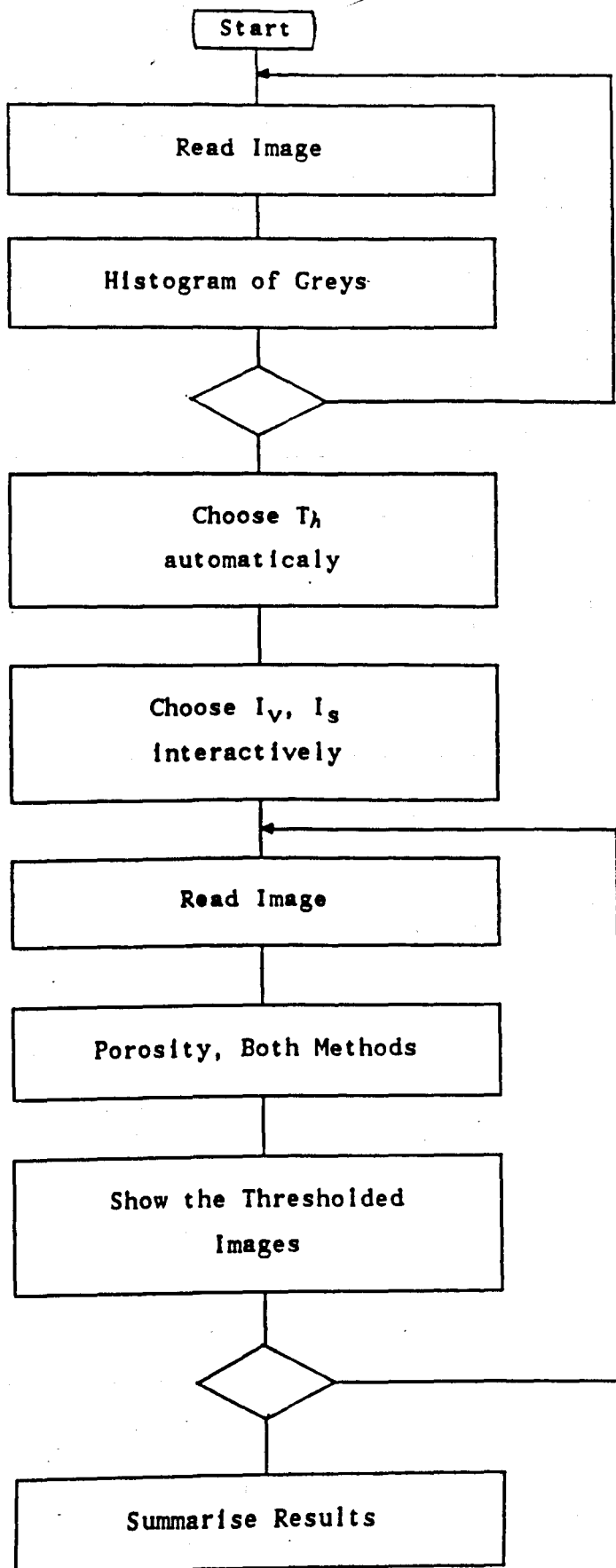


Fig.5.6 Flow Chart of Preliminary Analysis of Grey Levels.

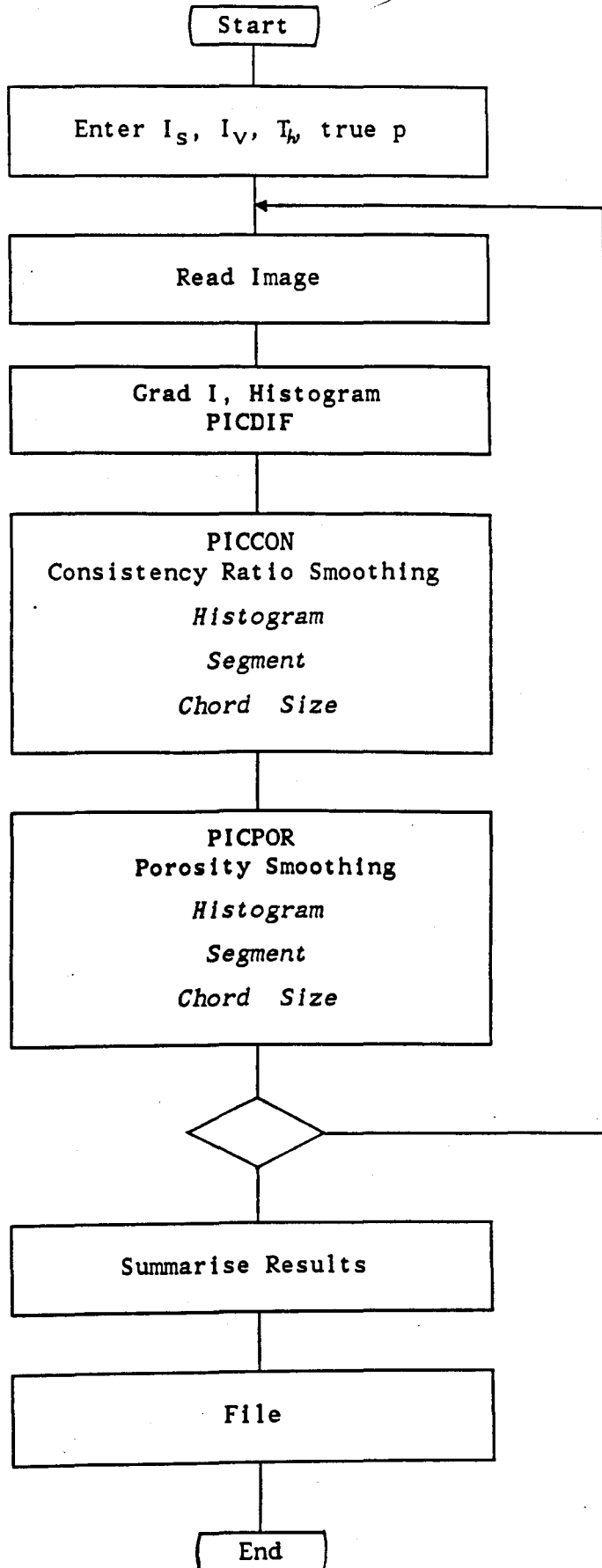


Fig.5.7 Flow Chart for Main Analysis.

## Chapter Six

## OBSERVATION AND DISCUSSION OF THIN SECTIONS

6.1 Introduction

The normally consolidated undrained triaxial testing employed in this research was discussed in Chapter Two; the observations carried out under the optical microscope will be discussed here; and the observations carried out under the scanning electron microscope will be discussed in the next Chapter. For comparison, the normally consolidated drained triaxial testing and the over-consolidated drained triaxial testing done by the University of East Anglia were observed and measured in the optical microscope and will also be discussed in this Chapter. As the optical observations are indirect, in that they do not allow the investigation of individual kaolin particles, the discussion will be limited to the description and analysis of the aggregates of particles and of the small groups of particles for the whole field observed. For convenience, the term patches will refer to areas which have local preferred orientation.

For the optical microscopy analysis, there are in total three methods used in this thesis, namely PMPA, POLMAP, and POLMAP4 (see Chapter 4). For the photometer method, PMPA, five fields were measured in each thin section; these were located in top-left, top-right, centre, bottom-left, and bottom-right of the thin section, respectively, and the results are given as the average of the five values (Fig.6.1). For the image analysis methods, POLMAP and POLMAP4, only four fields, *i.e.* top, left, right, and bottom,

which were different fields from the above measuring method, were measured for each thin section, the average results being analyzed (Fig.6.2).

For visual examination, the objective was x10, the tube factor x1.25, and the eyepiece x10, giving a magnification of x125. For the measurements, the eyepiece was removed, giving a circular field 1.5 mm diameter for the photometer, PMPA, and a field 0.47 mm square for the image analysis, POLMAP and POLMAP4, as discussed in Chapter 4.

## 6.2 Preliminary Observation on Failure Planes

### 6.2.1 Introduction

Before discussing the main results, some measurements taken across failure planes will be presented. In these cases, the measuring points formed a traverse across the failure plane.

### 6.2.2 Normally Consolidated Undrained Triaxial Testing

Fig.4.5 shows a typical failure plane for normally consolidated undrained triaxial testing sample at 14.5% strain. Fig.6.3 shows the results of POLMAP4. Each point refers to one field 0.47 mm square. It was found that both preferred orientation and the Consistency Ratio varied with the distance from the failure plane. The preferred orientation was changed from horizontal at the field far away from the failure plane to an inclined direction (in this particular case, the angle was  $27^{\circ}$  from horizontal) at the field involved failure plane. The Consistency Ratio decreased from 0.97 at 2 mm away from the field involved the failure plane to 0.908 at that field. In this

example, the image analysis seems to have shown some small changes which were not evident from visual examination at 1 mm from the failure plane.

### 6.2.3 Normally Consolidated Drained Triaxial Testing

Similar measurements to those discussed above were made for a normally consolidated drained triaxial testing sample and are shown in Fig.6.4 with similar results. These indicated that in the failure zone, particles inclined in the direction parallel to the failure direction, for example, at about  $17^\circ$  down-right to horizontal direction. Visual examination showed that the rotation at the boundary of the failure zone was sudden. The chord size did not give any obvious change.

### 6.2.4 Discussions

Visual examination showed that the particles in the failure plane were approximately parallel to the plane at about  $56^\circ$  inclination. However, the failure planes were less than 0.47 mm wide; so the measurements above included particles outside the failure planes.

## 6.3 Normally Consolidated Undrained Triaxial Testing

### 6.3.1 General Observation

The procedure of normally consolidated undrained triaxial testing was explained in Chapter Two. In total, 40 tests were made successfully, and stopped at different axial strains. Except for 5 samples which failed during impregnation, 35 thin sections were made from 35 triaxial samples, *i.e.* 315

fields, and another 5 thin sections (45 fields) were made from filter press cakes these being referred to as pre-consolidation. They were measured by PMPA, POLMAP, and POLMAP4, the details being listed in Table 6.1.

Table 6.1

Strain (%)	Number of Thin Sections
Pre-consolidation	5
0.0	6
1.0 - 3.0	7
3.0 - 5.0	2
5.0 - 7.0	3
7.0 - 9.0	3
9.0 - 11.0	5
11.0 - 13.0	3
13.0 - 15.0	6

### 6.3.2 Pre-Consolidation and Triaxial Consolidation

Five thin sections made from pre-consolidation samples, *i.e.* from the filter cake, were measured. As described in Chapter Two, the pre-consolidation in the filter press was one-dimensional consolidation. From slurry to cake, the soil has been compressing gradually under the vertical pressure, and no lateral strain could occur. Fig.6.5 gives the typical microstructure at this stage, which shows that a certain anisotropy has developed in the soil during the preparation of the cake in the filter press. In this stage, most of the particles turned into the horizontal direction, which is perpendicular to the direction of pressure.

Fig.6.6 is a micrograph of the microstructure of a thin section made from a sample after triaxial consolidation but without any shearing, *i.e.* axial

strain equal to 0%. In this micrograph, a blotchy appearance can be seen, and particles are arranged somewhat randomly, even though there are still some horizontal particles. At this stage, the pressure of consolidation (7 bar) was much higher than that in the pre-consolidation stage (1 bar); and the consolidating pressures were now equal in the three dimensions; thus, the sample could be deformed in lateral directions as well as vertical. According to these conditions, the sample in the triaxial cell could be compressed in three dimensions, so the particles in the soil could move freely as the water in the voids discharged and the volume decreased; thus, some changes of the microstructure in the soil had occurred from one-dimensional consolidation to three-dimensional consolidation. It can be expected that the Anisotropy

Table 6.2

Parameter	Pre-Consolidation	Consolidation
A1	0.585	0.334
SD	0.062	0.103
A2	0.692	0.494
SD	0.126	0.148
CR	0.855	0.746
SD	0.092	0.108
Ang, PMPA	9.15	12.07
T, POLMAP	16.945	21.34
Chord Size	46.95	21.16

Note: The values are the average values of five thin sections for pre-consolidation and of six thin sections for consolidation, respectively.

Indices should decrease; but the preferred direction of particles may either remain in the horizontal direction because down-left and down-right cancel each other, or if down-left and down-right do not cancel, the preferred direction may change from horizontal to inclined. The relative data measured from PMPA, POLMAP and POLMAP4 are listed in Table 6.2, which proved the above hypotheses, that is, the change of consolidating pressures and consolidating conditions have caused a change of anisotropy in the soil, say, from strong to weak, and a slight change of preferred orientation. The average chord sizes are also given in Table 6.2. A decrease of chord size is seen.

Therefore, before shearing, some changes of the microstructure of the soil had occurred. After triaxial consolidation, the Anisotropy Indices became lower; the chord sizes also decreased; and the main preferred orientation of particles changed a little even though it remained low.

### 6.3.3 Shearing

There was more scatter in these results than had been anticipated. Therefore, the results will be presented first; then the trends of the averages will be discussed; and finally it will be suggested that the variability of these samples increases as strain increases. Although they did not prove to be significant, quadratic regressions are superimposed on some graphs to illustrate the discussions.

*i. Preferred Orientation*

Figs.6.7.a and b show respectively the relationships against axial strain of the angles of preferred orientation measured by the microphotometric method, PMPA, calculated in two different ways. The value of angle at each point in Fig.6.7.a is the modulus of the algebraical average of values measured from five fields each 1.5 mm diameter in one thin section. Thus, each point represents the overall preferred orientation of one sample. All the orientations in Fig.6.7.a are close to the horizontal. Therefore, these observations eliminate the hypothesis that particles throughout the sample gradually turn into the direction of the failure plane.

Fig.6.7.b shows the same observations reduced in a different way. Each point is the average of the moduli of the values from the five fields. Thus, each point represents the average orientation of a field 1.5 mm diameter. These values are all low, which supports the conclusion from Fig.6.7.a. However, the values in Fig.6.7.b are larger than those in Fig.6.7.a, suggesting that the preferred orientation within the individual fields 1.5 mm diameter tends to deviate from the horizontal but to cancel out this effect throughout the sample. The results in Fig.6.7.b seem to show a very slight upward trend with strain (and there are no low values at high strains), but this trend did not prove to be significant when tested with linear regression. If the trend were to be real, it would mean that shear caused rotation of the particles at the 1.5 mm diameter scale.

Figs.6.8.a and b show respectively the relationships against axial strain of the angles of preferred orientation measured by the image analysis method, POLMAP4, calculated in two different ways. The value of angle at each

point in Fig.6.8.a is the modulus of the algebraical average of values measured from four fields each 0.47 mm square in one thin section, these fields being located between the five fields used for Fig.6.7.a. Apart from slightly higher values at low strain, all the points in Fig.6.8.a are in the same region as those in Fig.6.7.a, thus, reinforcing the conclusion that the overall preferred orientation remains horizontal.

Each point in Fig.6.8.b is the average of the moduli of the values from the four fields. Thus, each point represents the average orientation of field 0.47 mm square. These values are all low. However, the values in Fig.6.8.b are higher than those in Fig.6.7.b, thus suggesting that the preferred orientation within the individual fields 0.47 mm square tends to deviate from the horizontal more than the preferred orientation within the larger fields 1.5 mm diameter does.

## ii. *Anisotropy*

Figs.6.9.a, 6.9.b and 6.9.c show respectively the relationships against axial strain of A1, Anisotropy Index, measured by PMPA, A2, Anisotropy Index, measured by POLMAP, and CR, Consistency Ratio, measured by POLMAP4. Each point is the arithmetical average of the 5 or 4 fields for one sample.

It seems that the changes of the strength of anisotropy with axial strain may be divided into three stages, at low strain 0 - 5%, at intermediate strain 6 - 10%, and at high strain greater than 10%. Tentatively, it shows that A is increasing for low strain, then it remains unchanged, roughly speaking, at the intermediate stage, and thereafter, a scatter is created.

The microphotometer results in Fig.6.9.a are difficult to interpret. Linear regression showed a very slight upward trend which was not significant. Visual examination suggests that the unstrained samples were more uniform than the strained samples. Also, it seems that there may be an increase of anisotropy up to about 5% strain. From 6% to 10% strain, say, there is perhaps no change of anisotropy. Thereafter, there is perhaps a slight fall. These suggestions agree with the quadratic regression, although this was not shown to be significant.

Linear regression for the results in Fig.6.9.b for the smaller areas measured in POLMAP showed a very slight upward trend which was not significant. Quadratic regression showed a roughly similar result as that for the results in Fig.6.9.a. Again the most notable effect is an increase in the scatter of the results as strain progresses.

The results for POLMAP4 in Fig.6.9.c are in general agreement with the preceding observations. Linear regression showed a very slight upward trend which was not significant. As for the Fig.6.9.c, anisotropy (here measured by CR) seems to rise from 0 - 5%, then to stay constant to, say, 10%, then perhaps to fall. Quadratic regression showed an increase at the lower strain, say, about 0 - 8%, then a decrease at the strain greater than 8%, but this again did not achieve significance. In this diagram, the increase of scatter with strain is less pronounced.

### iii. Chord Size

The chord sizes of the areas mapped in POLMAP4 were measured to give extra information about the grouping of the particles into similar

directions. As explained in Chapter 4, four directions were used with a few points being labelled undecided. The results are shown in Fig.6.10. Linear regression showed a small upward trend, but this was not significant. When averaged, none of the 6 unstrained samples showed large chord sizes. After strain, 5 of the samples showed large chord sizes. However, many of the strained samples showed small chord sizes.

These results might be explained by the hypothesis that strain was accommodated in some samples by an increase in chord size, but other samples deformed without altering the chord size. This point will be discussed further below.

#### 6.3.4 Standard Deviation

In order to estimate the consistency of the measured results, standard deviations were calculated at levels corresponding to the previous results. First, the standard deviations, SD1, of Anisotropy Index A1 from the photometer with the five measurements of each thin section were calculated (Fig.6.11.a). SD1 measures the variation between areas 1.5 mm diameter. The results possibly show no trend as the axial strain increases.

Secondly, the standard deviations, SD2, of Anisotropy Index, A2, from POLMAP were calculated for each thin section using the four measurements obtained for each thin section (Fig.6.11.b); at the same time, the standard deviations, SD4, of Consistency Ratio, CR, from POLMAP4 were calculated for each thin section using the same four measurements (Fig.6.11.c). Both SD2 and SD4 measure the variations between areas 0.47 mm square. From Figs.6.11.b and 6.11.c, no significant change appeared, even though they

possibly show a slight decrease of standard deviations against the axial strains. The values of SD2 seem to be greater than those of SD4, but this is because the values of CR were tending to a limit at 1.0. In general, the values of SD1 were lower than SD2. The respective averages were  $SD1 = 0.113$ ,  $SD2 = 0.183$  for all samples. The ratio  $SD1/SD2 = 0.617$  which may be compared with the ratio of the average of the values of A1 and A2 plotted in Fig.4.9 which is  $A1/A2 = 0.399/0.490 = 0.814$ .

Finally, the standard deviations (SDG1, SDG2, SDG4, and SDS) of Anisotropy Indices, Consistency Ratio, and Chord Sizes based on the mean values of each thin section were calculated for each of the eight groups of strained samples defined in Table 6.1 (excluding pre-consolidation). This being based on results for whole samples, measures the variation between samples. These values are plotted against the nominal strain of each group in Fig.6.12 and Fig.6.13. These figures suggest that the variability between samples increases as strain increases.

### 6.3.5 Discussions

The measurements of orientation reported above show that the preferred orientation in the samples remained almost horizontal throughout the range of deformation considered (excluding changes in the failure plane itself). The measurements, however, did suggest that there might have been some relatively small scale changes of orientation which cancelled overall. The strength of anisotropy remained substantially constant throughout. This is in agreement with the hypothesis that in almost isotropic samples 'particles' would slip into more ordered positions increasing the anisotropy, whilst in the strongly anisotropic samples particles would push past each other decreasing

the anisotropy. The hypothesis that two mechanisms were acting in these samples is given some support by the quadratic trend which many of the graphs seemed to show, even though this trend was not found to be significant. Although no similar observations have been reported previously, the apparent increase in variability between samples as strain increases suggests that one mechanism may be dominant in some samples, whilst another mechanism may be dominant in others.

#### 6.4 Normally Consolidated Drained Triaxial Testing

All of the thin sections either for normally consolidated drained shearing or overconsolidated drained shearing discussed here and in the next section were made by the University of East Anglia; they were examined in optical microscopy only. The corresponding analysis for Scanning Electron Microscopy is being made in the University of East Anglia and exceeds the scope of this study.

The procedure of normally consolidated drained triaxial testing was similar to the normally consolidated undrained triaxial testing, except that the nominal pressure at the end of pre-consolidation was 7 bar, and the cell pressure was 7 bar too. The clay was nominally the same but was a different batch (Appendix A).

Fig.6.14 shows a set of typical micrographs from low axial strain to high axial strain to describe qualitatively the microstructural variation of clay in normally consolidated drained shearing.

The initial values of the Anisotropy Indices, both  $A_1$  and more especially

A2, are higher for the normally consolidated drained shearing samples than for the normally consolidated undrained shearing samples, see Table 6.3, which includes the values for over-consolidated drained triaxial shearing also. The higher values presumably result from the higher pre-consolidation pressures which were possible in the filter presses in the University of East Anglia.

Table 6.3 Initial Values

	A1	A2	ANG	CS
NCU	0.33	0.49	12.1	21.2
NCD	0.40	0.83	16.4	56.9
OCD	0.52	0.64	9.0	29.4

Figs.6.15.a and b show respectively the relationships against axial strain of A1, Anisotropy Index, measured by PMPA, and A2, Anisotropy Index, measured by POLMAP. Each point is the arithmetical average of the 5 or 4 fields for one sample.

As the strain increases, the Anisotropy Indices, A1, for the 1.5 mm diameter fields from the photometer shown in Fig.6.15.a, seem to rise at first and then perhaps to decrease slightly until failure occurs at about 15% strain.

The Anisotropy Indices, A2, for the 0.47 mm square fields from the image analysis shown in Fig.6.15.b, may increase with shear, but only slightly, presumably because the initial values are already high. There are, however, a few low results at low strain.

Each point in Fig.6.16 shows the modulus of the algebraical average of the five values of orientation obtained by the photometer for each sample. This corresponds to Fig.6.7.a for the undrained case. Again, all the observations in Fig.6.16 are close to the horizontal.

The average chord sizes for each sample measured by POLMAP are in Fig.6.17, the trend apparently being concave upwards.

### 6.5 Over Consolidated Drained Triaxial Testing

The University of East Anglia supplied 18 thin sections for the over consolidated drained triaxial test series. The clay was nominally the same as mine but was a different batch. The nominal pressure at the end of pre-consolidation was 7 bar, and the pressure for the triaxial consolidation was 7 bar too, but the cell pressure was released to 1 bar before starting to shear.

The range of axial strain for which the thin sections are available from the over consolidated drained shearing is from 0% to 6% with failure occurring at 8% strain. For convenient analysis and discussion below, the

Table 6.4 Over-consolidated Drained Samples

	No. of Thin-Section	Axial Strain(%)
Group one	3	0.0
Group Two	10	1.5
Group Three	5	5.0

samples are divided into three groups based on the axial strain, see Table 6.4.

The qualitative observation of the microstructure under the optical microscope suggested that the microstructure for the over consolidated drained shearing at low axial strain has the following characteristics: (1) the degree of anisotropy which existed in the soil before shearing was high; but random areas also were seen; (2) patches slightly increased as the axial strain increased.

The results of measurements from methods POLMAP and PMPA under the optical microscope further provided observations, shown in Table 6.5 and Figs.6.18, 6.19 and 6.20. The Anisotropy Index, A1, showed a slight increase with the axial strain (Fig.6.18.a), but the initial value for  $\epsilon = 0\%$  is larger than that in normally consolidated drained shearing, and there is a lot

Table 6.5

Strain (%)	A1	A2	Angle	Chord-Size
0.0	0.52	0.64	8.99	29.4
1.5	0.51	0.88	0.0	50.0
5.0	0.56	0.91	5.0	55.0

Note: The values shown here are the modulus of the algebraical average values from same group.

of scatter at low strain. The Anisotropy Index, A2, seemed to increase with the increase of axial strain (Fig.6.18.b). The direction of the preferred orientation was always close to the horizontal and the algebraical averages in Table 6.5 show this result even more clearly, whilst it appeared to decrease

with strain (Fig.6.19). There is again a large scatter at low strain. As far as can be seen from the results available, the chord size appeared to increase with the axial strain (Fig.6.20).

## 6.6 Summary

In all three series, the preferred orientation was originally close to the horizontal and remained close to the horizontal as strain increased. Except for A1 for the over-consolidated series, the graphs of strength of anisotropy vs. strain appeared to be concave downwards. For both normally consolidated undrained and drained shearings, the chord sizes in some of the samples increased with strain; but in other samples, the chord sizes appeared not to change. For the normally consolidated undrained shearing, the between-samples standard deviation appeared to increase with strain.

The results for the normally consolidated undrained shearing will be discussed further after the corresponding electron microscopy has been reported in the next Chapter.

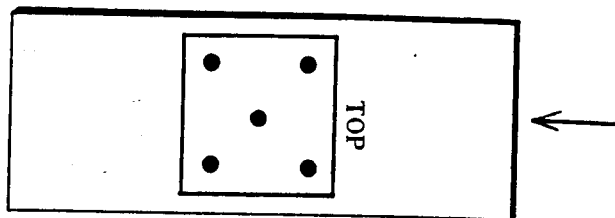


Fig.6.1 Illumination of the Position of the Fields Measured by PMPA.

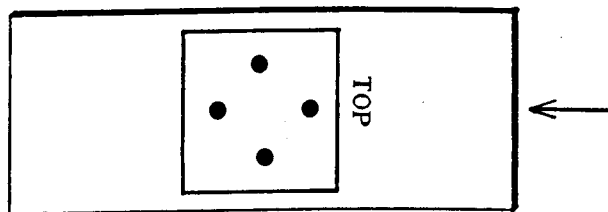
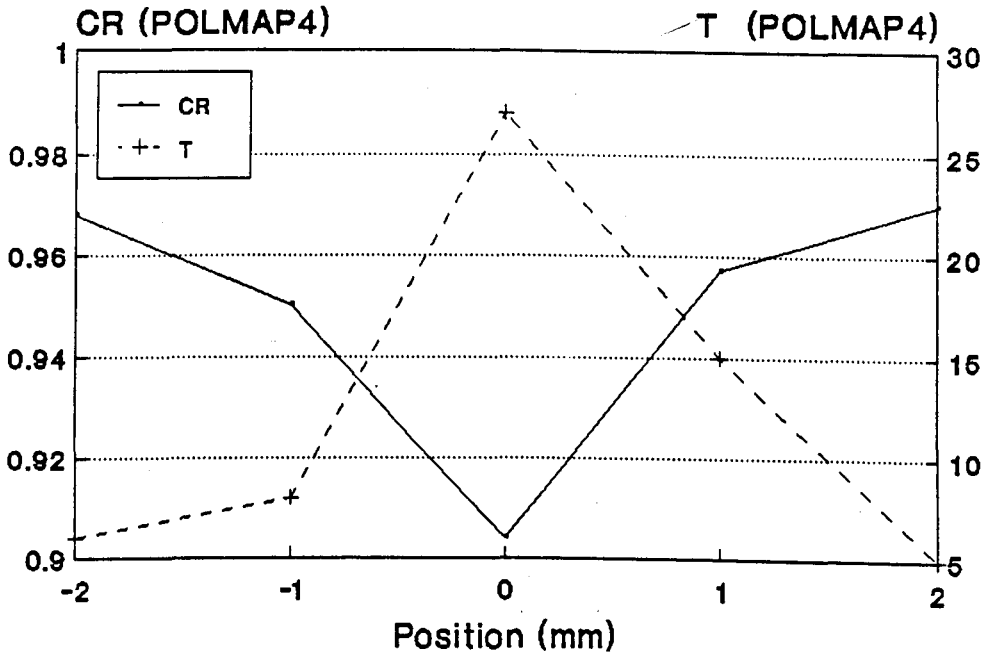
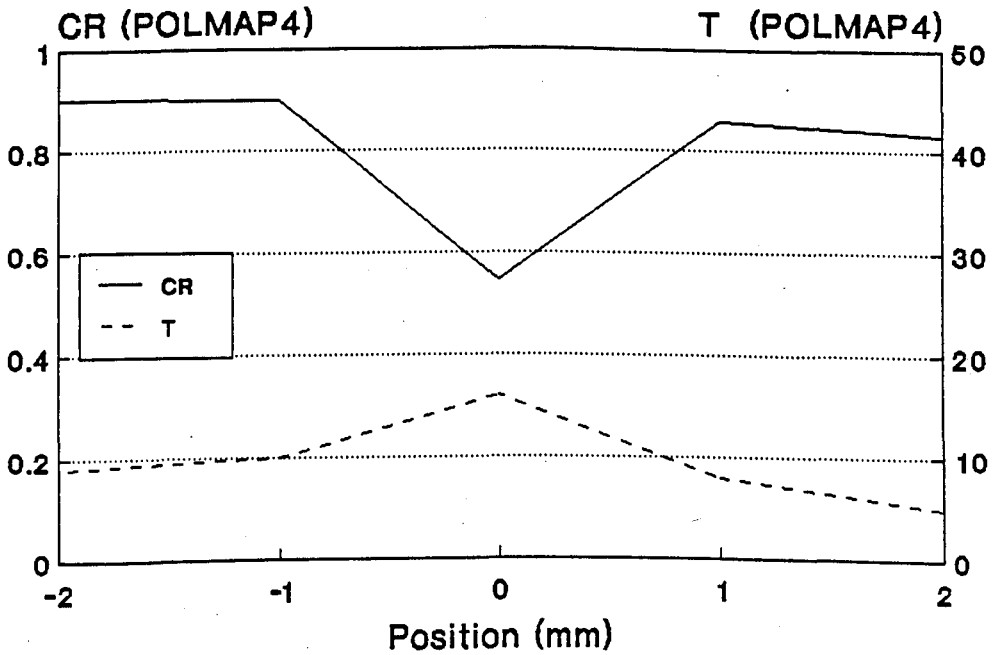


Fig.6.2 Illumination of the Position of the Field Measured by POLMAP and POLMAP4.



*Fig.6.3* POLMAP4 Measurements across a Failure Plane for the Normally Consolidated Undrained Shearing, (T = inclination to horizontal).



*Fig.6.4* POLMAP4 Measurements across a Failure Plane for the Normally Consolidated Drained Shearing, (T = inclination to horizontal).

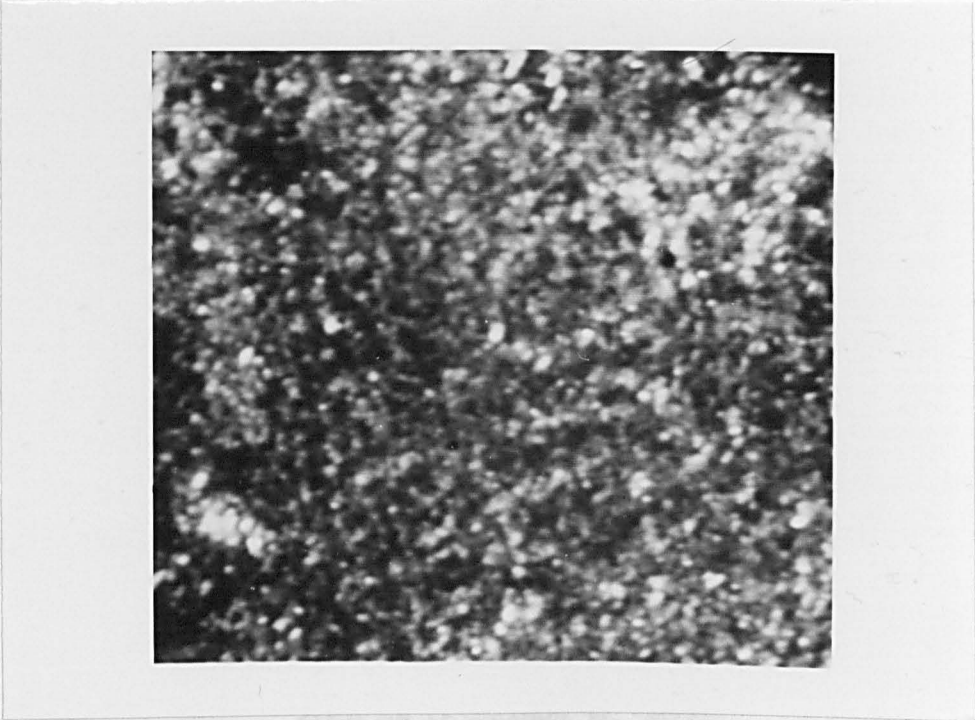


*Fig.6.5* Micrograph of Pre-Consolidation Sample for Normally Consolidated Undrained Shearing.

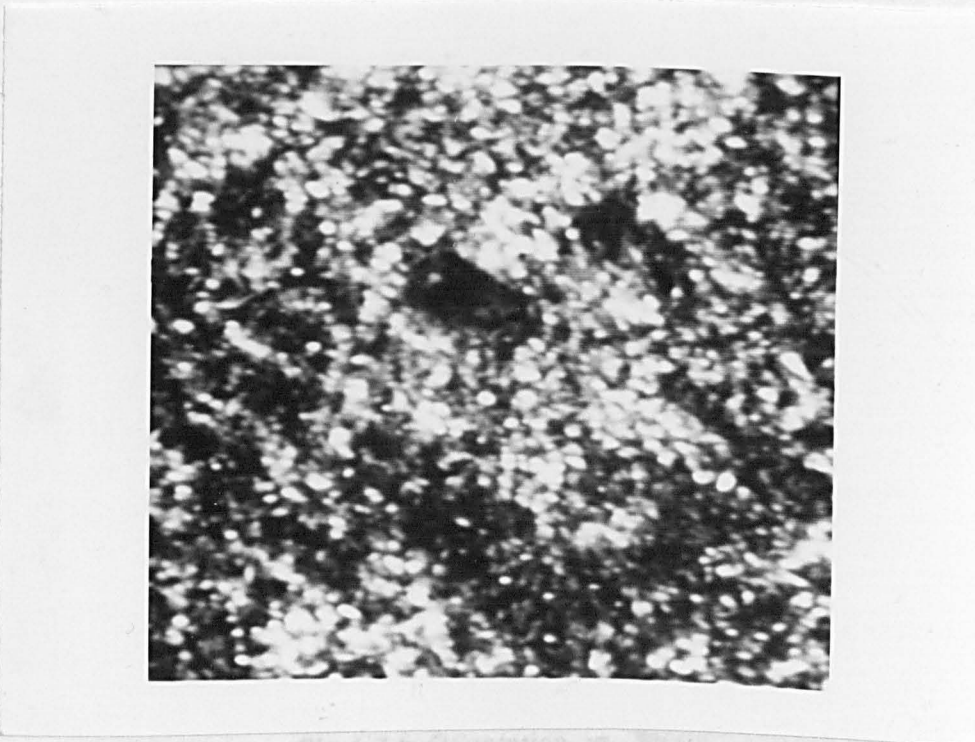


*Fig.6.6* Micrograph of Triaxial Consolidation Sample for Normally Consolidated Undrained Shearing.

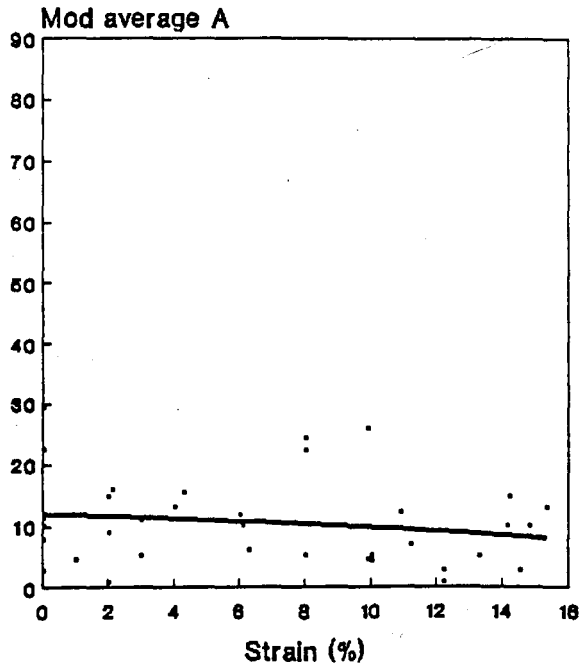


Fig.6.7.a Orientation vs. Strain

Normally Consolidated Undrained Shearing  
 Mod average A inclined from Horizontal.

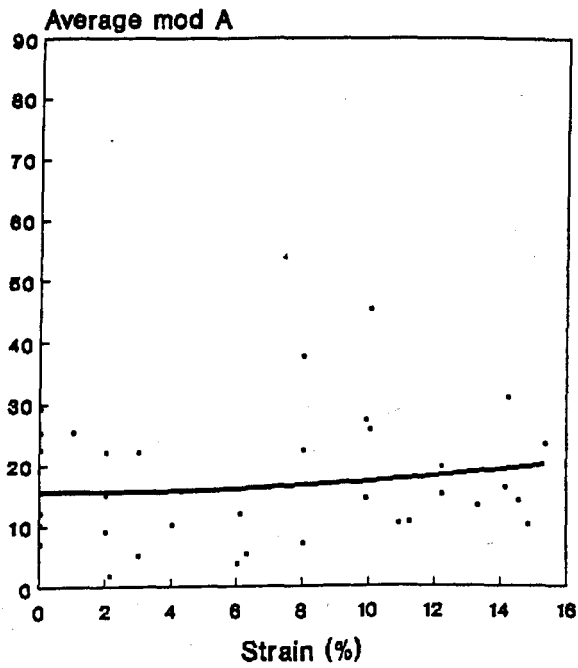
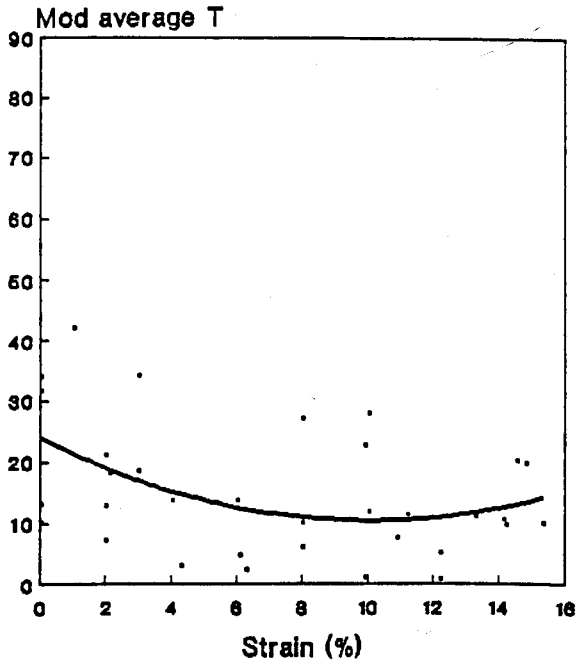


Fig.6.7.b Orientation vs. Strain

Normally Consolidated Undrained Shearing  
 Average mod A inclined from Horizontal.



*Fig.6.8.a* Orientation vs. Strain

Normally Consolidated Undrained Shearing

Mod average T inclined from Horizontal.

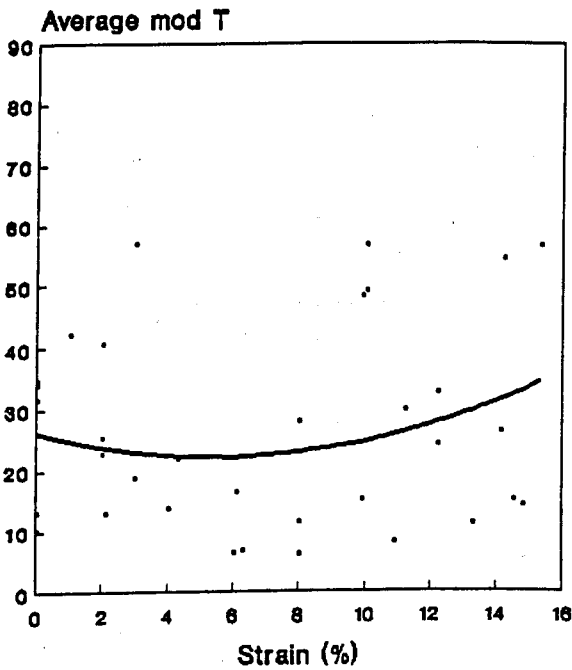


*Fig.6.8.b* Orientation vs. Strain

Normally Consolidated Undrained Shearing

Average mod T inclined from Horizontal.

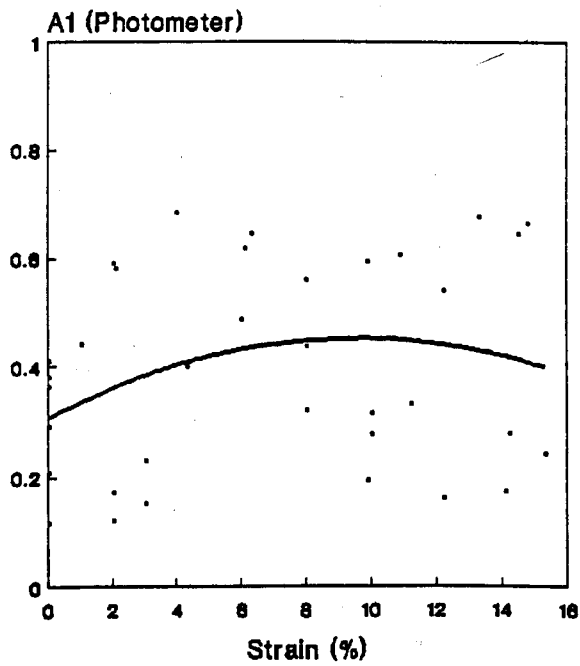


*Fig.6.9.a* Anisotropy Index A1 vs. Strain  
Normally Consolidated Undrained Shearing.  
(From photometer PMPA, area 1.5 mm diameter).

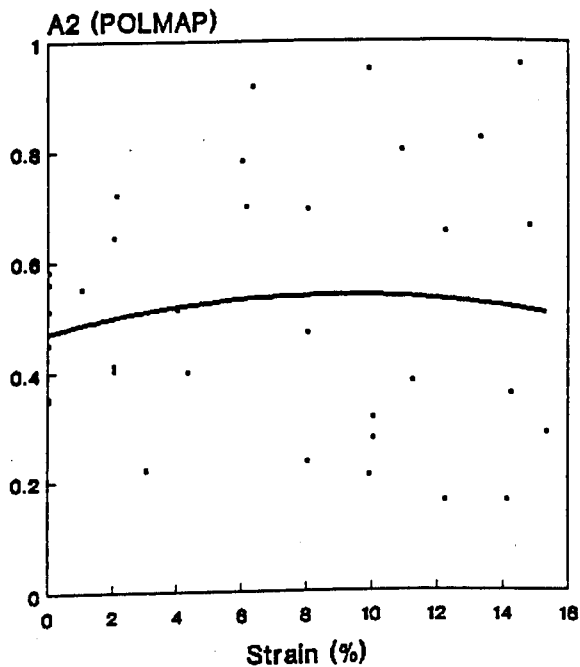


*Fig.6.9.b* Anisotropy Index A1 vs. Strain  
Normally Consolidated Undrained Shearing.  
(From POLMAP, area 0.47 mm square).

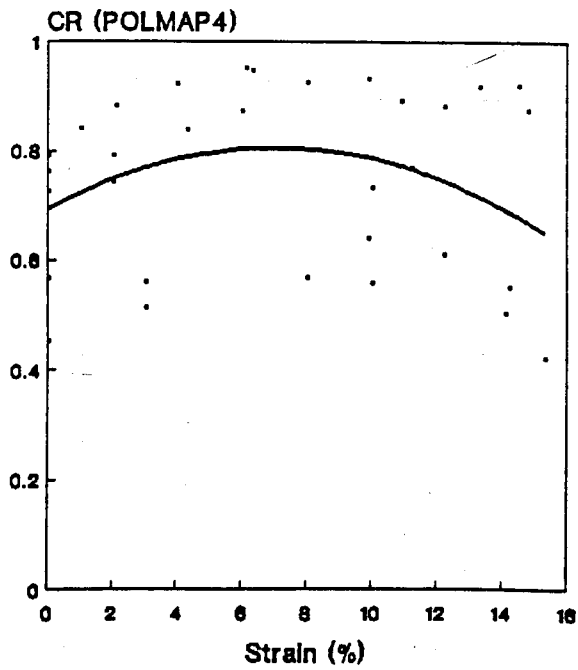


*Fig.6.9.c* Consistency Ratio CR vs. Strain  
Normally Consolidated Undrained Shearing.  
(From POLMAP4, area 0.47 mm square).

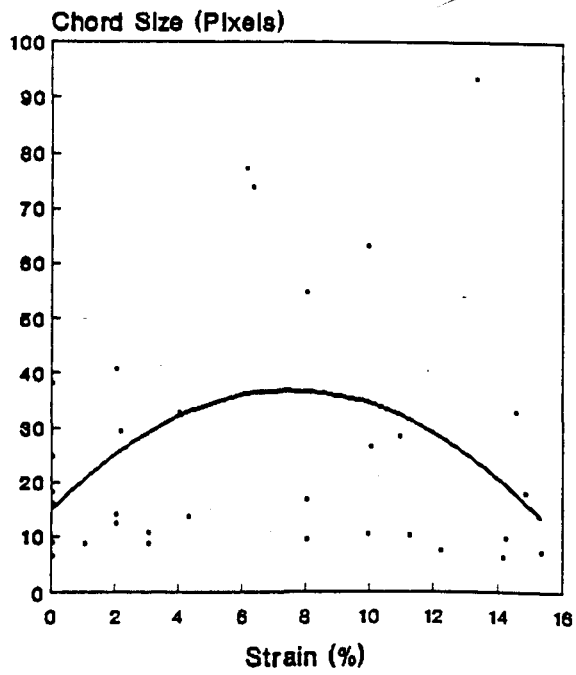


*Fig.6.10* Chord Size vs. Strain

Normally Consolidated Undrained Shearing.

(From POLMAP4, area 0.47 mm square).

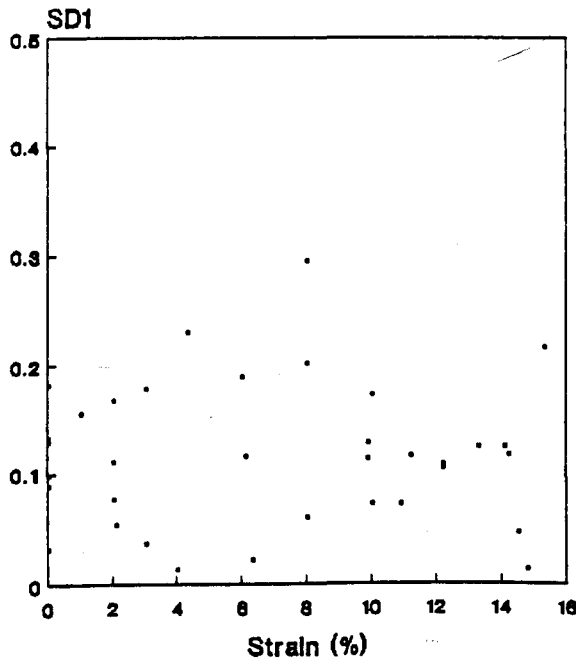


Fig.6.11.a Standard Deviation SD1 vs. Strain  
 Normally Consolidated Undrained Shearing.  
 (From PMPA, within samples, 5 x 1.5 mm).

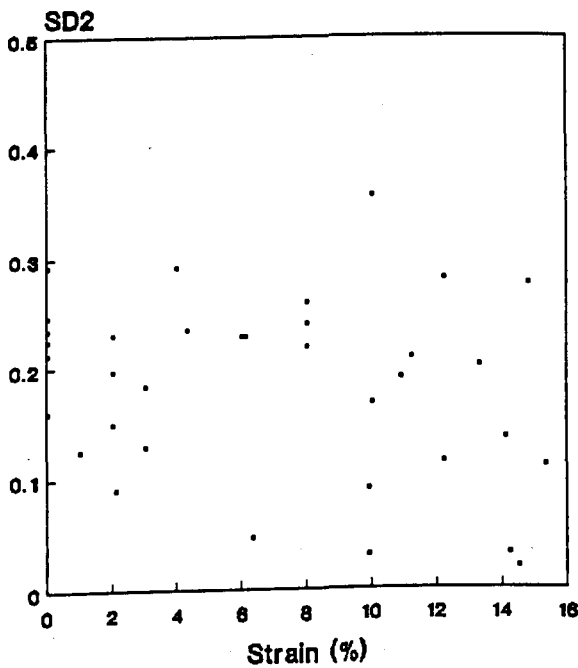
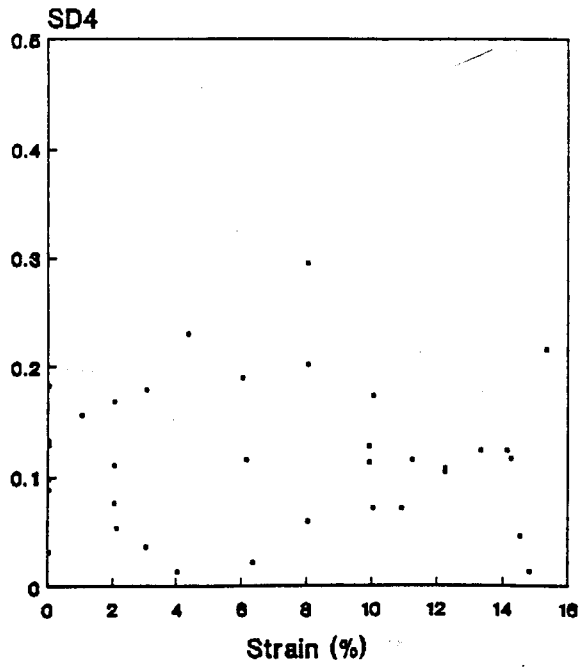


Fig.6.11.b Standard Deviation SD2 vs. Strain  
 Normally Consolidated Undrained Shearing.  
 (From POLMAP, within sample, 4 x 0.47 mm).



*Fig.6.11.c* Standard Deviation SD4 vs. Strain  
Normally Consolidated Undrained Shearing.  
(From POLMAP4, within sample 4 x 0.47 mm).

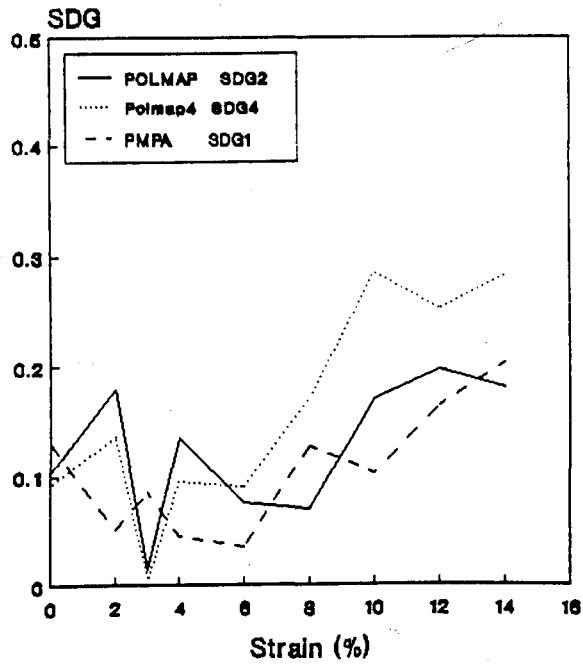


Fig.6.12 Standard Deviation vs. Strain  
Normally Consolidated Undrained Shearing.  
(For Anisotropy, between samples).

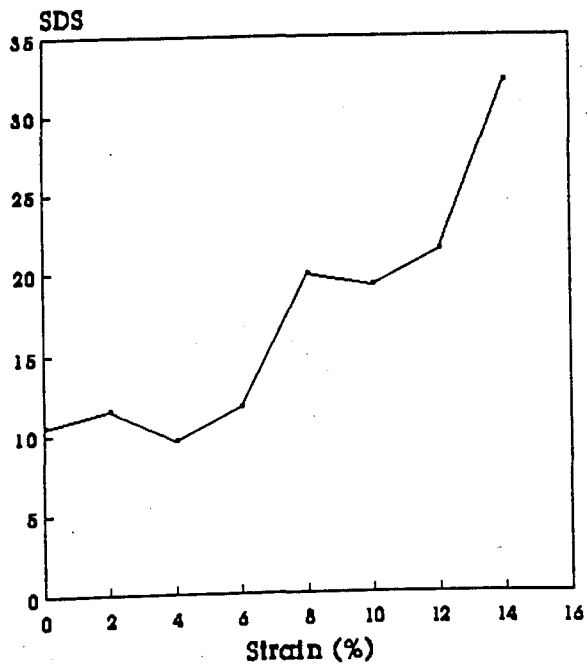
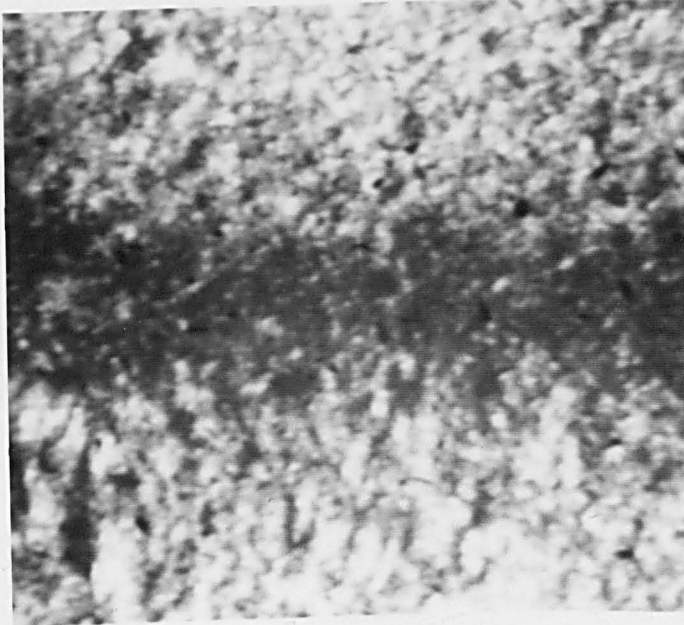


Fig.6.13 Standard Deviation vs. Strain  
Normally Consolidated Undrained Shearing.  
(For Chord Sizes, between samples).



*Fig.6.14.a* Micrograph of Triaxial Consolidation Sample  
For Normally Consolidated Drained Shearing.



*Fig.6.14.b* Micrograph From Normally Consolidated  
Drained Shearing Sample ( $\epsilon = 6\%$ ).

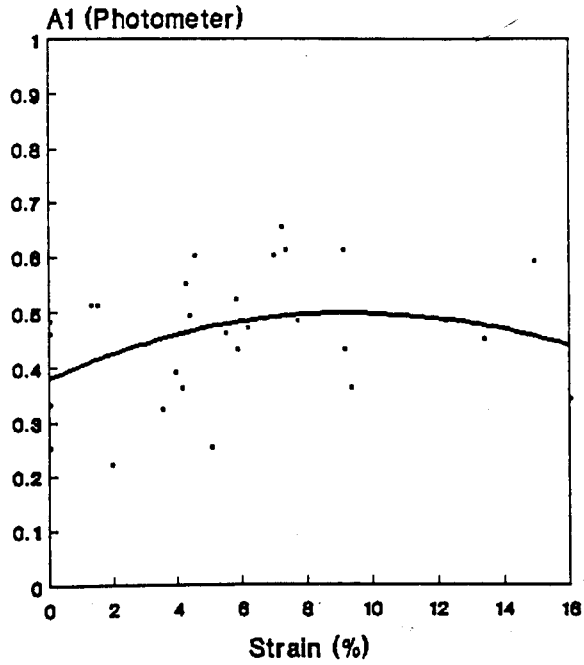


Fig.6.15.a Anisotropy Index A1 vs. Strain  
Normally Consolidated Drained Shearing.  
(From photometer, area 1.5 mm diameter).

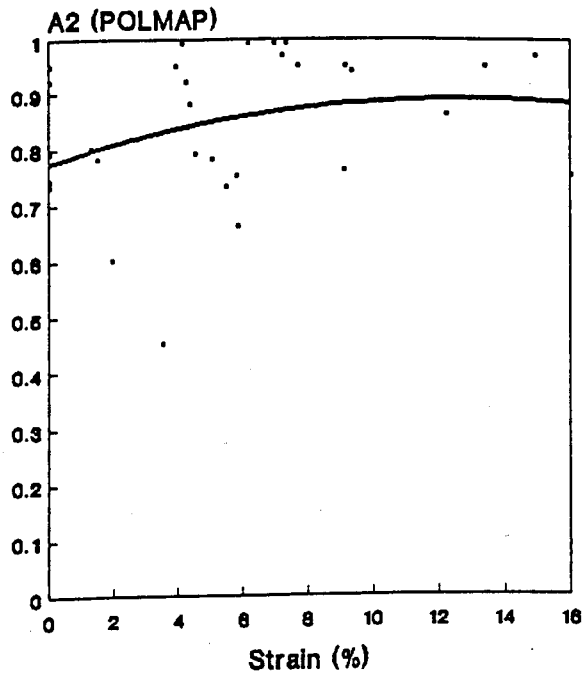


Fig.6.15.b Anisotropy Index A2 vs. Strain  
Normally Consolidated drained Shearing.  
(From POLMAP, area 0.47 mm square).

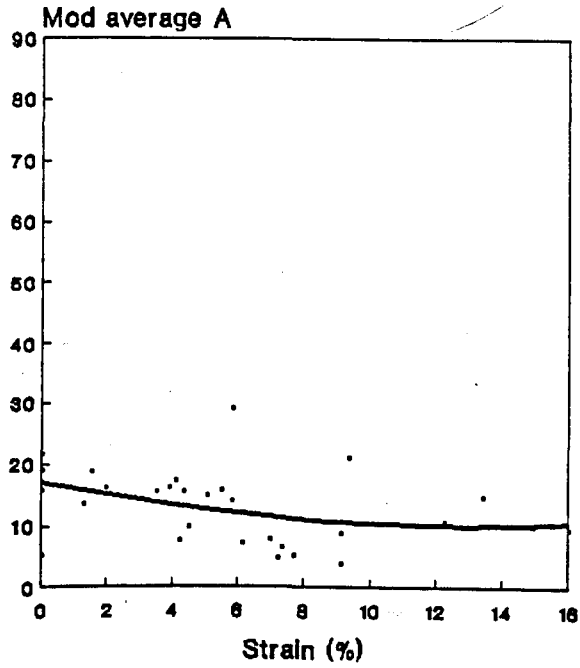


Fig.6.16 Orientation vs. Strain

Normally Consolidated Drained Shearing.

(From photometer, area 1.5 mm diameter).

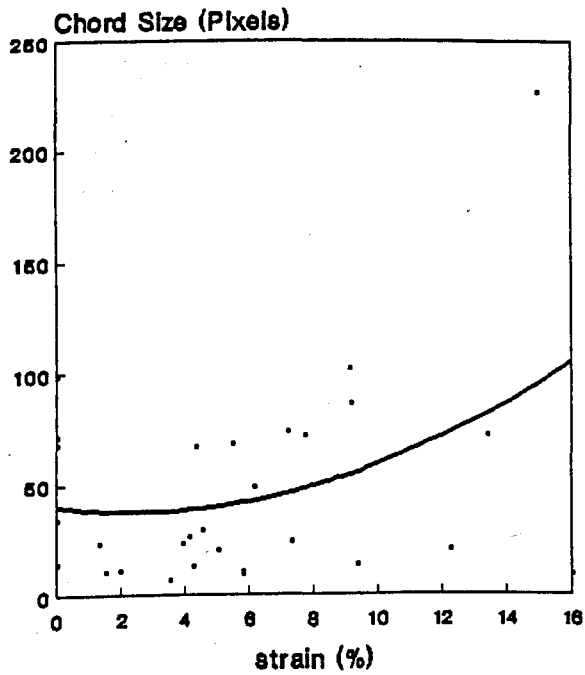


Fig.6.17 Chord Size vs. Strain

Normally Consolidated Drained Shearing.

(From POLMAP, area 0.47 mm square).

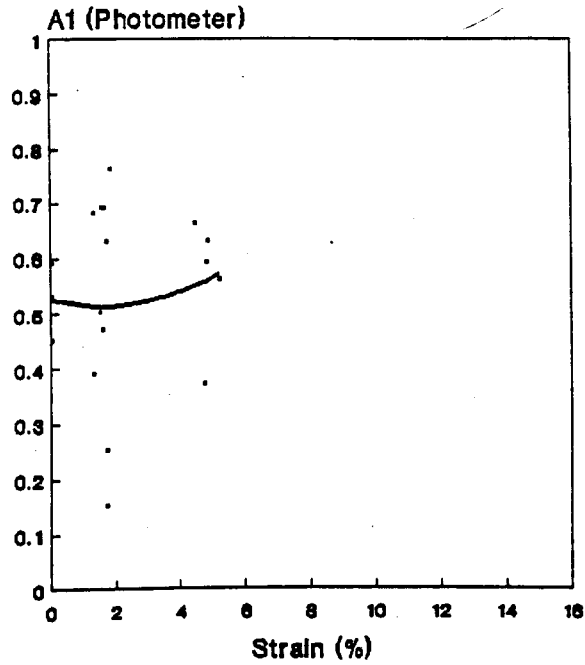


Fig.6.18.a Anisotropy Index A1 vs. Strain  
Over-Consolidated Drained Shearing.  
(From photometer, area 1.5 mm diameter).

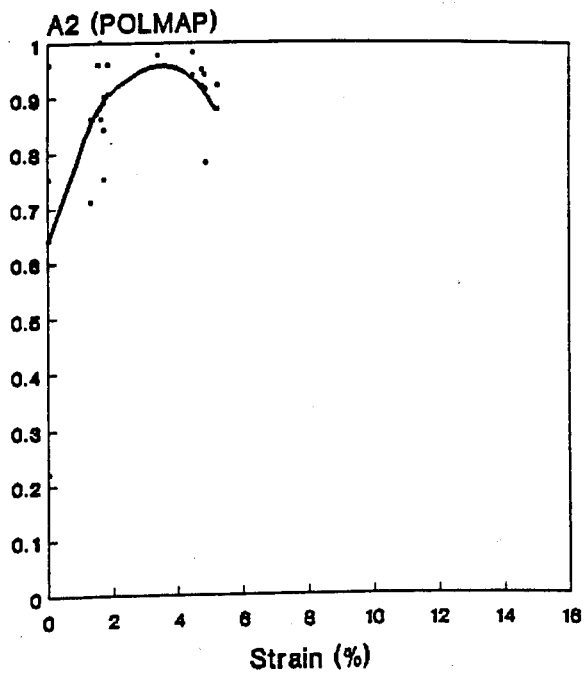


Fig.6.18.b Anisotropy Index A2 vs. Strain  
Over-Consolidated Drained Shearing.  
(From POLMAP, area 0.47 mm square).

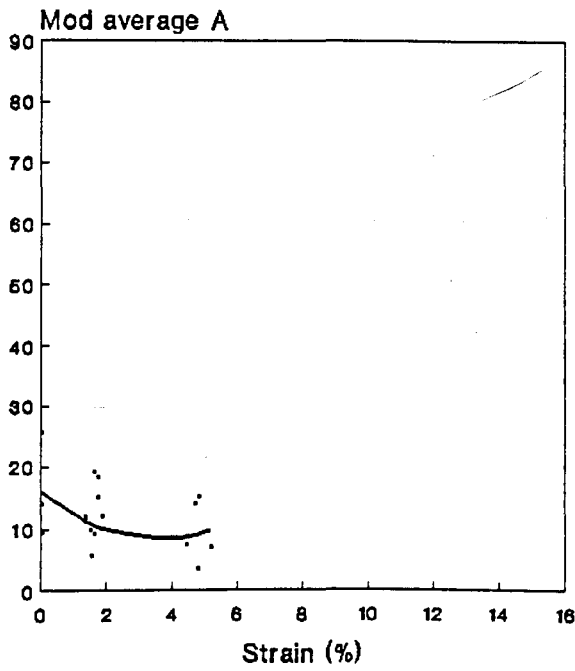


Fig.6.19 Orientation vs. Strain

Over-Consolidated Drained Shearing.

(From photometer, area 1.5 mm diameter).

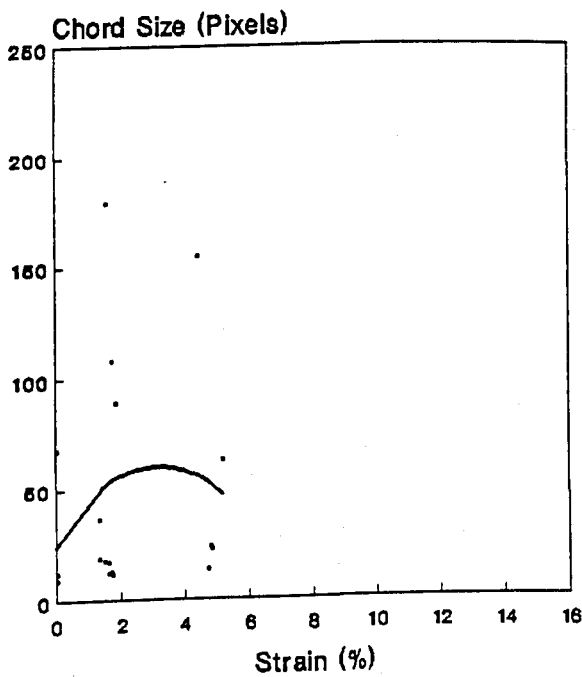


Fig.6.20 Chord Size vs. Strain

Over-Consolidated Drained Shearing.

(From POLMAP, area 0.47 mm square).

## Chapter Seven

### OBSERVATIONS OF SCANNING ELECTRON MICROSCOPY

#### 7.1 Introduction

In this chapter, observations which were carried out in the scanning electron microscope will be discussed; and the discussion will be related to the observations of features obtained under polarised light which were reported in the previous chapter. The specimens for the observations with the scanning electron microscope were from the normally consolidated undrained triaxial shearing. The procedures of the experiments and of the specimen preparation were discussed in Chapters 2 and 3.

For the scanning electron microscope image analysis, there were three methods which were mainly used in this thesis. They are named PICDIF, PICCON and PICPOR (Chapter 5).

In general, 25 images were taken from each specimen (Fig.5.1), and the magnification was 4000x, giving a  $25 \mu\text{m} \times 23.5 \mu\text{m}$  field as mentioned in Chapter 5. All the images for each sample had been obtained from the same block; so the orientations in all micrographs for one sample were measured in the same sense. However, as for the optical microscopy, anticlockwise in one sample may have corresponded to clockwise in another. Therefore, the orientations here and throughout this chapter have been given in the range  $0 - 90^\circ$ .

## 7.2 Comparisons of Methods

### 7.2.1 Comparison between Internal Methods

In this thesis, the methods PICDIF, PICCON and PICPOR were used in the image analysis. Of those, PICCON is believed to be the most accurate method. The comparisons of the results of these three methods are discussed below.

#### i. *Comparison of PICCON and PICDIF*

Each point in Fig.7.1 shows the preferred orientation from PICCON for one specimen plotted against the corresponding value from PICDIF, which gives a very good agreement. Note that there are two points which have very high values of orientation. These will be discussed later.

Fig.7.2 shows the relationship of the Consistency Ratios obtained from PICCON and PICDIF, which also gives a good agreement. The Consistency Ratio measured from PICCON was higher than that from PICDIF, which is expected, because PICCON took the mean vector from the smoothed images, and it is thought that in the smoothing, the effect of the ends of particles was removed as mentioned in Chapter 5.

The histogram of preferred orientations obtained from PICCON is shown in Fig.7.3. Remembering that the orientations have been folded into  $0 - 90^\circ$ , it is clearly seen that the distribution of angles is like a normal distribution, with mean approximately zero. The two high points mentioned above are far out of the region. The standard deviation is 17.07, so the possibility of  $63^\circ$  appearing

is 0.3 and the possibility of  $84^\circ$  appearing is less than 0.3. Therefore, these two values might be errors caused accidentally during the procedure of cutting and making the specimen (see Chapter 3). Thus, they will be omitted from the following analysis of preferred orientation.

## ii. Comparison of PICCON and PICPOR

Fig.7.4 and 7.5 show respectively the relationships of preferred orientation from PICCON against that from PICPOR and the Consistency Ratio from PICCON against that from PICPOR. Both of them give good agreement, except that more scatter is present than in Fig.7.1 and 7.2. This is because PICPOR analysed the image in a different way based on the density of local areas. (Again there are two high values in Fig.7.4, which are out of the normal region). Most of the preferred orientations from PICPOR are higher than that from PICCON, but the Consistency Ratios from PICCON are higher than that from PICPOR.

In summary, the three methods of image analysis give satisfactory agreement, the Consistency Ratio from PICCON being higher than the others as expected. The results from PICPOR show more scatter, but this was considered to be not serious.

### 7.2.2 Comparison between Optical Microscopy and Scanning Electron Microscopy

Some comparisons between the optical microscopy and scanning electron microscopy were made. Because the measurements for scanning electron microscopy were based on the combined Consistency Ratio for the 25 images, the comparison for strength of anisotropy was made between the combined Consistency

Ratio, CR2, from PICCON, and the combined Consistency Ratio, CR, from POLMAP4. The comparison for preferred orientation was made between the value, ANG2, from PICCON, and the average value, ANGP, of the nine fields from PMPA and POLMAP.

Fig.7.6 shows the relationship of ANG2 against ANGP. The two points at top left are for the two bad samples mentioned above. The fact that they have low orientations in the optical microscopy reinforces the decision to omit them from the analysis. The average preferred orientation, ANGP, of the nine fields was the algebraical average weighted by the number of fields. All the values are low, the region being limited below  $35^\circ$ . This seems to be a trend deviating from the 1:1 line, which means that the values of ANGP from polarising are smaller than those of ANG2 for the smaller fields in the scanning electron microscope. However, there is some scatter.

Fig.7.7 Shows the relationship of CR from POLMAP4 against CR2 from PICCON. Both measurements rise together. Almost all of the points are above the 1:1 line, which means that the CR for POLMAP4 is higher than CR2 for PICCON. There is more scatter here than had been anticipated, perhaps because values were available for only 4 fields per sample for POLMAP4.

In summary, despite the remarks above, the amount of scatter in Figs.7.7 and 7.6 was disappointing. However, the most important point here is to consider the effect of shear deformation on the structure of the samples.

### 7.3 Effect of Shear Deformation

#### 7.3.1 Introduction

In order to illustrate the discussion of the effect of shear deformation on the microstructure of the samples, quadratic regressions are superimposed on the graphs in the same way as was done for optical microscopy.

#### 7.3.2 Preferred Orientation

Figs.7.8.a to c show the relationships against strain of the angles of preferred orientation measured by PICDIF, PICCON and PICPOR. The value of angle at each point is the modulus of the algebraical average of values measured from 25 fields each  $25 \mu\text{m} \times 23.5 \mu\text{m}$  in one specimen. Thus, each point represents the overall preferred orientation of one sample. All the orientations in Figs.7.8.a to c are close to the horizontal, thus, reinforcing the conclusion that the overall preferred orientation remains horizontal. The quadratic regressions suggest that the changes of the angles with axial strain may be divided into three stages, at low strain 0 - 5%, at intermediate strain 6 - 10 %, and at high strain greater than 10%. It seems that the angle is decreasing for the low strain, then it keeps unchanged in the intermediate strain, thereafter, an increase is shown, these effects being slight.

#### 7.3.3 Anisotropy

Figs.7.9.a to c show respectively the relationships against axial strain of CR1, Consistency Ratio, measured by PICDIF, CR2, Consistency Ratio, measured by PICCON, and CR3, Consistency Ratio, measured by PICPOR. Here, each point

is the arithmetical average of 25 fields for one sample. Thus, these graphs show the strength of anisotropy at the level of individual micrographs averaged for each specimen.

It seems that the trends from scanning electron microscopy are similar to those from optical microscopy. The strength of anisotropy seems to change with axial strain; first there is an increase with axial strain, then a maximum value, then a decrease at high strain.

#### 7.3.4 Chord Size

Methods PICCON and PICPOR give the extra information: chord size the grouping of the particles into similar directions and densities, respectively. As mentioned in Chapter 5, four directions were used in PICCON with very few points being labelled either undecided or random.

There are three hypotheses to consider. Firstly, if the mapped regions are regarded simply as classes, then, because the number of classes in PICPOR is half that in PICCON, the expected chord size in PICPOR will be about twice that in PICCON. This result would arise if domains of different orientations were tightly (or loosely) aggregated into the region mapped by PICPOR. If this situation occurred, it would support the hypothesis that some at least of the structural units were small aggregates of domains with different orientations. However, PICCON could also give smaller chord size than PICPOR if the dense groups were large single domains, whilst the loose groups were jumbled conglomerations of small domains. Third, if each domain were to be separated from its neighbours by a region of low density, then in a traverse for one domain to the next, PICPOR would find two boundaries as it dipped into and

climbed out of the low density region, whereas PICCON would find only one boundary at the point where the mapped direction changed. On this basis, the chord size for PICPOR would be smaller than those for PICCON.

The results are shown in Fig.7.10. Fig.7.10.a shows the results from PICCON, and Fig.7.10.b shows the results from PICPOR. The values from PICPOR seem to be larger than those from PICCON. Several comparisons, by hand, of the regions mapped respectively by PICCON and PICPOR have been made, which shows that the dense groups mainly consist of single large particles or domains, but the loose groups are aggregated small particles and domains. This interpretation is the second hypothesis as mentioned above.

#### 7.4 Summary

The results of electron microscopy appeared to agree with the corresponding results from optical microscopy. The preferred orientation was close to horizontal, and during shearing it seemed not to change. The consistency ratio showed the same trend, concave downwards. The chord sizes measured by both methods PICCON and PICPOR appeared to remain constant as strain increased.

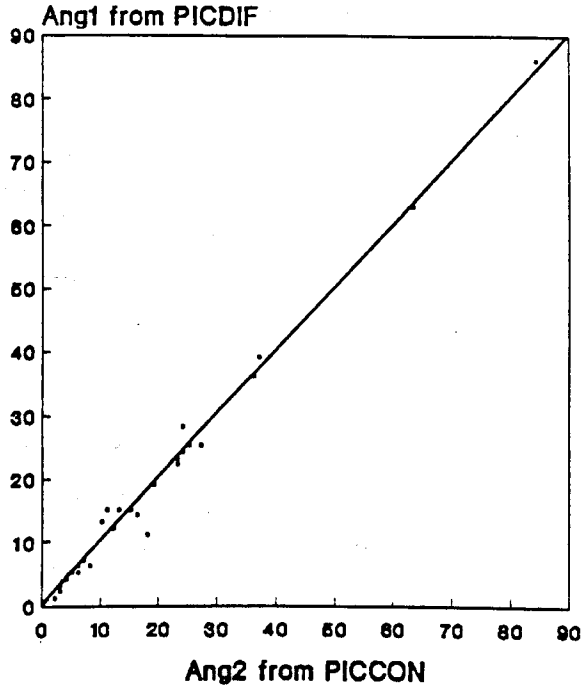


Fig.7.1 Ang1 from PICDIF vs. Ang2 from PICCON  
(Ang inclined from horizontal).

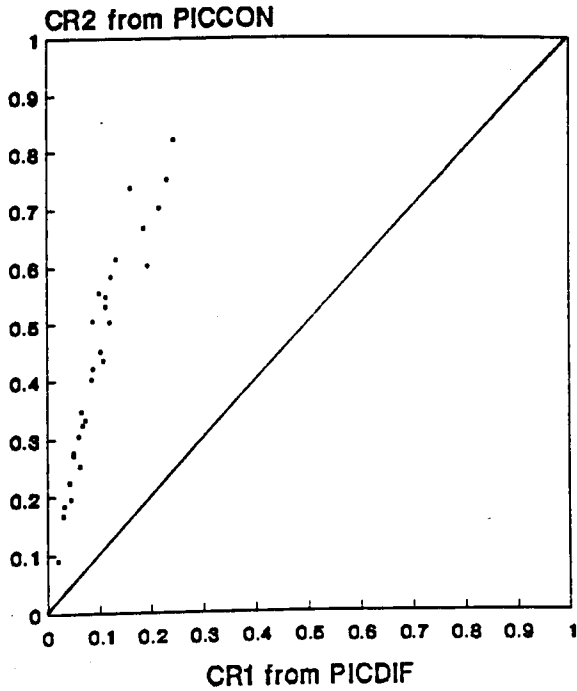


Fig.7.2 CR2 from PICCON vs. CR1 from PICDIF

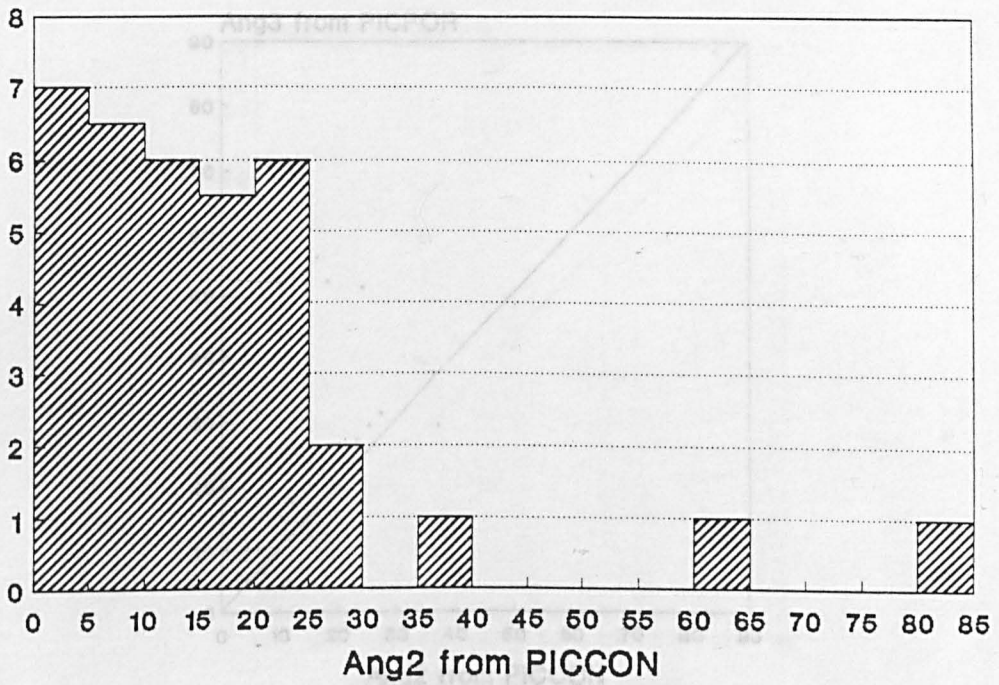


Fig.7.3 Histogram of Ang2 from PICCON.

(Ang inclined from horizontal).

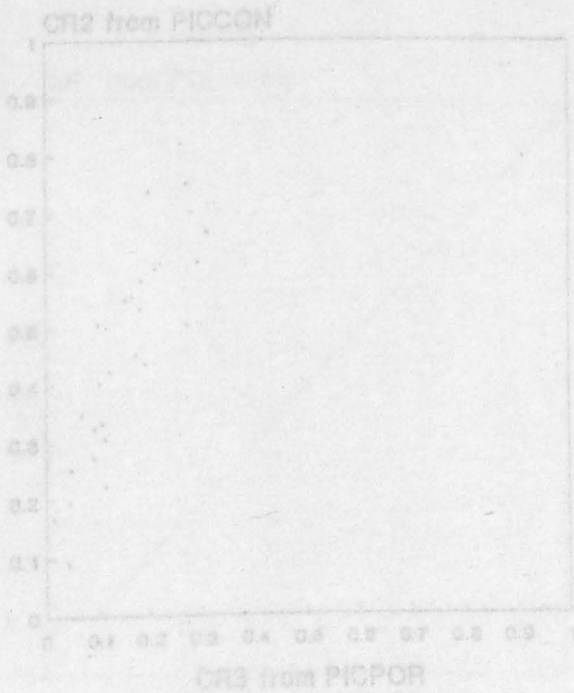


Fig.7.5 CR2 from PICCON vs. CR3 from PICPOR

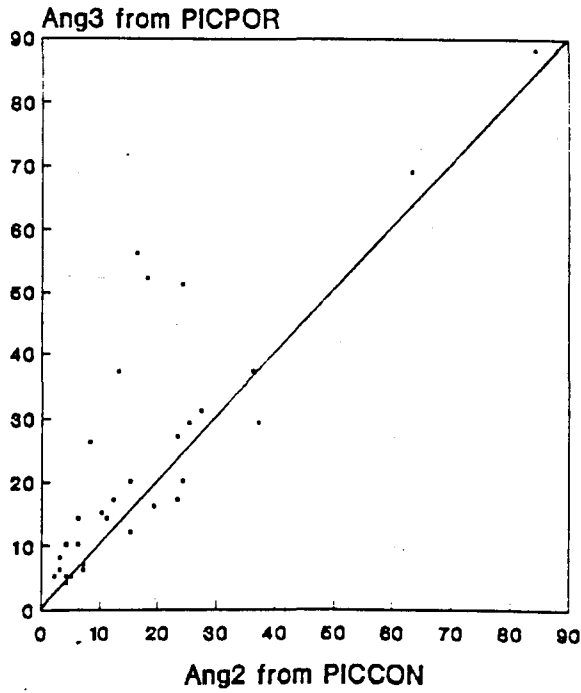


Fig.7.4 Ang3 from PICPOR vs. Ang2 from PICCON  
(Ang inclined from horizontal).

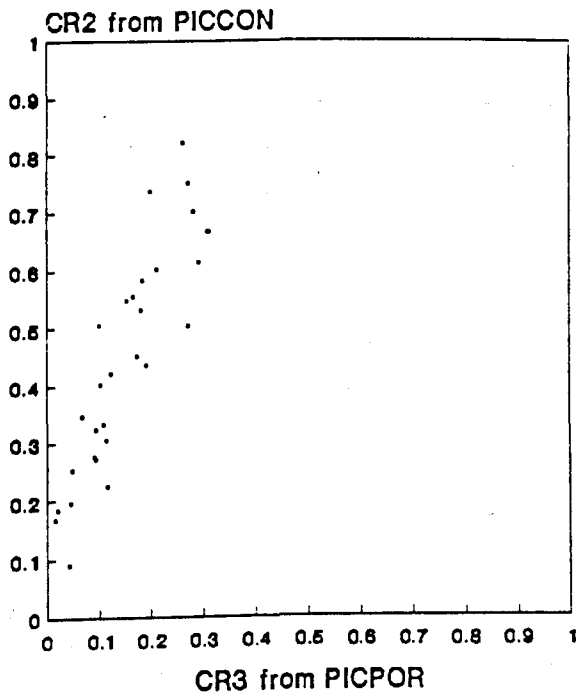


Fig.7.5 CR2 from PICCON vs. CR3 from PICPOR

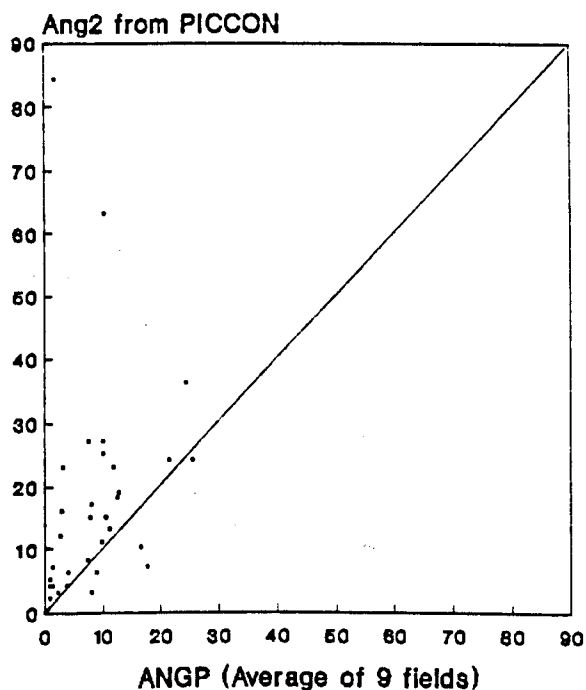


Fig.7.6 Ang2 from PICCON vs. ANGP

(Ang2 and ANGP inclined from horizontal, ANGP from the average of 9 optical microscopy fields)).

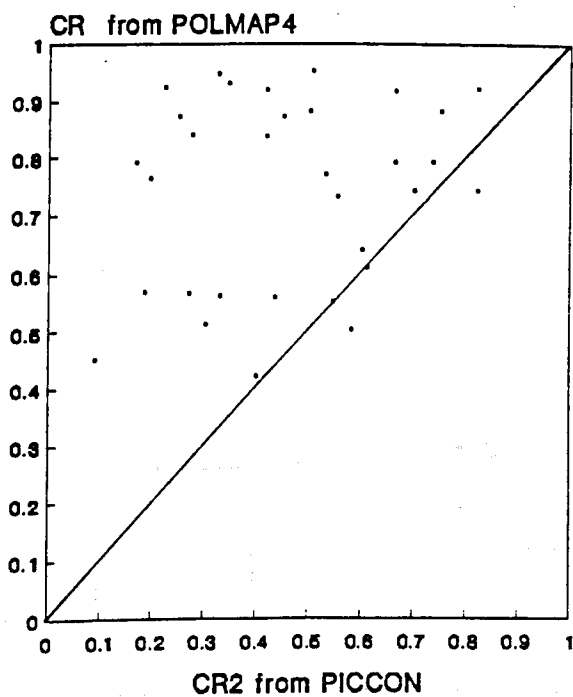


Fig.7.7 CR from POLMAP4 vs. CR2 from PICCON

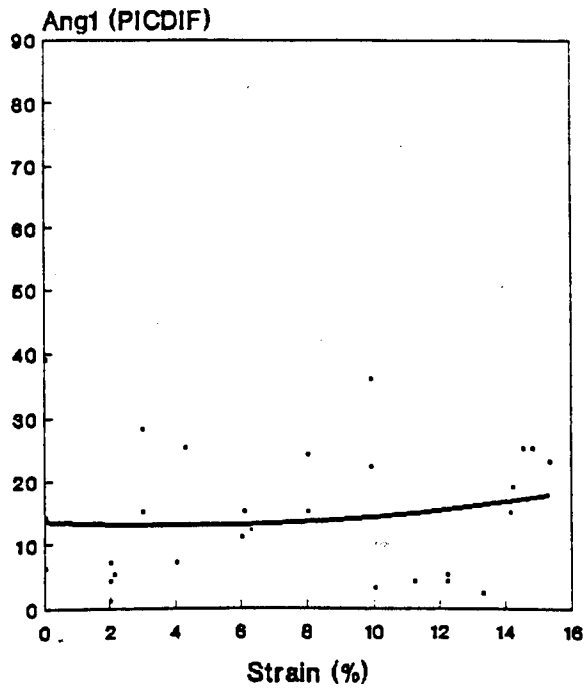


Fig.7.8.a Ang1 from PICDIF vs. Strain.

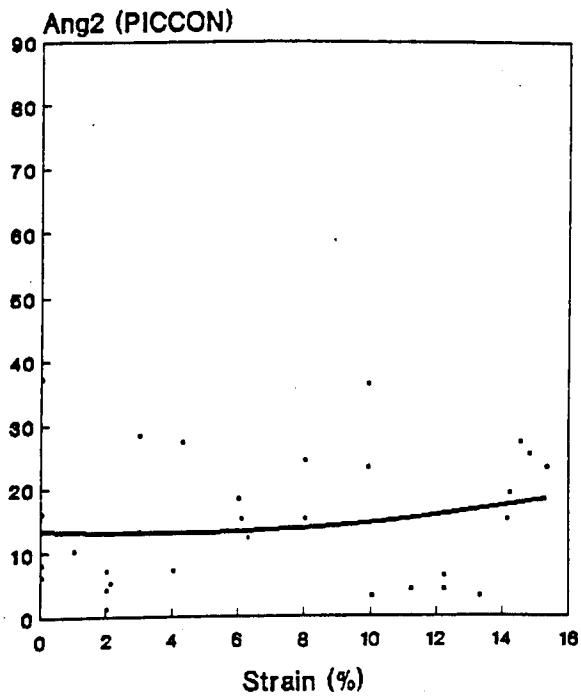


Fig.7.8.b Ang2 from PICCON vs. Strain

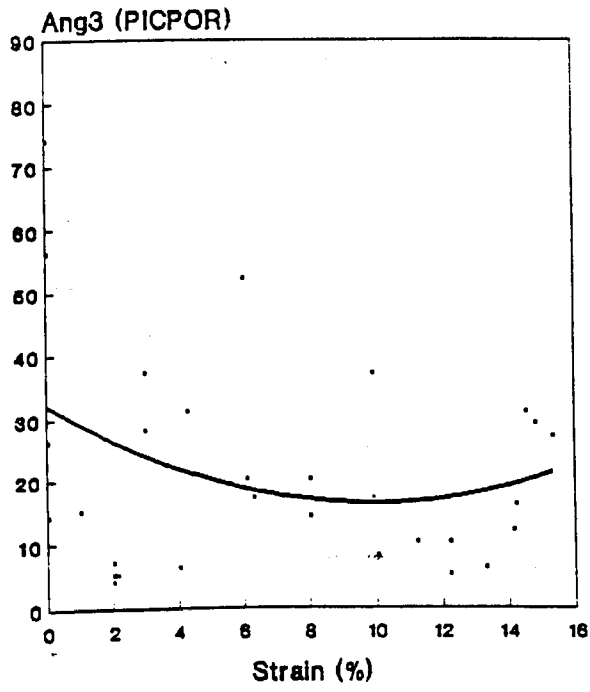


Fig.7.8.c Ang3 from PICPOR vs. Strain

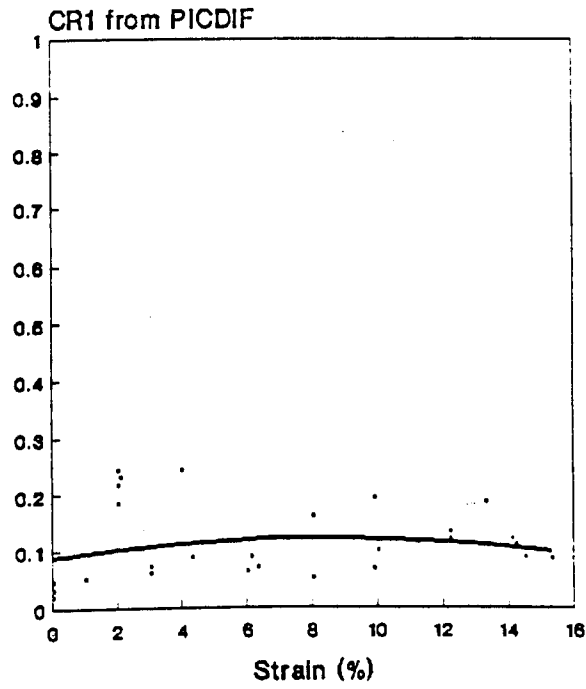


Fig.7.9.a CR1 from PICDIF vs. Strain.

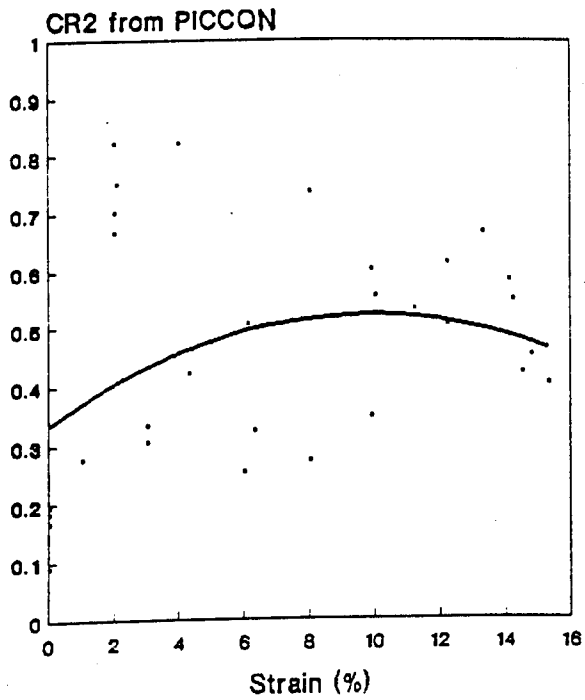


Fig.7.9.b CR2 from PICCON vs. Strain

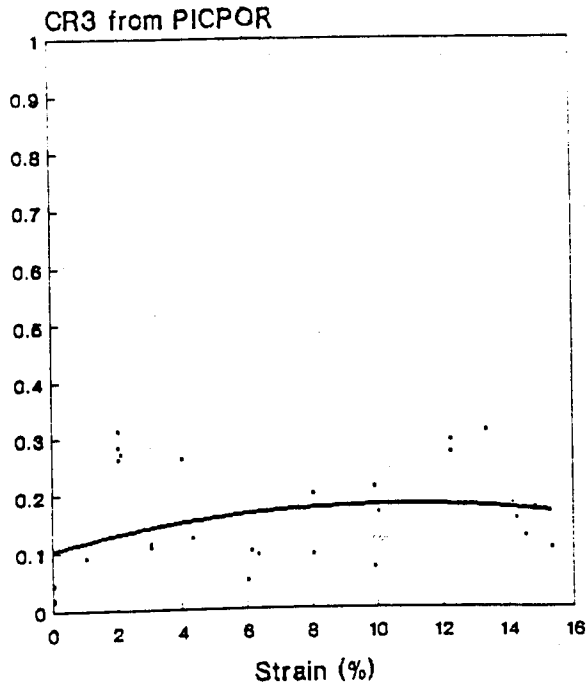


Fig.7.9.c CR3 from PICPOR vs. Strain

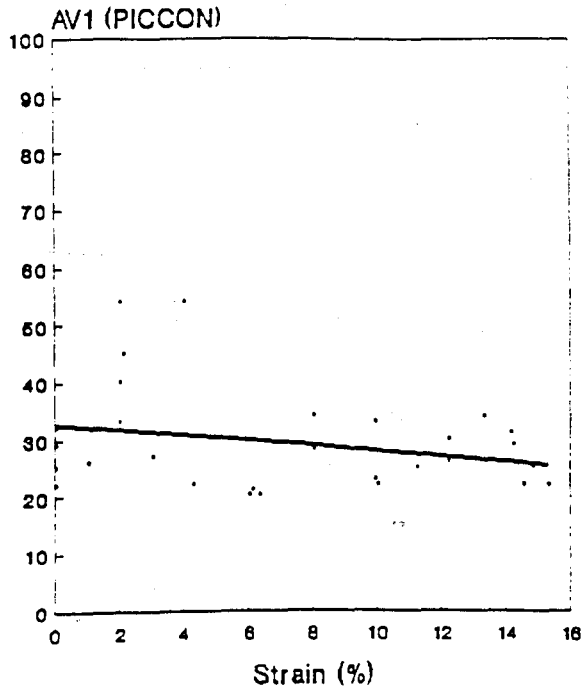


Fig.7.10.a Average Chord Sizes, AV1, from PICCON vs. Strain.

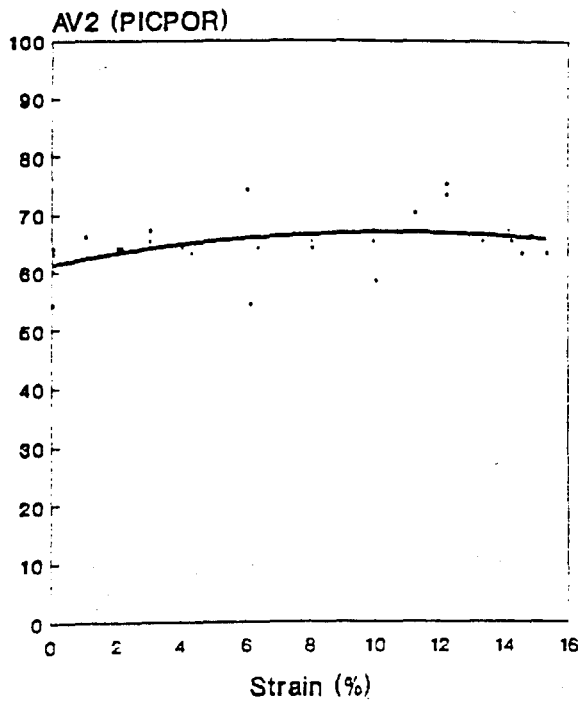


Fig.7.10.b Average Chord Sizes, AV2 from PICPOR vs. Strain

## Chapter Eight

### CONCLUSIONS AND RECOMMENDATIONS

#### 8.1 Conclusions

From the observations recorded in the previous chapters, some hypotheses have been proposed. This chapter will review and compare all the observations together. Some conclusions will be drawn and are given below, listed in the order in which they were established during the course of the experimental work and not necessarily in the order of importance.

##### 8.1.1 Stress-Strain Behaviour

The stress-strain curves of normally consolidated undrained triaxial shear (Fig.2.4) showed that, when the strain is about 10 % the stress achieves a peak value. Before the peak value, the stress-strain curves for replicate samples agreed with each other within 5 % stress at any strain. After the peak value, the stress falls, this fall being sometimes rapid, sometimes slow, and sometimes very slight.

##### 8.1.2 Sample Preparation

The techniques of sample preparation for both optical microscopy and electron microscopy which were adopted here presented satisfactory results. Substitution of the pore water by a mixture of acetone and water (details in Chapter 3) minimised the effect of this substitution on the structure, although there did seem to be some shrinkage. Impregnation with Vestopal W produced a

completely impregnated sample which had enough strength for further treatment (Chapter 3). It was very important that the water in the pores of the sample was completely replaced by acetone before impregnation, because the water would have stopped the resin from hardening. Some clean sand was placed around the sample to restrain it during substitution and impregnation. When grinding and polishing, care was paid to keeping the sample clean and to avoiding disrupting the surface of the sample.

### 8.1.3 Optical Microscopy

In this thesis, three new methods of optical microscopy, POLMAP, POLMAP3 and POLMAP4, were developed. These new methods provide more information than the older methods, and the maps given by the computer provide a more readily perceived image than did the original images.

The comparison of the Anisotropy Index with the Consistency Ratio (Fig.4.8) showed (1) that the Consistency Ratio is more sensitive to the degree of anisotropy than is the Anisotropy Index, and (2) that the Anisotropy Index depends not only on the 'strength' of anisotropy but also on the 'type' of anisotropy. It is therefore suggested that the Consistency Ratio is a more reasonable parameter for measuring the degree of anisotropy.

The new methods presented here are quick and easy to perform. These methods extend the older microphotometric analysis to provide fuller information on the orientation distribution together with the sizes and shapes of the mapped patches.

#### 8.1.4 Observation of Shear Deformation

Since all of the observations show some scatter, the following results are taken from the quadratic regressions, which were generally in agreement with each other (Figs.6.7 to 6.13, and 7.8 to 7.10). The results for undrained normally consolidated shear will be discussed first, followed by the results for the other two cases.

##### i. Normally Consolidated Undrained Shear

The results for preferred orientation from all the techniques used for the undrained normally consolidated shear series were close to the horizontal (Figs.6.7 - 8, and 7.8 - 7.9). These observations eliminate the hypothesis that domains turn into a preferred direction parallel to the failure plane.

All the quadratic regressions for the deviation of preferred orientation from the horizontal were concave upwards, see the same Figures as above. Although the trend was small, it is consistent with the hypothesis that the particles or domains tend to bed down into the horizontal during the early stages of shear deformation, and then they tend to be disrupted slightly during the later stages.

The results for the strength of anisotropy obtained from all the techniques used showed the same trend: *i.e.* the strength of anisotropy increased at low strain, then achieved a peak value, and finally decreased, as strain increased (Figs.6.9 and 7.9). This is consistent with the hypothesis of early bedding down and later disruption suggested above.

The results for the chord sizes of the mapped areas obtained from all the

techniques indicated that the chord sizes all remained substantially constant whilst deformation proceeded. These observations eliminated both the hypothesis that domains grow in size and the hypothesis that large domains are broken into a greater number of smaller domains.

The increase of the between-samples standard deviations shown in Figures 6.12 and 6.13 suggests that, post-peak, different samples are deforming in different ways, *i.e.* some form of structural instability is present. This interpretation is supported by the stress-strain behaviour summarised in Fig.2.4 and the appearance of large patches in some of the samples, cf. Fig.6.10.

A preliminary comparisons of maps from PICCON and PICPOR suggested that the dense areas in the samples consisted of large single domains whilst the less dense areas consisted of aggregations of small domains (see Section 7.3.1).

The quadratic trend for the deviation of the preferred orientation from the horizontal for the smoothed density field given by PICPOR was slightly more pronounced than the corresponding result from the smoothed orientation field given by PICCON (Figs.7.10.a and b). This was unexpected and is difficult to interpret. The quadratic regression from the chord sizes for the maps from PICPOR was very slightly concave downwards. It might perhaps be that some small domains were plastered onto larger ones during the early stages of shear and ripped off again during the later stages.

## ii. *Normally Consolidated Drained Shear*

The following conclusions for the drained normally consolidated shear series are based on optical microscopy, because the final results from electron

microscopy, which are being analysed elsewhere, are not yet available.

The results for the deviation of preferred orientation from the horizontal (Fig.6.16) were close to the horizontal, again eliminating the hypothesis that domains turn into a preferred direction parallel to the failure plane. The modulus of the average of the microphotometer results shown in Fig.6.16 should be compared with the results in Fig.6.7.a. Judged by the quadratic regression, the results for the drained samples decreased slightly as deformation increased, the rate of decrease being greater during the early stages of deformation. This pattern of behaviour is similar to that for the lateral strain deduced from Fig.2.6. The lateral strain was almost constant during the early stages of deformation and became more negative during the later stages as the samples expanded laterally.

In the drained series, the strength of anisotropy (Fig.6.15) increased at low strain, then achieved a peak value, and finally decreased, as strain increased, as did the results for the undrained series.

The chord sizes obtained from POLMAP appeared to increase with strain, the quadratic regression being concave upwards. These results differ from those for the undrained case, and it will be interesting to see how the results from electron microscopy compare. Judged visually, the standard deviation of the results in Fig.6.17 are moderately high at zero strain, lower at about 2% strain, and higher again in the mid-strain range; but there seem to be insufficient samples at high strain to make a calculation worthwhile before seeing the results from electron microscopy.

Tentatively, the overall behaviour of the drained series is somewhat similar to the undrained series, the particles appearing to bed down during the early

stages of deformation and to spread laterally during the later stages.

### iii. *Over-consolidated Drained Shear*

To provide a comparison, the conclusions from the incomplete set of thin sections for the drained over-consolidated shear series are summarised below. Again, the results from electron microscopy are expected to become available later. The trends are taken from both the quadratic regressions and the summary in Table 6.5, the differences being attributed to the smallness of the series.

This series of samples failed at about 6% strain which was much sooner than for the other series, which did not even reach the peak strains 10% or 8% strain.

The results for the deviation of preferred orientation from the horizontal (Fig.6.19) were close to the horizontal, again eliminating the hypothesis that domains turn into a preferred direction parallel to the failure plane. The deviation from the horizontal appear to have decreased slightly throughout the whole test.

The strength of anisotropy appears to have increased slightly during the tests (Figs.6.18.a and b). A precise analysis is difficult, because the microphotometer results increased during the later stages, whereas the POLMAP results increased during the early stages.

The chord sizes appear to have increased (perhaps only during the early stages of deformation) (Fig.6.20).

These samples appear to be bedding down until failure occurs abruptly.

### 8.1.5 Observations of Failure Planes

The measurements across failure planes using optical microscopy presented in Chapter 6 suggested that in the failure zone, the particles tend to incline in the direction of the failure plane. However, no changes were noticed in the patches and domains nearby, suggesting that these failure planes were local phenomena.

## 8.2 Recommendations

Some recommendations arising from the present research are listed in the following.

1. It is suggested that a new computer program should be written to compare the orientation maps from PICCON with the corresponding density maps from PICPOR.

2. Because of the variability within samples, it might be suggested that large numbers of fields in each sample, for both optical microscopy and electron microscopy, should be taken for the analysis. In future, it might be possible to take these observations in fully-automatic microscopes.

3. In future work, greater attention should be paid to three-dimensional effects than was possible here, although this will probably require further improvements in the techniques of preparation for electron microscopy.

4. In future electron microscopy, the conditions controlling contrast,

brightness, and the point spread function, should be standardised. This will be more convenient for that image analysis which has been planned in advance, and may make it easier to establish new unforeseen methods of analysis.

5. Mathematical models of the structure of soil, such as those which are now being based on inter-particle mechanics, should be capable of predicting a 'quadratic' response of the structure to increased strain.

6. These models should also take into account the possibility of structural instability, of which there may be several different types.

## Appendix A

### MECHANICAL TESTING PROCEDURE

#### FOR NORMALLY AND OVER-CONSOLIDATED DRAINED SHEAR SERIES (UEA TEST)

##### A.1 Normally Consolidated Drained Shear Test

###### A.1.1 Sample Preparation

Speswhite kaolinite was used in normally consolidated drained shear testing. The dry kaolinite powder is first mixed with distilled water at a moisture content approximately twice the liquid limit (about 70%). The slurry is mixed thoroughly until its texture has a smooth consistency with no lumps. Then, it is transferred to a low vacuum module, and shaken vigorously to remove all traces of trapped air. After mixing, the slurry is transferred to the filter presses.

The slurry is drained from both the top and bottom through porous stones and a laboratory grade filter paper membrane. The pressure applied to the piston is progressively increased over some days. The pressure is doubled daily up to 700 kPa.

This period lasts 14 days.

###### A.1.2 Triaxial Test

When consolidation in the filter press finishes, *i.e.* there is no further water extrusion, the filter cake is ready to be prepared into a sample for the three

dimensional triaxial consolidation.

The sample for the triaxial test is cut from the filter cake, being 38 mm diameter and 77 mm length.

In the triaxial apparatus, the water in the sample is drained from the top cap of the sample and pore pressure is measured from the bottom. The maximum consolidation pressure is 700 kPa, the same as the filter consolidation pressure. Again, the pressure is progressively increased, the increments are 200 kPa for the first two steps, and 300 kPa for the last step, this taking 6 days.

After three dimensional consolidation, the samples are tested in drained shear with a strain rate sufficient to complete the test in 4 days at a cell pressure of 700 kPa. During shearing, the axial load, axial deformation, volumetric deformation, and pore pressure are measured. Therefore, the stress-strain curve and volume change-strain curve can be plotted.

#### A.2 Over-Consolidated Drained Shear

For this series, the initial preparation of sample and  $K_0$  consolidation to 700 kPa follow the pattern used in normally consolidated drained shear series. The triaxial consolidation is also up to 700 kPa, but the drained shear is at a constant cell pressure of 100 kPa. These over-consolidated tests are not yet complete.

## Appendix B

## THE THEORY OF OPTICAL MICROSCOPY

This section considers the passage of a parallel beam of monochromatic light through a polarizer, a thin section, a plate ( $\lambda/4$ ,  $\lambda/2$ , or  $\lambda$ ), and an analyser. The polars (polarizer and analyser) are assumed to be crossed.

B.1 Without Plate

The light leaving the polarizer is plane-polarized and is represented by an oscillating vector drawn perpendicular to the ray, along the axes of polarizer Op. The amplitude is supposed to be unity, so it may be written (Hecht and Zajac, 1976):

$$p = \sin \omega t.$$

Let the section axes be Oe and Oo, and  $\angle pOe = \theta$  (Fig.B.1). Then, the light leaving the polarizer and entering the thin section is:

$$\begin{cases} e = p \cos \theta = \cos \theta \sin \omega t \\ o = p \sin \theta = \sin \theta \sin \omega t. \end{cases}$$

When the light passes through the thin section, a phase difference,  $\delta$ , occurs. The light leaving the thin section is:

$$\begin{cases} e = \cos \theta \sin \omega t \\ o = \sin \theta \sin (\omega t - \delta) \end{cases} \quad (\text{B.1}),$$

where the time origin has been changed by the phase shift for the extraordinary ray, and, similar changes assumed below where convenient.

Let the axes of the analyser be Oa,  $\angle pOa = \pi/2$  (shown in Fig.B.1). The analyser passes only the a-component of the light entering it, i.e.:

$$\begin{aligned} a &= e \cos (\pi/2 - \theta) - o \sin (\pi/2 - \theta) \\ &= \cos \theta \sin \theta \sin \omega t - \cos \theta \sin \theta \sin (\omega t - \delta) \\ &= \sin \omega t [\sin \theta \cos \theta (1 - \cos \delta)] + \\ &\quad \cos \omega t \sin \delta \sin \theta \cos \theta. \end{aligned}$$

$$\begin{aligned} [\text{rms } (a)]^2 &= 0.5 \{[\sin \theta \cos \theta (1 - \cos \delta)]^2 + \\ &\quad (\sin \delta \sin \theta \cos \theta)^2\} \\ &= 0.5 \sin^2 2\theta \sin^2 (\delta/2). \end{aligned}$$

So,

$$I = [\text{rms } (a)]^2 = 0.5 \sin^2 2\theta \sin^2 (\delta/2) \quad (\text{B.2}),$$

where,  $I$  = relative intensity, i.e. ratio of transmitted intensity to incident intensity: 'non-dimensional'.

$$[\text{rms } (a)] = 0, \text{ only if } \sin 2\theta = 0 \text{ or } \sin (\delta/2) = 0.$$

$$\text{So, } \theta = n\pi/2 \quad (n = 0, 1, 2, 3, \dots),$$

$$\text{or } \delta = 2k\pi \quad (k = 0, 1, 2, 3, \dots).$$

Thus, extinction occurs only when the section axes are parallel to or perpendicular to the axes of polars, or, in an inconvenient case, the thickness of the thin section is  $k\lambda/\Delta n$ .

$$\text{Here, } k = 0, 1, 2, \dots,$$

$$\lambda = \text{the wave length of light,}$$

$$\Delta n = n_a - n_b.$$

## B.2 With a Quarter-Wave Plate

As mentioned above, the light leaving the thin section is represented by Equation (B.2). Suppose the quarter-wave plate is in the position which lets the axes of the quarter-wave plate be  $xOy$ ,  $\angle pOx = \pi/4$  (see Fig.B.2). The light entering the quarter-wave plate is:

$$\begin{cases} x = \cos(\pi/4 - \theta)\cos\theta \sin\omega t - \sin(\pi/4 - \theta)\sin\theta \sin(\omega t - \delta) \\ y = \sin(\pi/4 - \theta)\cos\theta \sin\omega t + \cos(\pi/4 - \theta)\sin\theta \sin(\omega t - \delta). \end{cases}$$

When the light passess through the plate, a phase difference,  $\pi/2$ , occurs. In the case assumed the fast direction of the thin section is parallel to the slow direction of the quarter-wave plate, the light leaving the quarter-wave plate is:

$$\begin{cases} x = \cos(\pi/4 - \theta)\cos\theta \sin(\omega t - \pi/2) - \\ \quad \sin(\pi/4 - \theta)\sin\theta \sin(\omega t - \delta - \pi/2) \\ y = \sin(\pi/4 - \theta)\cos\theta \sin\omega t + \\ \quad \cos(\pi/4 - \theta)\sin\theta \sin(\omega t - \delta). \end{cases}$$

Let the axes of the analyser be  $Oa$ ,  $\angle pOa = \pi/2$ . Only the  $a$ -component of the light entering the analyser is passed, i.e.:

$$\begin{aligned} a &= x \cos \pi/4 - y \sin \pi/4 \\ &= 1/\sqrt{2} \{ [\sin\theta \sin(\pi/4 - \theta) \cos\delta - \cos\theta \cos(\pi/4 - \theta) + \\ &\quad \sin\theta \cos(\pi/4 - \theta) \sin\delta] \sin\omega t + \\ &\quad [\sin\theta \sin(\pi/4 - \theta) \sin\delta - \cos\theta \sin(\pi/4 - \theta) - \\ &\quad \sin\theta \cos(\pi/4 - \theta) \cos\delta] \cos\omega t \}, \\ [\text{rms}(a)]^2 &= 0.5 (1 - \sin 2\theta \sin\delta). \end{aligned}$$

So,

$$\begin{aligned} I &= [\text{rms}(a)]^2 \\ &= 0.5 (1 - \sin 2\theta \sin\delta) \end{aligned} \tag{B.3}.$$

[rms (a)] is zero only when

$$\sin 2\theta \sin \delta = 1.$$

It is only possible when

$$\begin{cases} \theta = (4n+1)\pi/4 \\ \delta = (4k+1)\pi/2, \end{cases}$$

or,

$$\begin{cases} \theta = (4n+3)\pi/4 \\ \delta = (4k+3)\pi/2, \end{cases}$$

where n and k are integers.

Thus, extinction occurs only when both: the section axes are  $\pi/4$  to polars and  $\delta$  is  $\pi/2$  in the case with the quarter-wave plate.

### B.3 With a Half-Wave Plate

Similarly to the case with a quarter-wave plate, the light entering the half-wave plate is determined by Equation B.3, and a phase shift,  $\pi$ , is introduced when the light passes the half-wave plate. The light leaving the half-wave plate is as follows with the same assumption as the quarter-wave plate:

$$\begin{cases} x = \cos(\pi/4 - \theta) \cos \theta \sin(\omega t - \pi) - \\ \quad \sin(\pi/4 - \theta) \sin \theta \sin(\pi t - \delta - \pi) \\ y = \sin(\pi/4 - \theta) \cos \theta \sin \omega t + \\ \quad \cos(\pi/4 - \theta) \sin \theta \sin(\omega t - \delta). \end{cases}$$

The light passing through the analyser is only the a-component of the light which is determined by the following equation:

$$a = x \cos \pi/4 - y \sin \pi/4$$

$$= - (\cos^2 \theta + \sin^2 \theta \cos \delta) \sin \omega t + \sin^2 \theta \sin \delta \cos \omega t,$$

$$[\text{rms } (a)]^2 = 0.5 [(\cos^2 \theta + \sin^2 \theta \cos \delta)^2 + (\sin^2 \theta \sin \delta)^2] \\ = 0.5 [\cos^4 \theta + \sin^4 \theta + 2.0 \sin^2 \theta \cos^2 \theta \cos \delta].$$

$$\text{So, } I = [\text{rms } (a)]^2 \\ = 0.5 [\cos^4 \theta + \sin^4 \theta + 2 \sin^2 \theta \cos^2 \theta \cos \delta] \quad (\text{B.4}).$$

[rms (a)] is zero only when both:

$$\theta = (2n + 1)\pi/4,$$

$$\text{and } \delta = \cos^{-1} -1 = (2k + 1)\pi,$$

where n and k are integers.

Thus, extinction occurs only when both of the following conditions exist: the section axes bisect the axes of the polars ( $45^\circ$ -position), and  $\delta = (2k + 1)\pi$ .

#### B.4 With a Whole-Wave Plate

In this case, as in the above, a phase shift,  $2\pi$ , is introduced when the light passes through the whole-wave plate. The light leaving the whole-wave plate is:

$$\left\{ \begin{array}{l} x = \cos (\pi/4 - \theta) \cos \theta \sin (\omega t - 2\pi) - \\ \quad \sin (\pi/4 - \theta) \sin \theta \sin (\pi t - \delta - 2\pi) \\ y = \sin (\pi/4 - \theta) \cos \theta \sin \omega t + \\ \quad \cos (\pi/4 - \theta) \sin \theta \sin (\omega t - \delta). \end{array} \right.$$

The light passing through the analyser is only the a-component of the light

which is determined by the following equation:

$$\begin{aligned}
 a &= x \cos \pi/4 - y \sin \pi/4 \\
 &= \sin \delta \cos \theta (1 - \cos \delta) \sin \omega t + \sin \theta \cos \theta \sin \delta \cos \omega t, \\
 [\text{rms } (a)]^2 &= 0.5 [\sin^2 \theta \cos^2 \theta (1 - \cos \delta) + \\
 &\quad \sin^2 \theta \cos^2 \theta \sin^2 \delta] \\
 &= 0.5 (1 - \sin^2 2\theta \sin^2 \delta), \tag{B.5}
 \end{aligned}$$

So,  $I = [\text{rms } (a)] = 0$ , only if  $\sin^2 2\theta \sin^2 \delta = 1$ .

Therefore,

$$\theta = (2n + 1)\pi/4 \quad (n = 0, 1, 2, 3, \dots),$$

$$\text{and } \delta = (2k + 1)\pi/2 \quad (k = 0, 1, 2, 3, \dots).$$

Thus, the extinction occurs in the same conditions as with a half-wave plate, that is the section axes bisect the axes of the polars ( $45^\circ$ -position), and  $\delta = (2k + 1)\pi/2$ .

## B.5 Two Special Methods of Analysis

### B.5.1 Method One: POLMAP4

When a parallel beam of monochromatic light passes through a polarizer, a thin section, a quarter-wave plate, and an analyser which is crossed with the polarizer, as mentioned above, the intensity ( $I$ ) of the light is as follows:

$$I = 0.5 (1 - \sin 2\theta \sin \delta) \tag{B.3}$$

In this case, suppose the thin section is set at  $0^\circ$  with the polarizer:

$$I_0 = 0.5 (1 - \sin 2\theta \sin \delta) \tag{B.3a}$$

Then turn the polars to  $45^\circ$ , the intensity of the light through the thin section is:

$$\begin{aligned} I_{45} &= [1 - \sin 2(\theta + 45) \sin \delta] \\ &= (1 - \cos 2\theta \sin \delta) \end{aligned} \quad (\text{B.3b}).$$

Then, turn the polars  $90^\circ$ , the intensity is:

$$\begin{aligned} I_{90} &= [1 - \sin 2(\theta + 90) \sin \delta] \\ &= (1 + \sin 2\theta \sin \delta) \end{aligned} \quad (\text{B.3c}).$$

Also, the following equation can be obtained:

$$I_{135} = (1 + \cos 2\theta \sin \delta) \quad (\text{B.3d}).$$

Therefore,

$$\text{tg } 2\theta = \frac{I_{90} - I_0}{I_{135} - I_{45}} \quad (\text{B.6a}),$$

$$\sin \delta = [(I_{90} - I_0)^2 + (I_{135} - I_{45})^2]^{1/2} \quad (\text{B.7a}),$$

$$\text{SUM} = \frac{(I_{90} + I_{45} + I_{90} + I_{135})}{4} = 1/2 \quad (\text{B.8a}).$$

### B.5.2 POLMAP3

In the same way as mentioned above, the following equations can be calculated:

$$I_0 = 0.5 (1 - \sin 2\theta \sin \delta) \quad (\text{B.3a}),$$

$$\begin{aligned} I_{120} &= 0.5 [1 - \sin 2(\theta + 120) \sin \delta] \\ &= 0.25[2 + (\sin 2\theta + \sqrt{3} \cos 2\theta) \sin \delta] \end{aligned} \quad (\text{B.3b'}),$$

$$\begin{aligned} I_{240} &= 0.5 [1 - \sin 2(\theta + 240) \sin \delta] \\ &= 0.25[2 + (\sin 2\theta - \sqrt{3} \cos 2\theta) \sin \delta] \end{aligned} \quad (\text{B.3c}'),$$

$$\begin{aligned} I_{180} &= 0.5 [1 - \sin 2(\theta + 180) \sin \delta] \\ &= 0.25[2 + (\sin 2\theta + \sqrt{3} \cos 2\theta) \sin \delta] \end{aligned} \quad (\text{B.3b}'''),$$

$$\begin{aligned} I_{60} &= 0.5 [1 - \sin 2(\theta + 60) \sin \delta] \\ &= 0.25[2 + (\sin 2\theta - \sqrt{3} \cos 2\theta) \sin \delta] \end{aligned} \quad (\text{B.3c2}),$$

$$\text{So, } \sin 2\theta \sin \delta = 2/3 (I_{120} + I_{240} - 2I_0) = 2/3 (I_{180} + I_{60} - I_0),$$

$$\cos 2\theta \sin \delta = 2/\sqrt{3}(I_{120} - I_{240}) = 2/\sqrt{3} (I_{180} - I_{60}).$$

Therefore,

$$\text{tg } 2\theta = \frac{I_{120} + I_{240} - 2I_0}{\sqrt{3} (I_{120} - I_{240})} \quad (\text{B.6b}),$$

$$\sin \delta = 2/3 \{ (I_{120} + I_{240} - 2I_0)^2 + [\sqrt{3} (I_{120} - I_{240})]^2 \}^{1/2} \quad (\text{B.7b}),$$

$$\text{Sum} = \frac{I_0 + I_{120} + I_{240}}{3} = 1/2 \quad (\text{B.8b}),$$

or,

$$\text{tg } 2\theta = \frac{I_{180} + I_{60} - 2I_0}{\sqrt{3} (I_{180} - I_{60})} \quad (\text{B.6c}),$$

$$\sin \delta = 2/3 \{ (I_{180} + I_{60} - 2I_0)^2 + [\sqrt{3} (I_{180} - I_{60})]^2 \}^{1/2} \quad (\text{B.7c}),$$

$$\text{Sum} = \frac{I_0 + I_{180} + I_{60}}{3} = 1/2 \quad (\text{B.8c}).$$

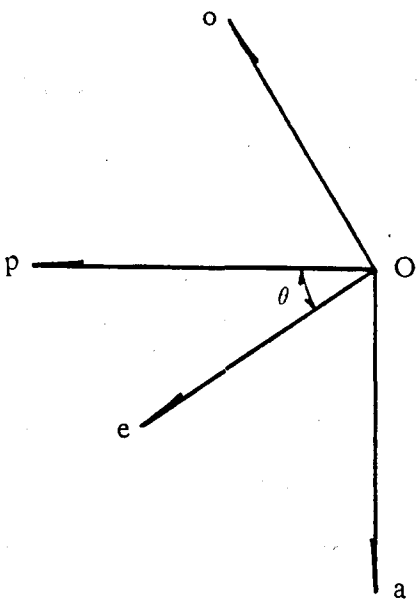


Fig.B.1

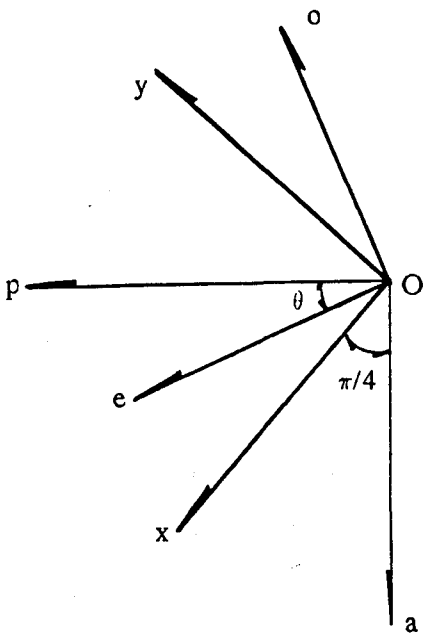


Fig.B.2

## Appendix C

## COMPARISON OF ANISOTROPY INDICES AND CONSISTENCY RATIO

C.1 Introduction

When the distribution of the number of pixels inclined at angle  $\theta$  is known, the formula for Anisotropy Indices A1 in PMPA and A2 in POLMAP and for the Consistency Ratio CR in POLMAP4 and POLMAP3 can be obtained. According to the experimental results, an approximate distribution is suggested as follows:

$$f = \begin{cases} a + b \cos 2\theta & 0 \leq \theta \leq \pi/4 \\ a & \pi/4 \leq \theta \leq 3\pi/4 \\ a + b \cos 2\theta & 3\pi/4 \leq \theta \leq \pi \end{cases} \quad (\text{C.1}).$$

Here, a and b are constants.

For a given distribution, the anisotropy Indices, A1 and A2, and the consistency Ratio, CR, are obtained below.

C.2 Anisotropy Index A1

It was shown in Appendix B that the intensity of the light leaving the analyser under crossed polars for one pixel is:

$$I = 0.5 \sin^2 2\theta \sin^2 \delta/2 \quad (\text{B.2}).$$

For the Anisotropy Index A1 in PMPA,

$$\text{Max} = \int_0^{\pi} 0.5 \sin^2 2(\theta - \pi/4) \sin^2 \delta/2 f d\theta,$$

$$\text{Min} = \int_0^{\pi} 0.5 \sin^2 2\theta \sin^2 \delta/2 f d\theta,$$

and,

$$A1 = \frac{\text{Max} - \text{Min}}{\text{Max} + \text{Min}} \quad (4.1).$$

Therefore,

$$\begin{aligned} \text{Max} &= \int_0^{\pi} 0.5 \sin^2 2(\theta - \pi/4) \sin^2 \delta/2 f d\theta, \\ &= \int_0^{\pi/4} 0.5 \sin^2 2(\theta - \pi/4) \sin^2 \delta/2 (a + b \cos 2\theta) d\theta + \\ &+ \int_0^{3\pi/4} 0.5 a \sin^2 2(\theta - \pi/4) \sin^2 \delta/2 d\theta + \\ &+ \int_{3\pi/4}^{\pi} 0.5 \sin^2 2(\theta - \pi/4) \sin^2 \delta/2 (a + b \cos 2\theta) d\theta, \\ \text{Min} &= \int_0^{\pi} 0.5 \sin^2 2\theta \sin^2 \delta/2 f d\theta, \\ &= \int_0^{\pi/4} 0.5 \sin^2 2\theta \sin^2 \delta/2 (a + b \cos 2\theta) d\theta + \end{aligned}$$

$$+ \int_{\pi/4}^{3\pi/4} 0.5 a \sin^2 2\theta \sin^2 \delta/2 d\theta +$$

$$+ \int_{3\pi/4}^{\pi} 0.5 \sin^2 2\theta \sin^2 \delta/2 (a + b \cos 2\theta) d\theta,$$

Suppose  $\delta$  is not a function of  $\theta$ , then  $0.5 \sin^2 \delta/2$  can be taken out from integral. Thus, the following conclusions can be obtained:

$$\text{Max} = 0.5 \sin^2 \delta/2 \left\{ \int_0^{\pi/4} \cos^2 2\theta (a + b \cos 2\theta) d\theta + \right.$$

$$\left. \int_{\pi/4}^{3\pi/4} \cos^2 2\theta a d\theta + \int_{3\pi/4}^{\pi} \cos^2 2\theta (a + b \cos 2\theta) d\theta \right\}$$

$$= 0.5 \sin^2 \delta/2 (a\pi/2 + 2b/3),$$

$$\text{Min} = 0.5 \sin^2 \delta/2 \left\{ \int_0^{\pi/4} \sin^2 2\theta (a + b \cos 2\theta) d\theta + \right.$$

$$\left. \int_{\pi/4}^{3\pi/4} \sin^2 2\theta a d\theta + \int_{3\pi/4}^{\pi} \sin^2 2\theta (a + b \cos 2\theta) d\theta \right\}$$

$$= 0.5 \sin^2 \delta/2 (a\pi/2 + b/3),$$

$$A1 = 1/3 \frac{b}{a\pi + b} \quad (C.2).$$

### C.3 Anisotropy Index A2

In POLMAP, the Anisotropy Index, A2, is described by Eq.4.3, *i.e.*

$$A2 = \frac{|(H + V) - (L + R)|}{H + V + L + R} \quad (4.3).$$

Here, H, V, L, and R are respectively the number of pixels mapped into direction: horizontal, vertical, down-left, and down-right, which come from comparison of three pairs of micrographs as mentioned in Chapter 4. The total number of pixels between  $\theta_1$  and  $\theta_2$  can be calculated by integrating  $f$  from  $\theta_1$  to  $\theta_2$ . Thus, the following results can be calculated in the same way:

$$H = \int_0^{\pi/8} f d\theta + \int_{7\pi/8}^{\pi} f d\theta = 0.25 a\pi + b \sin \pi/4,$$

$$V = \int_{3\pi/8}^{5\pi/8} f d\theta = 0.25 a\pi,$$

$$L = \int_{\pi/8}^{3\pi/8} f d\theta = 0.25 a\pi + b/2 (1 - \sin \pi/4),$$

$$R = \int_{5\pi/8}^{7\pi/8} f d\theta = 0.25 a\pi + b/2 (1 - \sin \pi/4),$$

$$A2 = (\sqrt{2} - 1) \frac{b}{a\pi + b} \quad (C.3).$$

#### C.4 Consistency Ratio CR

Following the definition of Consistency Ratio in Chapter 4,

$$CR = [(S_X^2 + S_Y^2)]^{1/2} / S \quad (4.3a).$$

$$\bar{\theta} = 0.5 \operatorname{tg}^{-1} (S_Y/S_X) \quad (4.3b).$$

And, in this case,

$$S_X = \int_0^{\pi} f \cos 2\theta \, d\theta = 0.25 \, b\pi,$$

$$S_Y = \int_0^{\pi} f \sin 2\theta \, d\theta = 0,$$

$$S = \int_0^{\pi} f \, d\theta = a\pi + b.$$

So,

$$CR = 0.25\pi \frac{b}{a\pi + b} \quad (C.4),$$

$$\bar{\theta} = 0.5 \operatorname{tg}^{-1} 0/0.25\pi = 0^\circ \quad (C.4).$$

#### C.5 Conclusions

Comparing A1, A2, and CR described by Eqs. C.2, C.3, and C.4 respectively, CR is bigger than A2 which is bigger than A1.

Considering another distribution (following Leng) as:

$$g = h + k \cos 2\theta \quad (C.5),$$

where,  $h$  and  $k$  are constants, it can be obtained by the procedure mentioned above that  $A_1$ ,  $A_2$ , and  $CR$  are respectively 0, 0, and  $k/2h$ .

Therefore, Consistency Ratio is expected to be bigger than the Anisotropy Indices, and its value depends mainly on the 'strength' of anisotropy; but Anisotropy Indices  $A_1$  and  $A_2$  depend on the 'type' of anisotropy in addition to the 'strength' of anisotropy.

## Appendix D

## AN EXAMPLE OF OUTPUT FILE

Program PICRAT.

First file is /bailib/tape2/file117 Last file is 138

True porosity = 520 o/oo;      gsolid = 234;      gvoid = 35

Threshold grey level = 128;    highest = 255;    lowest = 64

Filter radius = 20

CHORD LENGTHS: pixels

file	caption	PICCON				PICPOR			
		h	v	av	v/h	h	v	av	v/h
117	Q372G28.IM	37	38	38	1.027	66	74	70	1.121
118	Q372G3.IM	38	41	40	1.079	69	82	76	1.188
119	Q372G219.IM	30	31	31	1.033	64	78	71	1.219
120	Q372G21.IM	31	29	30	0.935	73	63	68	0.863
121	Q372G25.IM	33	32	33	0.97	61	60	61	0.984
122	Q372G218.IM	33	33	33	1.0	65	75	70	1.154
123	Q372G220.IM	23	23	23	1.0	120	130	125	1.083
124	Q372G221.IM	39	41	40	1.051	52	64	58	1.231
125	Q372G223.IM	35	35	35	1.0	57	59	58	1.035
126	Q372G224.IM	35	35	35	1.0	52	58	55	1.115
127	Q372G225.IM	31	29	30	0.935	83	75	79	0.904
128	Q372G27.IM	26	24	25	0.923	65	68	67	1.046
129	Q372G29.IM	30	31	31	1.033	72	78	75	1.083
130	Q372G210.IM	21	22	22	1.048	93	99	96	1.065
131	Q372G211.IM	24	23	24	0.958	71	66	69	0.93
132	Q372G212.IM	30	30	30	1.0	68	69	69	1.015
133	Q372G213.IM	39	40	40	1.026	65	69	67	1.062
134	Q372G214.IM	44	46	45	1.045	75	82	79	1.093
135	Q372G215.IM	31	33	32	1.065	61	68	65	1.115
136	Q372G22.IM	31	29	30	0.935	73	63	68	0.863
137	Q372G216.IM	31	31	31	1.0	100	93	97	0.93
138	Q372G217.IM	33	33	33	1.0	60	71	66	1.183
	mean	32	32	32	1.0	71	75	73	1.056
	std dev	6	6	6	1.0	16	16	16	1.0

CONSISTENCY RATIOS o/oo  
 ANGLE degree from horizontal

file	caption	PICDIF		PICCON		PICPOR	
		rat	ang	rat	ang	rat	ang
117	Q372G28.IM	212	64	755	64	236	60
118	Q372G3.IM	179	85	653	85	303	89
119	Q372G219.IM	167	80	648	80	366	-83
120	Q372G21.IM	85	-16	315	-17	74	-40
121	Q372G25.IM	206	51	774	51	549	38
122	Q372G218.IM	155	51	605	51	232	50
123	Q372G220.IM	31	-71	198	-78	225	87
124	Q372G221.IM	211	78	722	78	538	83
125	Q372G223.IM	198	54	695	56	352	80
126	Q372G224.IM	170	57	665	57	272	58
127	Q372G225.IM	146	15	608	17	215	21
128	Q372G27.IM	117	61	553	63	314	-28
129	Q372G29.IM	150	-77	599	-78	196	-75
130	Q372G210.IM	44	89	212	-89	386	-78
131	Q372G211.IM	98	-37	482	-38	161	-5
132	Q372G212.IM	113	53	442	53	305	52
133	Q372G213.IM	215	63	675	63	222	86
134	Q372G214.IM	227	54	793	56	503	50
135	Q372G215.IM	216	65	781	65	416	62
136	Q372G22.IM	85	-16	315	-17	74	-40
137	Q372G216.IM	118	47	466	48	467	37
138	Q372G217.IM	197	73	720	73	436	79
	vector mean	105	63	434	63	188	69
	mean	152		576		311	
	std dev	58		182		137	
	av con rat			319			

## REFERENCES

- Aas, G., 1967, *Vane tests for investigation of anisotropy of undrained shear strength of clays*. Proceedings of the Geology Conference, Oslo, 1, pp. 3–8.
- Barden, L., 1972, *The influence of structure on deformation and failure in clay soil*. Geotechnique 22, pp. 159–163.
- Barden, L. & Sides, G. R., 1970, *Engineering behaviour and structure of compacted clay*. ASCE 96 SM4, pp. 1171–1200.
- Bates, T. F. & Comer, J. J., 1954, *Electron microscopy of clay surfaces*. Proceedings of 3rd Conference on Clays and Clay Minerals, Pergamon Press, pp. 1–25.
- Bennett, R. H., Bryant, W. R., & Hulbert, M. H., eds., 1990, *Microstructure of fabric-grained sediments, from mud to shale*. Springer, New York.
- Beutelspacher, H. & Van der Marel, H. W., 1968, *Atlas of electron microscopy of clay minerals and their admixtures*. Elsevier Publishing Company, Amsterdam.
- Bhasin, R. N., 1975, *Pore size distribution of compacted soils after critical region drying—executive summary of final report*. NTIS Accession No. PB245 427. National Technical Information Service, U.S. Dept. Commerce, Springfield, VA.
- Bhatia, S. K. & Soliman, A., 1990, *The application of image analysis techniques*

- to *microstructural studies in geotechnical engineering*. Microstructure of Fabric-Grained sediments — from Mud to Shale, Bennett, R. H. et al. eds. pp.367–378.
- Bjerrum, L., 1972, *Embankments on soft ground*. Proceedings of the Special Conference on Performance of Earth and Earth Supported Structures, ASCE 2, pp. 1–54.
- Borst, R. L. & Keller, W. D., 1969, *Scanning electron micrographs of API reference clay minerals and other selected samples*. Proceedings of 3th International Clay Conference, 1, pp. 871–901.
- Bowles, F. A., 1968, *Microstructure of sediments: investigation with ultrathin sections*. Science, 159, pp. 1236–1237.
- Buessem, W. R. & Nagy, B., 1953, *The mechanism of the deformation of clay*. Proceedings of 2nd Conference on Clays and Clay Minerals. pp. 480–491.
- Chilingar, G. V. & Knight, L., 1960, *Relationship between pressure and moisture content of kaolinite, illite, and montmorillonite clays*. Bulletin of the American Association of Petroleum Geologists, 44, pp. 101–106.
- Chiou, W. A., Bryant, W. R. & Benett, R. H., 1990, *Quantification of clay fabric, a simple technique*. Microstructure of Fine-Grained Sediments — from Mud to Shale, Bennett, R. H. et al. eds. pp.379–387.
- Collins, K., & McGown, A., 1974, *The form and function of microfabric features in a variety of natural soils*. Geotechnique, 24, pp. 223–254

- Curry, J. R., 1956, *The analysis of two-dimensional orientation data*. Journal of Geology, 64, pp. 117-131.
- De, P. K., 1970, *Kaolin-microstructure after consolidation and direct shear*. University of City Ph.D. Thesis.
- Emerson, W. W., 1959, *The structure of soil crumbs*. Journal of Soil Science, 10, pp. 235-244.
- FitzPartick, E. A., 1984, *Micromorphology of soils*. Chapman and Hall Ltd, London.
- Gillott, J. E., 1969, *Study of the fabric of fine-grained sediments with the scanning electron microscope*. Journal of Sedimentary Petrology 39, pp. 90-105.
- Gillott, J. E., 1970, *Fabric of Leda clay investigated by optical, electron-optical, and X-ray diffraction methods*. Engineering Geology, 4, pp. 133-153.
- Greene-Kelly, R., Chapman, S., & Pettifer, K., 1970, *The preparation of thin sections using polyethylene glycols*. Micromorphological Techniques and Applications. D. A. Osmond & P. Bullock ed., pp. 15-24.
- Grim, R. E., 1953, *Clay mineralogy*. McGraw-Hill Book Company, New York.
- Grim, R. E., 1962, *Applied clay mineralogy*. McGraw-Hill Book Company, New York.

- Hayes, J. B., 1970, *Polytypism of chlorite in sedimentary rocks*. Clays and Clay Minerals, 18, pp. 285–306.
- Hearle, J. W. S., Sparrow, J. T., & Cross, P. W., 1972, *The use of the scanning electron microscope*. Pergamon, Oxford.
- Hecht, E. & Zajac, A., 1976, *Optics*. New York, Addison–Wesley Publishing Company.
- Hounslow, M. & Tovey, N. K., 1992, *Porosity measurements in back-scattered SEM images of particulate materials*. Scanning Microscopy, Supplement 6.
- Hsi, H–R. & Clifton, D. F., 1960, *Flocculation of selected clays by various electrolytes*. Proceedings of 9th National Conference on Clays and Clay Minerals, Pergamon Press.
- Ingram, R. L., 1953, *Fissility of mudrocks*. Geological Society of American Bulletin, 64, pp. 869–878.
- Kaarsberg, E. A., 1959, *Introductory studies of natural and artificial argillaceous aggregates by sound–propagation and X–ray diffraction methods*. Journal of Geology, 67, pp. 447–472.
- Keinonen, L. (Trans. U. V. Helava), 1957, *New theory to explain frost action*. NRC Canada Technique Translation.
- Kistler, S. S., 1932, *Coherent expanded aerogels*. Journal of Physics and Chemistry, 36, pp. 52–64.

- Konta, J., 1961, *Imbibometry—a new method for the investigation of clays*. The American Mineralogist, 46, pp. 289–303.
- Lambe, T. W., 1953, *The structure of inorganic soil*. Proceedings of the American Society of Civil Engineers, Separate No. 315, pp. 1–49.
- Lambe, T. W., 1958, *The structure of compacted clay*. ASCE, 84 SM2, pp. 1654–1 to 1654–34.
- Lambe, T. W., 1960, *A mechanistic picture of shear strength in clay*. Research Conference on Shear Strength of Cohesive Soils, ASCE, University of Colorado, Boulder, Colorado, pp. 555–580.
- Lee, I. K., White, W., & Ingles, O. G., 1983, *Geotechnical Engineering*. Pitman Publishing.
- Leng, X., 1992, Personal communication.
- Leonards, G. A., 1962, *Engineering properties of soils*. In "Foundation Engineering", Leonards, G. A., ed., McGraw-Hill Book Company, New York, pp. 66–240.
- Low, P. E., 1959, *Viscosity of water in clay systems*. Proceedings of 8th National Conference on Clays and Clay Minerals, Pergamon Press, pp. 170–182.
- Martin, R. T. & Ladd, C. C., 1975, *Fabric of consolidated kaolinite*. Proceedings of 23rd National Conference on Clays and Clay Minerals, Pergamon Press, pp. 17–25.

- McConnachie, I., 1971, *Electron microscopy of the consolidation of a kaolin*. University of Glasgow Ph. D. Thesis.
- Meade, R. H., 1964, *Removal of water and rearrangement of particles during the compaction of clayey sediments — review*. Geological Survey Professional Paper, No. 497-B, U.S., Dept. of the Interior, pp. B-1 to B-23.
- Miedema, R., Pape, T., & Van der Waal, G. J., 1974, *A method to impregnate wet soil samples, producing high-quality thin sections*. Neth. J. Agric. Sci. 22, pp. 37-39.
- Mitchell, J. K., 1956, *The fabric of natural clays and its relation to engineering properties*. Proceedings of the Highway Research Board, 35, pp. 693-713.
- Morgenstern, N. R. & Tchalenko, J. S., 1967, *The optical determination of preferred orientation in clays and its application to the study of microstructure in consolidated kaolin*. Proceedings of the Royal Society, Series A, 300; Part I, pp. 218-234, Part II, pp. 235-250.
- Murphy, C. P., 1986, *Thin section preparation of soils and sediments*. A B Academic Publishers.
- O'Brien, N. R., 1972, *Microstructure of a laboratory sedimented flocculated illitic sediment*. Canadian Geotechnical Journal, 9, pp. 120-122.
- Olson, R. E., & Mitronovas, F., 1960, *Shear strength and consolidation characteristics of calcium and magnesium illite*. Proceedings of 9th National

---

Conference on Clays and Clay Minerals, Pergamon Press, pp. 185–208.

Olson, R. E., 1962, *The shear strength properties of calcium illite*. Geotechnique, 12, pp. 23–43.

Pusch, R., 1966, *Investigation of clay microstructure by using ultra-thin sections*. Swedish Geotechnical Institute, Reprints and Preliminary Reports, 15.

Pusch, R., 1970, *Microstructural changes in soft quick clay at failure*. Canadian Geotechnical Journal, 7, pp. 1–7.

Rosenqvist, I. Th., 1955, *Investigations in the clay–electrolyte–water system*, Norwegian Geotechnical Institute, Publication Number 9.

Rosenqvist, I. Th., 1959, *Mechanical properties of soil water systems*. ASCE 85 SM2, pp. 31–53.

Rosenqvist, I. Th., 1960, *The influence of physico–chemical factors upon the mechanical properties of clays*. Proceedings of 9th National Conference on Clays and Clay Minerals, Pergamon Press, pp. 12–27.

Rosenqvist, I. Th., 1968, *Mechanical properties of soils from a mineralogical–physical–chemical viewpoint*. An Edited Version of Five Lectures Held at the City University, London, on the University Exchange Scheme.

Schofield, R. K. & Samson, H. R., 1954, *Flocculation of kaolinite due to the attraction of oppositely charged crystal faces*. Discussions of the Faraday Society, 18, pp. 135–145.

- Scott, C. R., 1969, *An introduction to soil mechanics and foundations*. Maclaren and Sons Press, London.
- Seed, H. B. & Chan, C. K., 1961, *Compacted clays: structure and strength characteristics*. Trans. Am. Soc. Civil Eng. 126, pp. 1343–1407.
- Singh, R. B., 1969, *A versatile method for treatment of clay soils for thin section fabric studies*. Journal of Soil Science, 20, pp. 269–273.
- Smart, P., 1966a, *Optical microscopy and soil structure*. Nature 210, 1400.
- Smart, P., 1966b, *Particle arrangements in kaolin*. Proceedings of 9th National Conference on Clays and Clay Minerals, Pergamon Press, pp. 241–254.
- Smart, P., 1966c, *Soil structure, mechanical properties and electronmicroscopy*. University of Cambridge Ph.D. Thesis.
- Smart, P., 1969, *Soil structure in the electron microscope*. Proceedings of the International Conference on Structure, Solid Mechanics Engineering Design, M. Te'eni, ed., London, pp. 249–255.
- Smart, P., 1975, *Soil microstructure*. Soil Science, 119, No. 5, pp. 385–393.
- Smart, P. & Dickson, J. W., 1978, *Deformation and shear of normally consolidated flocculated kaolin*. Pro. Interdisc. Conf. Mechm. Deform. Fract., Lulea 1, pp. 121–128.
- Smart, P. & Tovey, N. K., 1981, *Electron microscopy of soils and sediments*;

*Examples*. Clarendon Press, Oxford.

Smart, P. & Tovey, N. K., 1982, *Electron microscopy of soils and sediments; Techniques*. Clarendon Press, Oxford.

Smart, P. & Tovey, N. K., 1988, *Theoretical aspects of intensity gradient analysis*. *Scanning*, 10, pp. 115–121.

Smart, P. & Tovey, N. K., 1989, *Microfabric of the deformation of soils*. Second Year Report on AFOSR Grant 87–0346.

Smart, P. & Leng, X., 1990, *Image analysis by transputer*. Applications of Transputers 2 – Proceedings of 2nd International Conf. Applications of Transputers, Southampton, 1990. IOS Press, Amsterdam, pp. 240–247.

Smart, P., Tovey, N. K., Leng, X., Hounslow, M. K., & McConnachie, I., 1990, *Automatic analysis of microstructure of cohesive sediments*. pp.359–366 in R. H. Bennett et al eds. *Microstructure of Fine-grained Sediments— From Mud to Shale*. New York, Springer. 1990.

Smart, P. & Leng, X., 1991, *Textural analysis by transputers*. SERC/DTI Transputer Loan Initiative Reports. SERC, Rutherford–Appleton Laboratory, Didcot Vol. 10, pp. 1–15.

Smart, P. 1992, Personal Communication.

Smart, P & Leng, X., 1992, *Textural analysis*. In H. C. Webber ed. *Image Processing and Transputers*. IOS Press, Amsterdam, pp. 73–95.

- Smart, P., Leng, X. & Bai, X., 1992, *Image analysis of soil microstructure*. Geotechnique et Informatique, Presses de l'école nationale des Ponts et Chaussées, pp. 905–912
- Soil Mechanics and Foundations for Undergraduates*, 1985, South University of Technology et al eds. (in Chinese).
- Tan, T. K., 1959, *Structure mechanics of clays*. Scientia Sinica, 8, pp. 83–97.
- Taylor, A. W., 1959, *Physico-chemical properties of soils: ion exchange phenomena*. ASCE 85 SM2, pp. 19–30.
- Tchaleko, J. S., 1967, *Influence of shear and consolidation on the microscopic structure of some clays*. University of London Ph.D. Thesis.
- Terzaghi, K., 1925, *Principles of soil mechanics*. Engineering News Record, 95.
- Tovey, N. K., 1970, *Electron microscopy of clays*. University of Cambridge Ph.D. Thesis.
- Tovey, N. K., 1971, *Soil structure analysis using optical techniques on scanning electron micrographs*. Proceedings of 4th SEM Symp. IIT Research Institute, Chicago, pp. 49–56.
- Tovey, N. K., 1980, *Digital computer technique for an orientation analysis of micrographs of soil fabric*. Journal of Microscopy, 120, pp. 303–315.
- Tovey, N. K. & Sokolov, V. N., 1981, *Quantitative SEM methods for soil*

*fabric analysis*. Scanning Electron Microscopy, 1, pp. 536–554.

Tovey, N. K. & Smart, P., 1986, *Intensity gradient techniques for orientation analysis of electron micrographs*. Scanning, 8, pp. 75–90.

Unitt, B. M., 1975, *A digital computer method for revealing directional information in images*. Journal of Physics, E Series 2, 8, pp. 423–425.

Unitt, B.M. & Smith, K. C. A., 1976, *The application of the minicomputer in scanning electron microscopy*. Proceedings of 6th Eur. Reg. Cong. Electron Microsc. 1, pp. 162–167.

Van Olphen, H., 1963, *An introduction to clay colloid chemistry*. Interscience Publishers, London.

Vermeer, P. A., 1990, *The orientation of shear bands in biaxial tests*. Geotechnique, 40, pp. 223–236.

Ward, W. H., Marsland, A., & Samuels, S. G., 1965, *Properties of London clay at the Ashford Common shaft: in-situ and undrained strength tests*. Geotechnique, 15, pp. 321–344.

Williams, P. J., 1964, *Experimental determination of apparent specific heats of frozen soils*. Geotechnique, 14, pp. 133–142.

Wong, K. Y., 1975, *Microfabric changes during the deformation of clays*. University of Cambridge Ph.D. Thesis.

---

Wu, T. H., 1958, *Geotechnical properties of glacial lake clays*. ASCE 84 SM3, pp.1732-1 to 1732-34.